to ~55% of the shell model values of $(2J+1)$. This is significantly lower than spectroscopic factors resulting from other reactions. Generally, the kinematic regions of better agreement between the analysing power data and calculations are similar to those of the earlier $^{16}O(\vec{p},2p)$ experiment. The analysing power for the $2s_{1/2}$ state near $\ell=0$ dominance is reasonably predicted whether spin-orbit dependence in the optical model is included or not.

At various kinematic conditions, peaks in the cross section suggest the possible presence of $1p_{1/2}$ and $1p_{3/2}$ ^{40}Ca single particle states at ~21 MeV and ~30 MeV separation energy respectively.

0-315-03534-X

PERMISSION TO MICROFILM — AUTORISATION DE MICROFILMER

• Please print or type — Écrire en lettres moulées ou dactylographier

Full Name of Author — Nom complet de l'auteur

LARRY EDWARD ANTONUK

Date of Birth — Date de naissance	Country of Birth — Lieu de naissance
5 Sept. 1953	CANADA

Permanent Address — Résidence fixe

Nuclear Research Center, University of Alberta

Title of Thesis — Titre de la thèse

Quasi - Elastic Scattering of Polarized Protons From Calcium - 40 at 200 MeV

University — Université

University of Alberta

Degree for which thesis was presented — Grade pour lequel cette thèse fut présentée

Phd. Nuclear Physics

Year this degree conferred — Année d'obtention de ce grade	Name of Supervisor — Nom du directeur de thèse
1981	Dr. P. Kitching

Date	Signature
December 19/81	Larry E. Antonuk

NL-91 (4/77)

NOTICE

AVIS

The quality of this microfiche is heavily dependent upon the quality of the original thesis submitted for microfilming. Every effort has been made to ensure the highest quality of reproduction possible.

If pages are missing, contact the university which granted the degree.

Some pages may have indistinct print especially if the original pages were typed with a poor typewriter ribbon or if the university sent us a poor photocopy.

Previously copyrighted materials (journal articles, published tests, etc.) are not filmed.

Reproduction in full or in part of this film is governed by the Canadian Copyright Act, R.S.C. 1970, c. C-30. Please read the authorization forms which accompany this thesis.

La qualité de cette microfiche dépend grandement de la qualité de la thèse soumise au microfilmage. Nous avons tout fait pour assurer une qualité supérieure de reproduction.

S'il manque des pages, veuillez communiquer avec l'université qui a conféré le grade.

La qualité d'impression de certaines pages peut laisser à désirer, surtout si les pages originales ont été dactylographiées à l'aide d'un ruban usé ou si l'université nous a fait parvenir une photocopie de mauvaise qualité.

Les documents qui font déjà l'objet d'un droit d'auteur (articles de revue, examens publiés, etc.) ne sont pas microfilmés.

La reproduction, même partielle, de ce microfilm est soumise à la Loi canadienne sur le droit d'auteur, SRC 1970, c. C-30. Veuillez prendre connaissance des formules d'autorisation qui accompagnent cette thèse.

THIS DISSERTATION
HAS BEEN MICROFILMED
EXACTLY AS RECEIVED

LA THÈSE A ÉTÉ
MICROFILMÉE TELLE QUE
NOUS L'AVONS REÇUE

THE UNIVERSITY OF ALBERTA

QUASI-ELASTIC SCATTERING

OF POLARIZED PROTONS

FROM CALCIUM-40 AT 200 MEV

by

Ⓒ LARRY EDWARD ANTONUK

A THESIS

SUBMITTED TO THE FACULTY OF GRADUATE STUDIES AND RESEARCH

IN PARTIAL FULFILMENT OF THE REQUIREMENTS FOR THE DEGREE

OF DOCTOR OF PHILOSOPHY

in

NUCLEAR PHYSICS

DEPARTMENT OF PHYSICS

EDMONTON, ALBERTA

SPRING, 1981

THE UNIVERSITY OF ALBERTA

RELEASE FORM

NAME OF AUTHOR   LARRY EDWARD ANTONUK

TITLE OF THESIS   QUASI-ELASTIC SCATTERING

OF POLARIZED PROTONS

FROM CALCIUM-40 AT 200 MEV

DEGREE FOR WHICH THESIS WAS PRESENTED   DOCTOR OF PHILOSOPHY

YEAR THIS DEGREE GRANTED   1981

Permission is hereby granted to THE UNIVERSITY OF ALBERTA LIBRARY to reproduce single copies of this thesis and to lend or sell such copies for private, scholarly or scientific research purposes only.

The author reserves other publication rights, and neither the thesis nor extensive extracts from it may be printed or otherwise reproduced without the author's written permission.

(Signed) *Larry E. Antonuk*

PERMANENT ADDRESS:

NUCLEAR RESEARCH CENTER

UNIVERSITY OF ALBERTA

EDMONTON, ALBERTA

T6G-2N5

DATED *December 11, 1980*

THE UNIVERSITY OF ALBERTA

FACULTY OF GRADUATE STUDIES AND RESEARCH

The undersigned certify that they have read, and
recommend to the Faculty of Graduate Studies and Research,
for acceptance, a thesis entitled "QUASI-ELASTIC
SCATTERING OF POLARIZED PROTONS FROM CALCIUM-40 AT 200 MEV"
submitted by LARRY EDWARD ANTONUK
in partial fulfilment of the requirements for the degree of
Doctor of Philosophy in Nuclear Physics.

....
Supervisor

....

....

....

....

....
External Examiner

Date.....4ᵀᴴ Dec 1980.....

TO MY MOTHER

WHOSE LOVE, SUPPORT, PATIENCE, AND FAITH HAS SUSTAINED AND

INSPIRED ME THROUGH ALL.

\ABSTRACT

A $^{40}Ca(\vec{p},2p)$ experiment was performed at the TRIUMF facility using a 200 MeV polarized proton beam. Data were acquired at eleven independent pairs of angles for separation energies from 0 to 100 MeV over a wide range of recoil momenta. For eight angle pairs, cross sections and analysing powers were extracted from the data as a function of the energy difference of the final state protons for knockout from the valence states ($1d_{3/2}$, $2s_{1/2}$, and $1d_{5/2}$). Cross section and analysing power information was obtained for 3 other angle pairs for only the $2s_{1/2}$ state.

The results were compared with Distorted Wave Impulse Approximation (DWIA) calculations which incorporated the bound state wave functions of Elton and Swift (EL-67), an optical model potential, with spin-orbit terms, from Schwandt (SC-80), and a half-off-shell prescription for the free p-p scattering matrix element. The $\ell=2$ states show strong j-dependence in the analysing power at most measured angles. Such dependence was predicted by Jacob and Maris (JA-73) and has been observed for $\ell=1$ states in ^{16}O (KI-80,KI-76). DWIA calculations agree well with the present analysing powers for equal and near equal angles in the forward direction. The spectroscopic factors resulting from normalizing the calculations to the data are only ~50%

ACKNOWLEDGEMENTS

assistance in maintaining the experimental apparatus during the experiment and the Eclipse during later analysis and for their explanations of many technical questions which arose.

Special thanks goes to several University of Alberta post-doctoral fellows - to Al Anderson for his patient explanations of the workings of the Eclipse and for introducing me to mountain-climbing at a time when the long thesis work got me down - to R. L. Liljestrand and H. Wilson for their advice on the project and their companionship on several excellent hiking and skiing trips.

I am indebted to my fellow graduate students, Rick Hooper, Ron Sloboda, Tim Cooper, Doug Hasell, and Doug Phillips for their solace and warm fellowship.

A special thanks to Phil Bennett, Arthur Haynes, and Corrie Kost for their special modifications of OPDATA which made the long task of fitting less mind numbing.

My thanks goes to C.W. Bordeaux for allowing me the use of TRIUMF's word processor without which the writing of this thesis would have been an unimaginably dreary task. I also thank Anna Gelbart and Hugh Rogan who did such a fine job drafting and assembling my figures.

Thanks also must go to all the individuals who proof-read my thesis including Dr. R. Abegg and Allyson MacBean.

Finally I thank my two very special and dear friends, Keith Corson and Ann Beales whose companionship on many

hiking, skiing, bicycling, and canoeing trips was greatly appreciated during the last five years.

The financial support of the National Research Council of Canada, the University of Alberta, and TRIUMF are gratefully acknowledged.

ix

TABLE OF CONTENTS

xi

LIST OF TABLES

LIST OF FIGURES

CHAPTER I

INTRODUCTION

Quasi-elastic (p,2p) scattering occurs when the incident proton undergoes a single violent interaction with the nuclear proton; this collision is usually treated as free proton-proton scattering. Thus, although there has been some theoretical investigation of two step processes (KU-79), quasi-elastic scattering is usually viewed as a single step process as represented schematically in Figure I-1. Currently, one of the most immediate aspects of (p,2p) reactions is that they allow a check of the validity of the wave functions describing the propagation of protons through the nucleus. Also, in addition to offering an opportunity to examine the proton-proton interaction in the environment of a nuclear potential, a study of the resulting hole states in the residual nucleus tests nuclear models by providing information on the overlap between the wave functions of the target ground state and excited states of the residual nucleus.

A classical view of the (p,2p) reaction is as follows. As illustrated in Figure I-2, an incoming proton (mass M) which is incident upon a target nucleus (mass M_A) strikes a bound particle and the two protons scatter to detectors without undergoing any other violent interactions. In the shell model, each bound state nucleon is characterized by a well-defined orbital angular momentum and binding energy.

FIGURE I-1

Schematic representation of a (p,2p)
reaction as a single step process.

FIGURE I-2

Diagramatic representation of a (p,2p)
reaction illustrating the labelling of the
various kinematic quantities.

p_0

p_1

p_2

A

A-1

$(\vec{k_0}, E_0)$

M

M_A

$(\vec{k_2}, E_2)$

M

θ_2

M_{A-1}

θ_1

M

$(\vec{k_{A-1}}, E_{A-1})$

$(\vec{k_1}, E_1)$
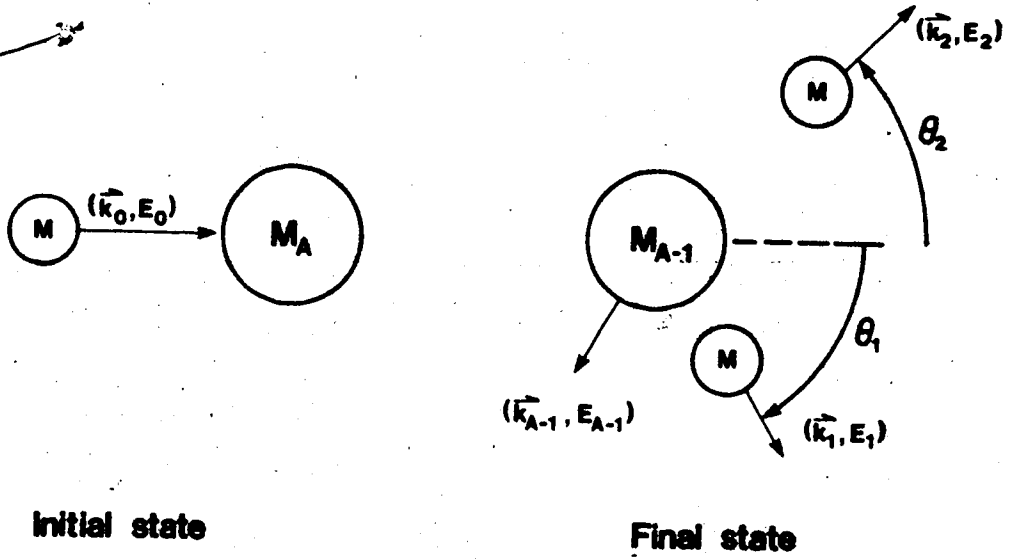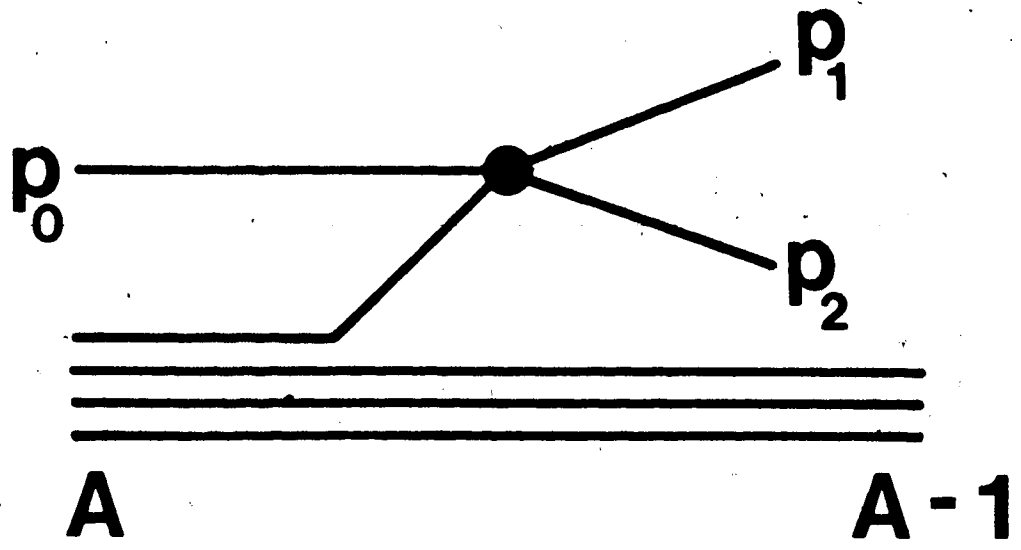
Initial state

Final state

Thus the interaction results in the knocking out of a moving nuclear proton which "almost" behaves like a free nucleon. Such "quasi-free" collisions result in a strong angular correlation between the outgoing protons as well as peaks in the summed energy spectrum corresponding to the binding energies of the various single particle states.

A characteristic of quasi-free scattering is that the target nucleon can have an effective initial polarization in the reaction. In asymmetric kinematic conditions, the reaction may be localized. For example, below 400 MeV, the mean free path of protons travelling through nuclear matter decreases strongly as the energy decreases. Consequently, events in which one proton emerges with a large energy compared to the other may tend to originate on the side of the nucleus in the direction of the momentum of the lower energy proton. This results in a spatial localization of the reaction. (This is distinct from the localization of the (p,2p) reaction due to radial peaking of the bound state wave function. Surface localization does not occur for the $1s_{1/2}$ state wave function which is mainly concentrated near r=0.) A careful selection of the angles and energies of the outgoing protons determines the magnitude and direction of the momentum of the struck particle which can couple to a localized enhancement of the reaction and this leads to a well-defined sense of orbital angular momentum. Through nuclear spin-orbit coupling, the struck proton is effectively polarized in a direction

normal to the scattering plane. In particular, protons in states of the same ℓ but different j will be polarized in opposite directions. This, coupled with the fact that the free p-p cross section for the scattering of protons with parallel spins is larger than that for antiparallel spins, leads to a j-dependence in the $(\vec{p},2p)$ analysing power. This dependence was predicted by Jacob and Maris (JA-73) and first observed for the $\ell=1$ states of ^{16}O (KI-80,KI-76). Therefore, $(\vec{p},2p)$ could conceivably be used as a spectroscopic tool to distinguish states of the same ℓ but different j.

A quantitative picture of $(\vec{p},2p)$ includes the effect of nuclear distortion of the proton wave functions and is formulated using the Distorted Wave Impulse Approximation (DWIA). In Appendix I, the DWIA description is, discussed and details are given about the manner in which the j-dependence in the analysing power arises. In the present context, the struck particle polarization and hence the analysing power are more promising than the cross section in testing DWIA. This arises because of the particular insensitivity of analysing power to the bound state wavefunction and the spectroscopic factor. Also, the analysing power is less sensitive to the optical potential than the cross section.

From the earliest experiments to the present, analysis of (p,2p) experiments has consisted of organizing the data either on the basis of the summed energy of the outgoing

protons, on the recoil momentum of the residual nucleus, on the outgoing angles, or on some combination of these (KU-71,JA-69,TY-66,WI-55,CH-52). Early interest in (p,2p) reactions focussed on attempts to study the momentum distribution of bound nucleons by measuring energy distributions for one outgoing proton over a variety of scattering angles (CL-52). In the first (p,2p) coincidence experiment (CH-52), angular correlations for ^{6}Li were measured about an opening angle 90°. The degree to which bound nucleons exhibited free nucleon (quasi-free) behavior was examined in these studies. Later coincidence experiments which measured the energy of one (WI-55) or both (TY-58) outgoing protons gave some of the first direct evidence of the existence of single particle shell model states.

Several features of quasi-free scattering contribute to the interest in this reaction. The kinematics of the (p,2p) reaction allow the recoil momentum to vary over a wide and useful range from zero to several hundred MeV/c. Consequently, it should be possible to distinguish between states of differing ℓ, particularly $\ell \neq 0$ states (whose momentum distribution, and hence cross section, is at a minimum at zero recoil momentum - as explained in Appendix I) from $\ell = 0$ states (whose momentum distribution is at a maximum there). In addition, the same binding energy and recoil momentum region can be examined with a number of different kinematic configurations. This redundancy allows

one to examine the interaction process for a given nuclear state under a variety of conditions. Comparisons with a DWIA formalism can then be made.

During the quasi-elastic reaction, the binding energy of the struck nucleon together with the recoil momentum of the residual nucleus makes the 2 body t-matrix half-off-shell (RE-70). In addition, the distortion suffered by the incoming and outgoing protons causes the t-matrix to be fully off-shell (RE-73). However, if this latter effect can be ignored and the DWIA is a sufficiently accurate description of the (p,2p) reaction, it may be possible to extract off-shell t_{pp} matrix information which can then be compared with the predictions of various phase-equivalent (phenomenological) potentials (BI-76). Such potentials are equivalent on the energy shell and the hope is that one can distinguish among them by calculations of off-shell processes. Unfortunately, to extract nucleon-nucleon information one must perform accurate calculations of the effects of distortion, which can be quite large.

It has been suggested that certain experimental geometries might be particularly propitious for the examination of off-shell effects (IO-78,DE-79). With such geometries an attempt would be made to utilize the variety of kinematic conditions possible for the reaction. The expectation was that the sensitivity of calculations to distortion and the bound state wave functions could be reduced by holding the outgoing proton energies constant

while the initial state of the nucleus being examined was fixed by restricting the value of the recoil momentum. However, calculations comparing off-shell behavior in (p,2p) geometries expected to maximize such differences have shown disappointingly small sensitivity to the potential used (MI-79).

From the above discussion, the (p,2p) reaction is seen to offer information on nuclear structure, off-shell effects, and propagation of protons through nuclear matter. There are, of course, a number of other reactions which give information complementary to that obtained in (p,2p). Through knockout or pickup reactions such as (p,pn), (e,e'p), (α,αp), (p,d), (d,^{3}He), and (γ,p), information on nuclear structure through the removal of a single nucleon is acquired. The knockout reactions (p,pn) and (e,e'p) are fairly well described by a single step DWIA formalism at intermediate energies. Like the (p,2p) reaction, these offer considerable kinematic freedom including wide variation of the recoil momentum. Experimental investigations of (p,pn) reactions can be designed to acquire (p,2p) information simultaneously (JA-79). Such measurements are expected to yield information about bound neutrons similar to that from (p,2p) reactions concerning bound protons.

The impulse approximation can be checked by finding quasifree processes which have nearly equal distortion and differ primarily in the knock-out process itself. An

example of such a test was an analysis of $^{12}C(p,2p)$ and $^{12}C(p,pn)$ data (MA-79). By taking the ratio of the cross sections for each process, the effects of distortion nearly cancel. A comparison of the ratio of the measured cross sections with the theoretical predictions serves as a check of the impulse approximation.

Information about the momentum distribution for the deeply bound states of several nuclei including ^{40}Ca has been acquired through (e,e'p) measurements (MO-76,NA-76,AM-66). Compared to (p,pN), (e,e'p) with only one strongly interacting particle might be expected to suffer less nuclear distortion and the interaction is presumably well understood. However, cross sections tend to be several orders of magnitude lower and thus harder to extract from background. Enticing evidence for 1s and 1p single particle state strengths in ^{40}Ca has been published (MO-76) although better statistics would be desirable. The (γ,p) reaction can also excite hole states and offers advantages and disadvantages similar to those for (e,e'p), but the range of experimentally accessible recoil momenta is restricted to values >300 MeV/c (MA-75). Apart from the fact that data is limited due to the difficulty of the experiments, questions about the reaction mechanism make an interpretation of the results difficult. A recent $^{16}O(\gamma,p)$ experiment suggests that one-step processes are inadequate to account for the observed differential cross sections and that the inclusion of two-step processes improves agreement

with the data (MA-77).

(α,αp) quasi-elastic scattering is strongly surface localized compared to (p,2p) due to the strong absorption of α particles in nuclear matter. Some recent (α,αp) measurements on ^{6}Li and ^{19}F are in fair agreement with DWIA calculations and, in the case of ^{6}Li, yield a spectroscopic factor consistent with that derived from a DWIA analysis of ^{6}Li(p,2p) data (NA-79). Measurements of (α,αp) and (p,2p) on ^{40}Ca are currently being analysed (RO-80).

The neutron pickup reaction, (p,d), provides information about high momentum (>300 MeV/c) components of bound neutron wave functions. Recent ^{40}Ca(p,d) measurements show evidence for a number of single particle states up to excitation energies of 18 MeV (LI-80,AL-79,SM-79). In addition, this reaction is potentially useful in probing deep hole states. With the advent of polarized beams, ($\vec{p}$,d) analysing power measurements have been shown to distinguish strongly between states of the same ℓ but different j (HU-80,AL-79,CH-67). High momentum components are also examined in the (d,^{3}He) reaction. States of different ℓ are readily distinguished by the angular distributions of their cross sections (KR-71). High resolution ^{40}Ca(d,^{3}He) measurements at 52 MeV have provided detailed spectroscopic information from the ground state to excitation energies of ~10 MeV (DO-76).

The current investigation of ^{40}Ca($\vec{p}$,2p) is an extension of the previous ^{16}O($\vec{p}$,2p) experiment (KI-80,

KI-76) and offers new possibilities. The choice of ^{16}O and ^{40}Ca targets follows from their reputations as good shell model nuclei which should provide relatively pure single particle states.

The separation between any two of the three valence states of ^{40}Ca ($1d_{3/2}$, $2s_{1/2}$, $1d_{5/2}$) is less than 3 MeV making them experimentally more difficult to resolve than, for example, the states of ^{16}O which are 6.5 MeV apart. With improving energy resolution, more recent $^{40}Ca(p,2p)$ experiments (TY-66,JA-69,KU-71) have tended to emphasize the nuclear spectroscopy aspect. A recent $^{40}Ca(p,2p)$ experiment (RO-78) attained a resolution of 350 keV but examined only the $1d_{3/2}$ and $2s_{1/2}$ states. The best resolution attained in a (p,2p) measurement which examined all three ^{40}Ca valence states was 4 to 5 MeV (JA-69). Thus, a goal of this experiment was to attain the best possible beam and detector resolution in order to fully or partially resolve all the valence states. A knowledge of excitation energies and relative spectroscopic factors for the removal of protons from a particular single particle state can greatly assist in the analysis and interpretation of nucleon knockout experiments where the resolution may be inadequate to resolve individual peaks. Such factors for ^{40}Ca have been provided by DWBA analyses of (p,d), (d,^{3}He), and (d,^{3}H) experiments (DO-76,MA-72) and were helpful in this investigation.

In the present experiment, both the cross sections and

analysing powers for the three valence states of ^{40}Ca were measured over a large range of recoil momenta. With the kinematics chosen so as to achieve a large effective polarization of the struck proton, the j-dependence of the analysing power of $\ell=2$ states was examined for the first time. The degree to which DWIA could reproduce the data and, in particular, the extent to which the inclusion of spin-orbit distortion affected agreement of the predictions with the data were of major interest. This experiment was the first experimental investigation of ($\vec{p}$,2p) on a medium mass nucleus and was also the first investigation of the ability of DWIA to reproduce such data.

In previous ^{40}Ca(p,2p) experiments, James (JA-69) and Kullander (KU-71) both reported evidence for 1p and 1s strength in ^{40}Ca. The current experiment also offers the prospect of examining deeply bound nuclear states and provides the possibility for distinguishing between states such as $1p_{1/2}$ and $1p_{3/2}$ on the basis of the behavior of their analysing powers. The measurement of binding energies and widths of deeply bound states provides important data for comparison with nuclear matter calculations from 2-body interactions (CO-74,SP-72,SP-71).

CHAPTER II

EXPERIMENTAL DETAILS

2.1 Overview

The experiment was performed at the TRIUMF facility located near the University of British Columbia. The TRIUMF cyclotron delivered a 200 MeV polarized proton beam with a polarization of ~0.6 → ~0.75 and with an energy resolution better than 1%. The cyclotron accelerates H^- ions and a proton beam is extracted by removing both electrons from the ions by means of a stripper foil. The proton beam has $\lesssim 7$ ns pulses separated in time by ~43 ns. During the experiment the average beam current was kept at 0.5 to 1.0 nA.

The experimental configuration is illustrated schematically in Figure II-1. Four detector telescopes were mounted on booms which could be positioned independently around a circular scattering chamber with an angular precision of ±0.10°. Beam polarization was measured by means of a polarimeter located upstream of the scattering chamber. Beam current was monitored both by means of the polarimeter and an ion chamber located downstream of the scattering chamber. A more detailed description of various components of the apparatus follows.

2.2 Polarimeter

The polarimeter used in this experiment has been

13

FIGURE II-1
Experimental configuration of polarimeter,
scattering chamber, and detectors.

LB

NaI(Tℓ)

COPPER

PLASTIC
SCINTILLATOR

MWPC

LF

SCATTERING
CHAMBER

POLARIMETER

L2 L1

R3

CH₂

SOFT VACUUM

L3

R2 R1

BEAM

THIN
KAPTON
WINDOW

TARGET

RF

RB
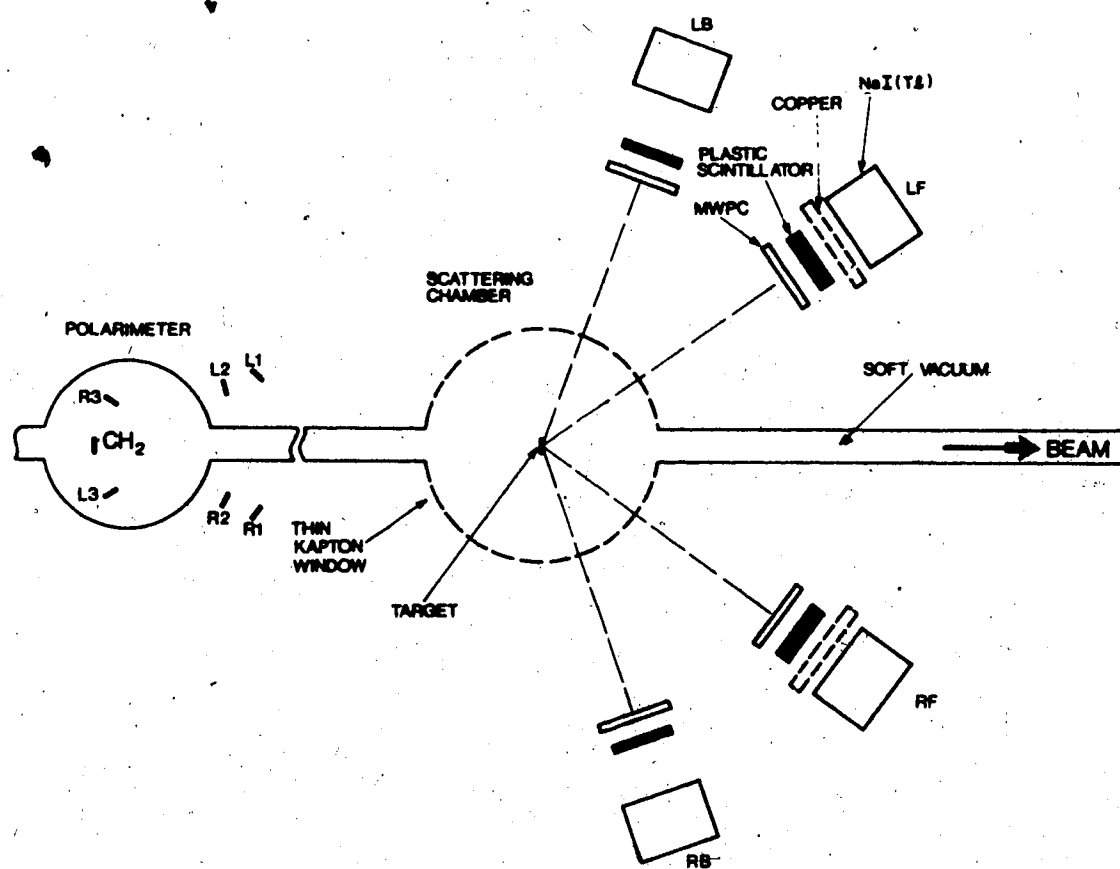
described in detail in (GR-79,MC-78). Free p-p scattering using a CH_2 target with an average thickness of $3.83\pm.38$ mg/cm^2 was used for monitoring both the beam polarization and beam current. The polarimeter detectors are illustrated in Figure II-1. On either side of the beamline a pair of detectors at 17° (L1·L2 or R1·R2) acted as a telescope to define the solid angle. Triple coincidences (L1·L2·L3 and R1·R2·R3) are called prompts (consisting of reals and randoms) and are counted. To measure the contribution of random events, coincidences between these same sets of detectors but with L3 and R3 delayed by 43 nanoseconds were also counted. This delay ensures that the protons come from different beam bursts and hence different interactions. The rate of accidental events from one beam burst is assumed to be the same as that between two consecutive beam bursts. A schematic diagram of the polarimeter electronics is shown in Figure II-2.

We denote the number of prompt coincidences L1·L2·L3 (R1·R2·R3) as POL[L] (POL[R]) and the number of accidental coincidences as POL[LACC] (POL[RACC]). The beam polarization and number of incident protons (NI_a) are given by

$$(II.1) \quad \text{Beam Polarization} = \frac{1}{PAP} \cdot \frac{\left(POL[LRE] - POL[RRE]\right)}{\left(POL[LRE] + POL[RRE]\right)}$$

$$(II.2) \quad NI_a = \left(POL[LRE] + POL[RRE]\right) \cdot \frac{6.2418 \times 10^9}{PC},$$

FIGURE II-2
        Logic diagram of polarimeter electronics.
        Logic symbols are defined in Figure III-1.
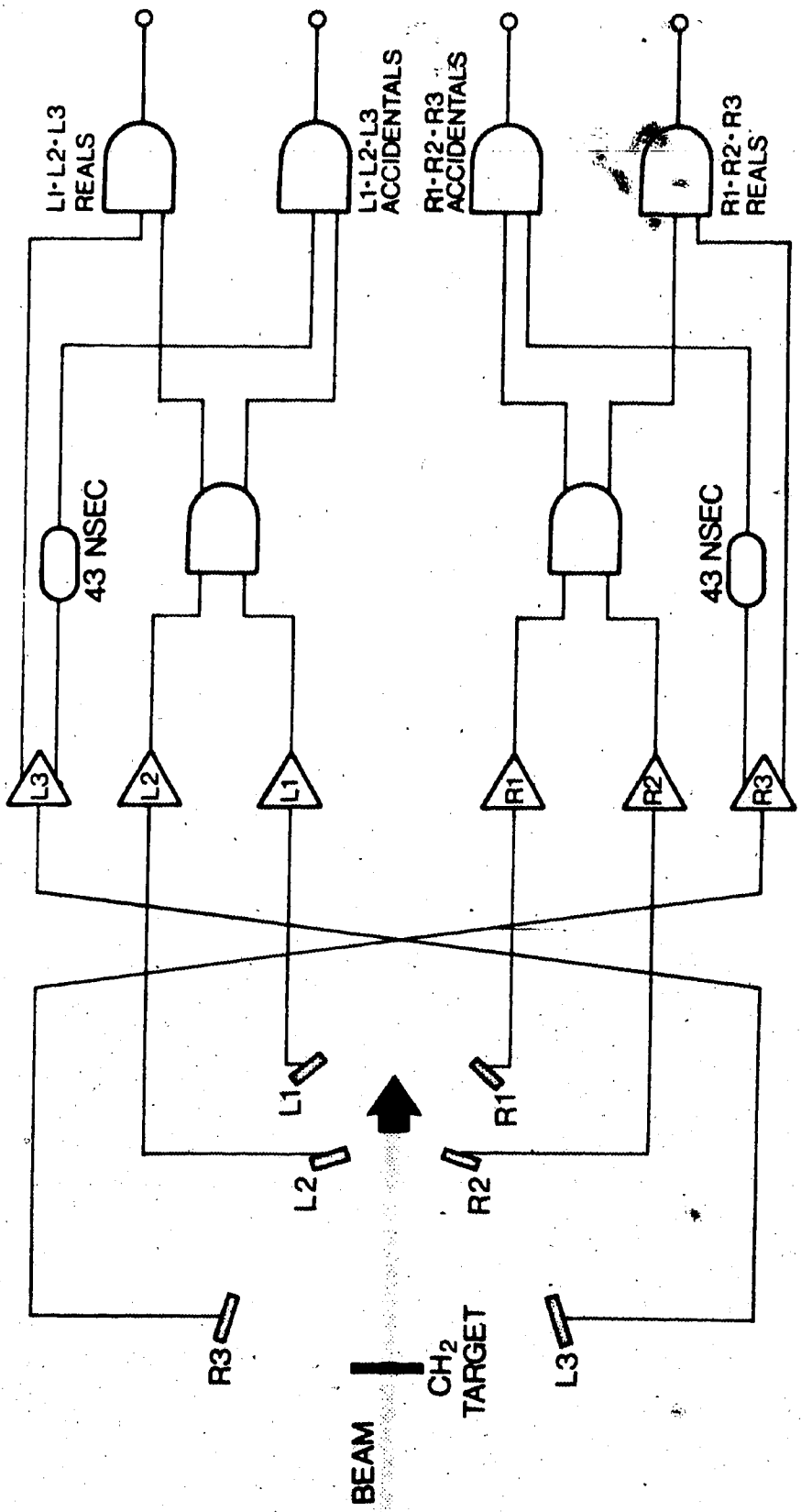
where   POL[LRE] = POL[L] - POL[LACC],

POL[RRE] = POL[R] - POL[RACC],

PAP is the polarimeter analysing power which equals 0.300±0.015 at 200 MeV,

PC is the conversion factor from polarimeter counts to nanocoulombs which equals 350±25 counts per nanocoulomb at 200 MeV.

Beam polarization for spin ↑ (↓) typically ranged from 0.67 to 0.75 (-0.61 to -0.70) during the experiment. The polarimeter served as the primary beam monitor in the experiment.

2.3 Ion Chamber

A detailed description of the ion chamber, its operation, and calibration appears in (MC-78). In brief, the proton beam passing through the ion chamber ionizes helium gas that is continually flowing through the chamber. The resulting charge is collected by means of high voltage planes in the chamber and a digital signal proportional to the amount of charge is produced. During the experiment the voltage was maintained at -300 Volts. If the number of ion chamber counts is represented by IC, the number of incident protons (NI_b) is given by

$$(II.3) \quad NI_b = \frac{IC \cdot 6.2418 \times 10^9}{ICC} \quad ,$$

where   the conversion factor from ion chamber counts to nanocoulombs (ICC) is 156±11 at 200 MeV.

The ion chamber served as a secondary beam monitor, and its

consistency with the polarimeter is discussed in Chapter IV.

2.4 Targets and the Scattering Chamber

A circular scattering chamber with a radius of 25 cm was used. The window of the chamber is 5 cm high, allows the passage of scattered particles from 12° to 168° on either side of the beamline, and consists of 127 μm thick Kapton. The targets used in the experiment were: CD_2 (58 mg/cm^2±5%), CH_2 (50 mg/cm^2±5%), a natural Ca target (50.88 mg/cm^2±5%, of which 96.97% is ^{40}Ca and we shall refer to it as the ^{40}Ca target), and a ZnS scintillator screen for monitoring the position of the beam. They were mounted, one above the other, on a vertical ladder which can be raised or lowered remotely so as to position the desired target in the path of the proton beam. The target drive mechanism is mounted on a plate which sits on the top of the scattering chamber. The CD_2 target is circular with a diameter of 3 cm, while the other targets are ~5 cm square.

2.5 Detector Telescopes

The four booms surrounding the target chamber were designated: Left Front (LF), Right Front (RF), Left Back (LB), and Right Back (RB), where left or right refer to the side of the beamline looking downstream. This labelling is illustrated in Figure II-1. Also shown in the Figure is the arrangement of the components of the detector telescopes on each boom. Each telescope consisted of two

multi-wire proportional counter (MWPC) planes to provide position information in the horizontal (x) and vertical (y) directions, a thin plastic counter, and a NaI(Tℓ) detector. The front (back) wire planes were 134.1 (115.2) cm from the target and were 64(x) by 128(y) (64 by 64) wires. The solid angles were defined using these planes. The construction and operation of these multiwire detectors is reviewed in (MC-78,CA-75).

Each multiwire chamber consists of a plane of high voltage wires kept at -5000 Volts, a sense plane of wires, a second high voltage plane, a second sense plane, and a final high voltage plane. The sense wires are 16 μm in diameter, spaced 2 mm apart, and made of gold-plated tungsten. The high voltage wires are 102 μm in diameter, spaced 1 mm apart, and consist of beryllium (1.9%) and copper. The wire planes are enclosed between sheets of 25.4 μm thick Kapton, and the 4.7 cm spacing between the Kapton sheets is continuously flushed with a gas mixture (75% Ar bubbled through methylal at 0°C, 24.5% isobutane, and 0.5% freon).

A plastic scintillator 12.8 cm square and 0.635 (0.3275) cm thick was positioned behind each front (back) MWPC. Each of these detectors consists of NE110 scintillator and is connected to a plastic light guide which directs the light flashes through a 90° bend to a 5 cm RCA 8575 photomultiplier. The scintillators acted as passing counters providing timing and energy loss (dE/dx)

information. The energy deposited in these detectors was used in the calculation of a mass parameter to separate deuterons from protons.

NaI detectors served as stopping counters to measure the kinetic energies (T) of the protons. A detailed description of these detectors and their efficiency appears in (CA-77). The large quantity of light generated by detected particles in intermediate energy experiments commonly results in a gain shift in the photomultiplier tube with detected flux. This problem arises because the current flow in the photo-cathode induces a voltage drop across it, which distorts the electric field collecting the photo-electrons. The electronics of the base of the 12.5 cm photomultiplier tube were specifically designed to minimize this problem and are sketched in Figure II-3. The 4 tube bases were fed through a common 10 μF capacitor kept at +1600 V. Normally, the outputs from the photomultiplier are passed through a pulse shaper before integrating with an analogue to digital converter (ADC). The nearly exponential tails of such shaped signals are quite long (10 μs) and the possibility arises that the tail of a previous pulse may overlap a pulse of interest. Also a second pulse may arrive during the integration of the first pulse. In either case the undesirable result is that the total integrated signal contains contributions from more than one pulse (a condition referred to as pile-up). To overcome this concern, devices called pile-up monitors which note

FIGURE II-3
        Diagram of NaI photomultiplier tube base.

ANODE → 64 ns DELAY LINE

TO ELECTRONICS

V+ (1600V 6.67mA)

MVS 460

the arrival of two signals within a specified gate (length of time) were used. Pile-up monitors with inputs from the plastic scintillators recorded instances when two signals from a plastic detector were sufficiently close in time that the corresponding NaI signals would overlap. Signals from the plastics were used as they are sharp (~10 ns) and thus allow the pile-up monitor to resolve between signals close in time. Beam current was kept low enough that pile-ups did not exceed 20% of the signals processed. Pile-ups were rejected in later analysis of the data.

In principle, the long exponential tails from the NaI tube base can be brought back to zero voltage (the baseline voltage) quickly by adding an attenuated, inverted, and delayed component of the original signal to the original signal. Such a cancellation was attempted by means of a clip line connected to the tube anode in parallel with the signal cable. As shown in Figure II-3, the clip line was terminated with a 0.5 μF capacitor and a resistance (15 Ohms) which is lower than the characteristic impedance of the cable (50 Ohms). The resulting output signal was directed to an ADC with no pulse shaping and could be integrated in approximately one-tenth the time. Although it was expected that such clipping would decrease energy resolution while allowing significantly higher event rates, tuning of the electronics at the start of the experiment indicated that the resolution remained constant whether the terminators were connected or not. Subsequently it was

decided to proceed without the terminators and to live with longer integration times and necessarily lower event rates.

Each NaI(Tℓ) crystal and tube base was encased in an antimagnetic shield (Mu metal) which sat in an iron pipe. This pipe was, in turn, mounted in a lead pig to shield the NaI detector from background radiation. The NaI detectors were positioned 2.5 cm behind the plastic scintillators. The NaI(Tℓ) crystals are cylindrical with a 12.7 cm diameter and a 7.62 cm thickness capable of stopping 150 MeV protons. When the front detectors (LF, RF) were operated forward of 29°, a 0.631 cm thick copper plate was inserted behind each of the front plastic scintillators to degrade the proton energies sufficiently to stop them in the NaI detectors. Taped to the detection surface of each NaI and plastic was a light-emitting diode (LED) driven by a pulse generator. The pulser also fired one wire in each of the MWPC planes. The response of the NaI detectors to the pulser signal had an ~50 ns rise time and a fall time of ~300 ns.

CHAPTER III

EXPERIMENTAL PROCEDURE

To process the information from the detectors a combination of fast NIM and CAMAC electronics was employed. The electronics were divided into two sections: one near the scattering chamber and detectors, the other in a remote counting room. A Honeywell H316 computer located in the counting room received event information processed by the electronics via a CAMAC network. A data acquisition program, ORION, controlled the data processing in the Honeywell. A detailed description of the structure and operation of this data acquisition system has been given in a series of internal reports (RO-74,RO-75,RO-75a,RO-77).

A schematic diagram illustrating the electronics located near the scattering chamber is shown in Figure III-1 while those located in the counting room are shown in Figures III-2 and III-3. A coincidence between a left and a right plastic detector generated an EVENT FAST signal. This requested the multiwire controller to preserve any multiwire information in a set of memory registers (this action is called a strobe) and also caused the EVENT FAST logic unit to be latched so that no other coincidences could be registered until a CLEAR signal was issued. The electronics in the counting room determined whether the event was to be processed further. A coincidence between a left and right plastic and NaI detector telescope generated an EVENT SLOW

FIGURE III-1

   .   Logic diagram of electronics located near
       scattering chamber.

TO EVENT FAST LATCH

COMPUTER NOT BUSY

FROM MASTER GATE FAN OUT

CLEAR

READ

STROBE

MWPC CONTROLLER

EVENT FAST

LATCH

72 ns

72 ns

L FAST OR

R FAST OR

ADC L0

ADC L2

ADC R0

ADC R2

PLASTIC LF

NaI LF

NaI LB

PLASTIC LB

PLASTIC RF

NaI RF

NaI RB

PLASTIC RB

PULSER FANOUT

TO MWPC's

LEGEND

FROM OTHER LOGIC

TO OTHER LOGIC

TO CAMAC ADC.TDC.DCR

TO SCALER

VETO INPUT

COMPLIMENTARY OUTPUT

DISCRIMATOR

AMPLIFIER

DELAY

OR

AND

INT
INTEGRATOR

PUG
PILE-UP GATE

CF
CONSTANT FRACTION DISCRIMINATOR

ATT
ATTENUATOR

FIGURE III-2
        First of two logic diagrams of electronics
        located in remote counting room.
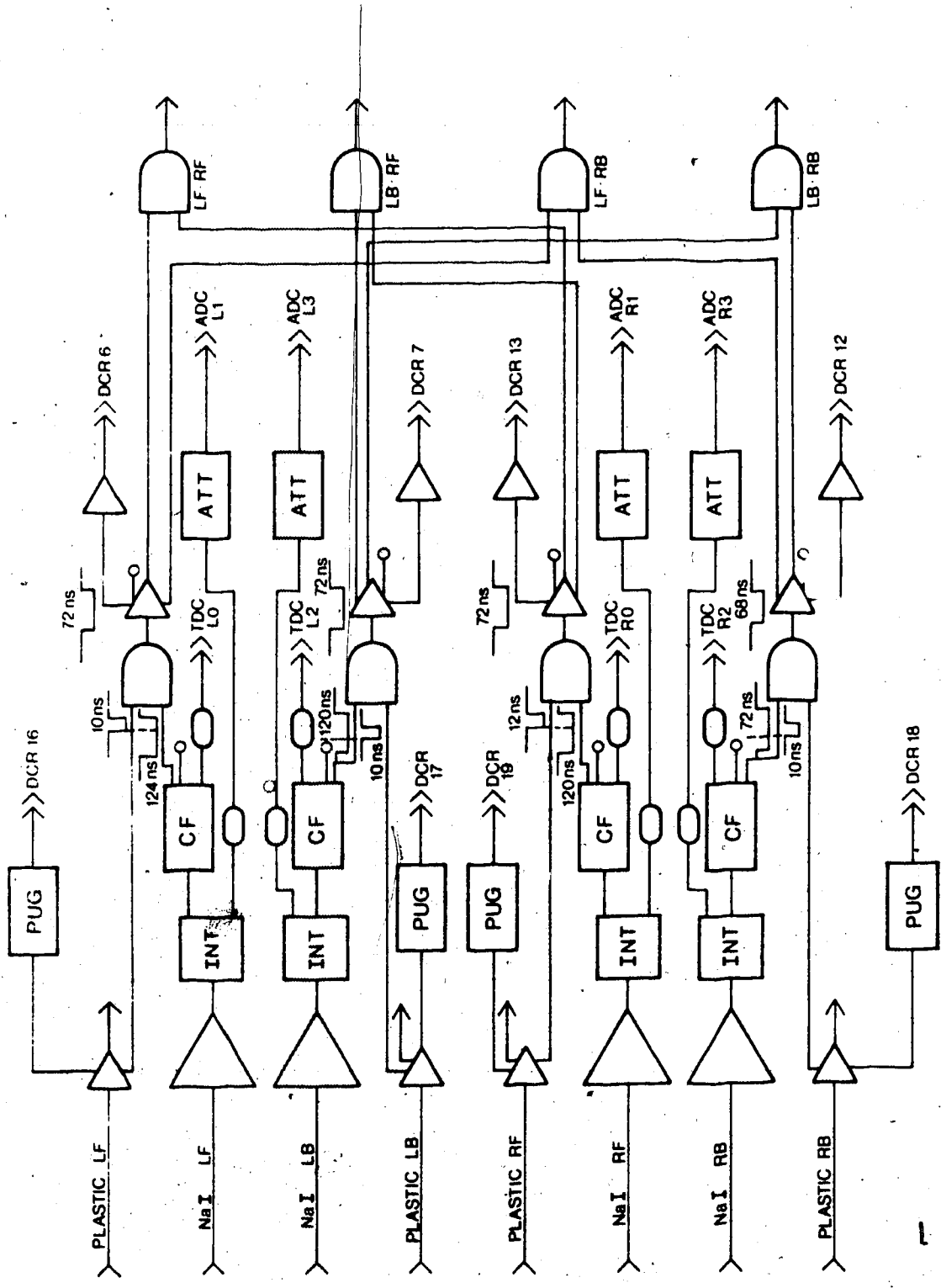
FIGURE III-3
        Second of two logic diagrams of electronics
        located in remote counting room.
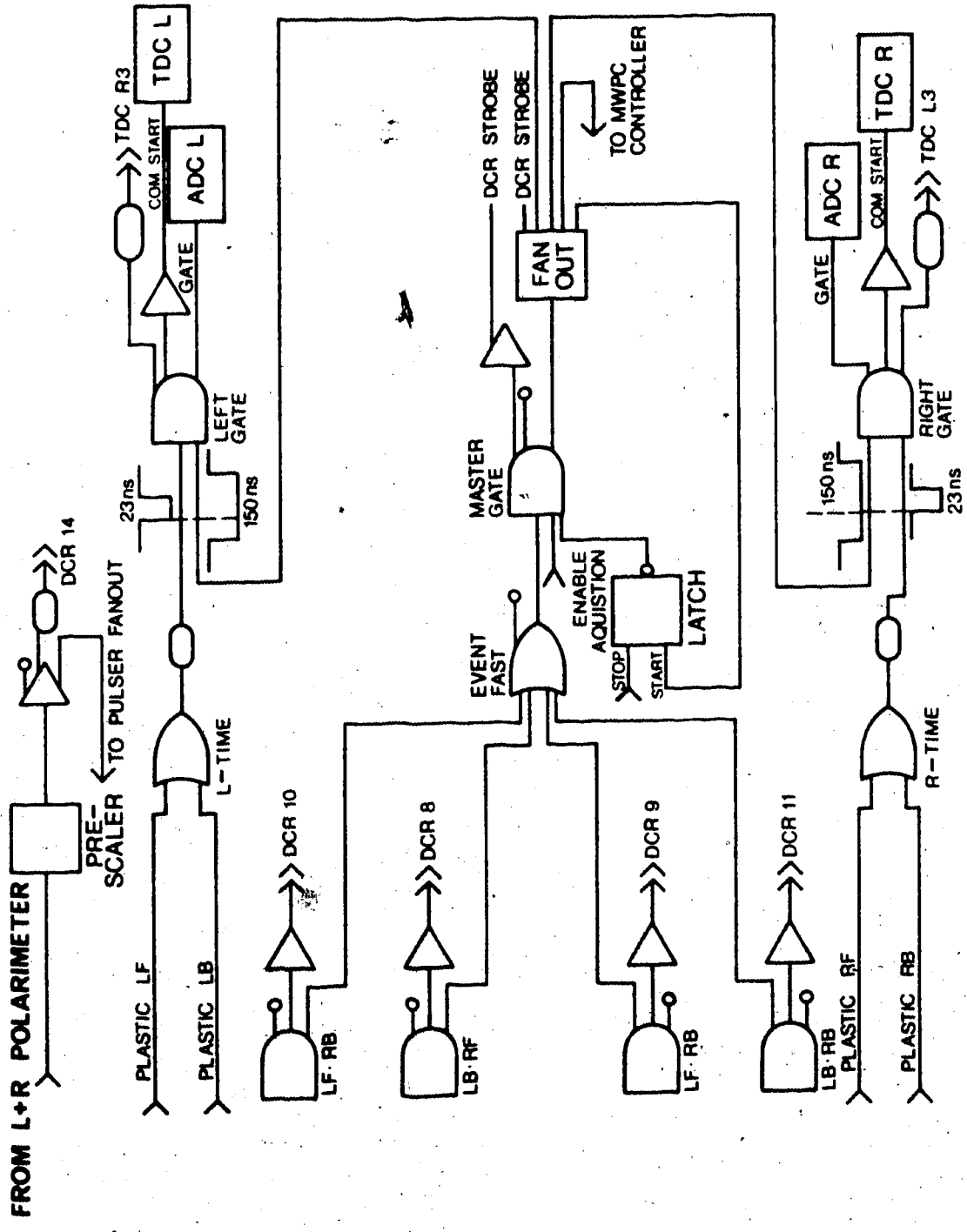
(MASTER GATE) signal. This latched the MASTER GATE and signaled the system to transmit the MWPC information to the computer through CAMAC. If a MASTER GATE was not generated within 1 µs of the strobe, the MWPC controller would generate an internal CLEAR which cleared the multiwire memories and disabled the EVENT FAST latch so that further coincidences could be processed. If a MASTER GATE occurred, the system processed the information until it was ready for the next event at which time the computer issued a COMPUTER NOT BUSY signal. This generated a CLEAR which was sent to the MWPC controller and which released the latches on the EVENT FAST and SLOW logic.

Following a MASTER GATE, CAMAC ADC's were turned on for a fixed length of time (a GATE) to integrate the signals from the plastic and NaI detectors, and time-to-digital converters (TDC's) were started. The ADC's were multi-input (12-fold) charge integrating types with 256 pC corresponding to full scale (1024 channels). The ADC gates used were 400 ns wide. The constant fraction devices shown in Figure III-2 provided a sharp timing signal when the height of the NaI signal had risen a pre-specified fraction of the full peak height (0.2 in this experiment). The widths of the pile-up gates were 9.0 to 9.4 µs. There were separate sets of ADC's and TDC's for the left and right detectors. To ensure that a left (right) detector gated or started the left (right) ADC's or TDC's respectively, the signals to initiate these processes were derived by ANDing the MASTER GATE signal with

a suitably delayed signal from the left (right) plastic. This is called retiming.

A TDC unit has a number of inputs each of which is stopped by a separate signal and all of which have a common start. In addition to using timing signals from the plastics and NaI detectors as stops, every second signal from the radio-frequency (rf) oscillations of the cyclotron was employed as well. The resulting timing right versus rf (start=right, stop=every second rf pulse) spectrum encompassed two beam bursts. A typical spectrum is shown in Figure III-4. If the cyclotron becomes slightly mistuned, some of the accelerated H^- ions that pass the stripper foil slip out of phase with the rf by ~180°, experience deceleration, and are subsequently extracted by the stripper foil resulting in a decelerated beam. Data acquired during periods having large amounts of decelerated beam have a spectrum such as the one shown in Figure III-5. As discussed in Chapter IV, decelerated beam data had no objectionable features and was not treated differently from other data. One of the stopping signals on the left (right) TDC consisted of a suitably delayed signal from the right (left) side. A typical left-right timing (start=left, stop=right plastic) spectrum is shown in Figure III-6. The first and third peaks are random coincidence events consisting of protons from successive beam bursts. The middle peak consists of prompt (real+random) events (from the same beam burst).

The DCR units shown in Figures III-2 and III-3 are

FIGURE III-4

Timing spectrum for start-right plastic; stop-every second rf pulse. Counts are LF-RB ($25°-67°$) events with ^{40}Ca target and with no decelerated beam present.

FIGURE III-5

Timing spectrum for start-right plastic, stop-every second rf pulse. Experimental conditions are as for Figure III-4 along with the presence of decelerated beam.

FIGURE III-6

Timing spectrum for start-left, stop-right plastic. Counts are LF-RF ($30°-30°$) events with a ^{40}Ca target.
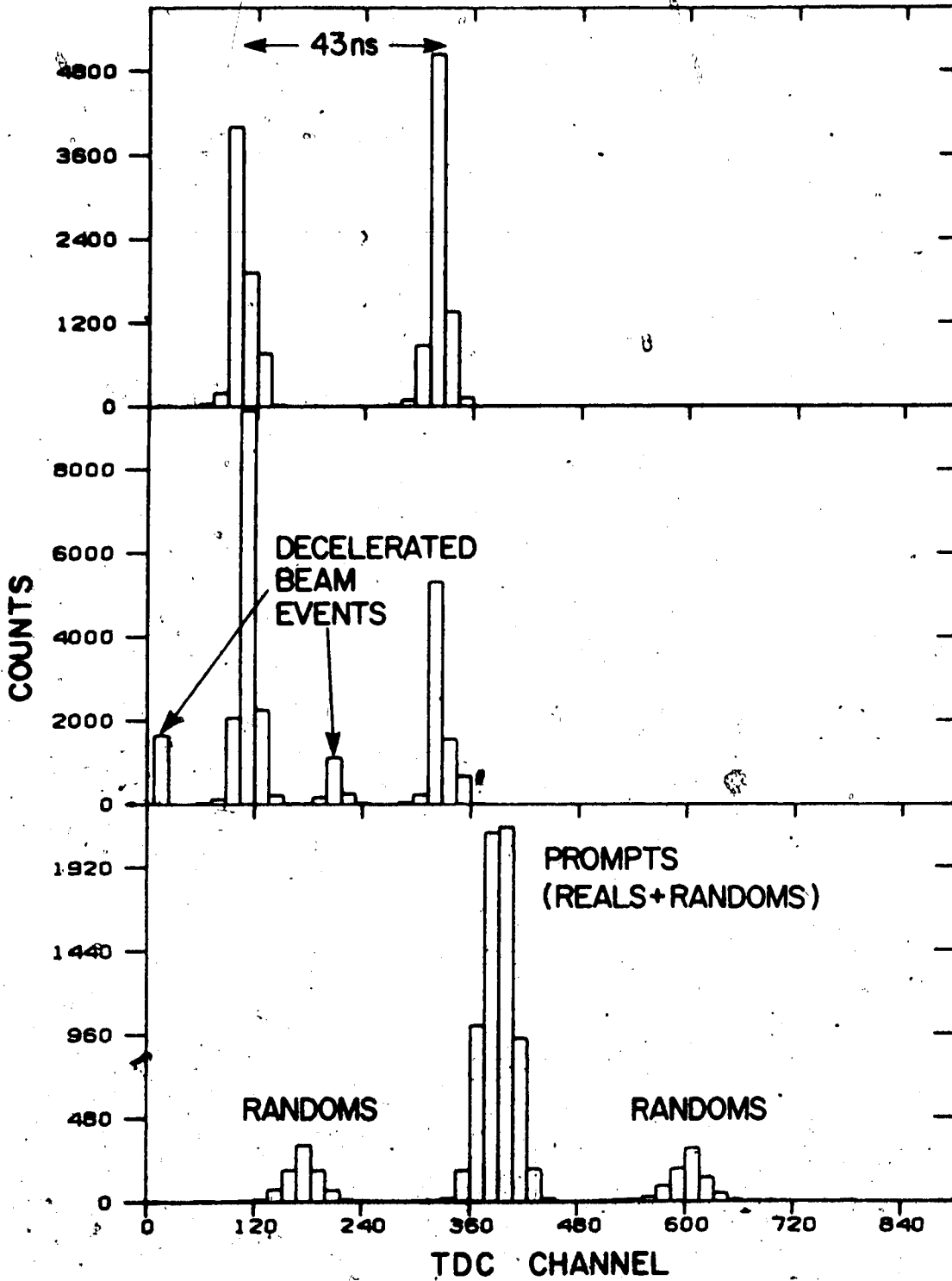
CAMAC digital coincidence registers (or bit pattern units) consisting of 24 bits. For each MASTER GATE, the contents of the register were sent to the computer with each bit representing the status of its input. Table I shows the DCR assignments used in the experiment. To record the total number of counts from certain devices over the course of the experiment, CAMAC scalers were used. The quantities scaled in this experiment are listed in Table II, and the positions of some of these scalers are indicated in Figures III-1, III-2, and III-3.

While the computer is processing a previous event, the latch on the MASTER GATE could result in the loss of new events. This computer dead-time must be taken into account. In addition, the electronics preceding the MASTER GATE could contribute to the overall dead-time (although this effect is usually negligible compared to computer dead time). For the purposes of monitoring both the electronic and computer dead-times and to present a constant amplitude signal for calibration, pulser pulses, which were scaled (1 pulse for every 2^5) L+R polarimeter counts, were fed to the plastic and NaI LED's.

The information received by the computer was processed and, for each MASTER GATE, an event record was written on magnetic tape. A list of the contents of an event record is shown in Table III. In the table, LAM PATTERN refers to the CAMAC look-at-me signal issued when a CAMAC crate required the attention of the computer. The events written on tape

TABLE I

DCR Assignments

DCR Number	Assignment
0-5	Not used
6	LF (NaI·P1)
7	LB (NaI·P1)
8	LBRF
9	LFRB
10	LFRF
11	LBRB
12	RB (NaI·P1)
13	RF (NaI·P1)
14	Pulser
15	Beam on
16	Pile Up LF
17	Pile Up LB
18	Pile Up RB
19	Pile Up RF
20	Spin Up
21	Spin Down
22-23	Not used

TABLE II

Parameters Scaled and Stored in Header and Trailer Blocks*

Scaler Number	Parameter
1	Ion Chamber
2	Event Slow Coincidence Presented
3	Master Gate
4	Elapsed Time (100 Hz Clock)
5	Polarimeter Left
6	Polarimeter Right
7	Not Used
8	Not Used
9	LBRF Coincidence
10	LFRB Coincidence
11	LFRF Coincidence
12	LBRB Coincidence
13	Polarimeter Left Accidentals
14	Polarimeter Right Accidentals
15-17	Not used
18	Polarimeter Left+Right
19	Polarimeter Left+Right (Prescaled)
20	Polarimeter Left+Right Accidental
21	Pulser (=Polarimeter Left+Right Prescaled)
22-24	Not used
25	LF (NaI·Pl)
26	LB (NaI·Pl)
27	RB (NaI·Pl)
28	RF (NaI·Pl)
29-32	Not used
37,33	NaI LF
38,34	NaI LB
39,35	NaI RB
40,36	NaI RF
45,41	Not used
46,42	Pulser (=Polarimeter Left+Right Prescaled)
47,43	Event Fast
48,44	Event Fast Coincidence Presented
53,49	Plastic RF
54,50	Plastic LF
55,51	Plastic RB
56,52	Plastic LB

*   In cases where a parameter has two scaler numbers, the
    second number corresponds to an overflow scaler.

TABLE III

Event Record Structure

Word Number	Parmeter	Comment
0	-(Length of Event)	
1	Flag (-1 or -2)	
2	LAM PATTERN	
3	IR Hi	Not used
4	IR Lo	Not used
5-6	DCR (24 bits)	
7	TDC L0	Left Start,Stop= NaI LF
8	TDC L1	rf
9	TDC L2	NaI LB
10	TDC L3	R Plastic
11	TDC R0	Right Start,Stop=NaI RF
12	TDC R1	rf
13	TDC R2	NaI RB
14	TDC R3	L Plastic
15	ADC L0	Plastic LF
16	ADC L1	NaI LF
17	ADC L2	Plastic LB
18	ADC L3	NaI LB
19	ADC L4	Spare-Not used
20	ADC R0	Plastic RF
21	ADC R1	NaI RF
22	ADC R2	Plastic RB
23	ADC R3	NaI RB
24	ADC R4	Spare-Not used
25-26	Scaler	Ion Chamber
27-28	Scaler	Event Fast
29-30	Scaler	Master Gate
31-32	Scaler	Time
33-34	Scaler	Polarimeter Left
35-36	Scaler	Polarimeter Right
37	MWPC	Number of hits + 1
38-end	MWPC	Coordinates

were organized into runs. At the beginning (end) of each run, a header (trailer) block was written which included the contents of the scalers listed in Table II. By subtracting the header block scalers from the corresponding trailer block scalers, the accumulated values for the run were obtained. For a given run, the angles of the detector booms were kept constant as was the polarization direction of the beam. Successive runs recorded on a single tape were separated by an end of file (EOF) mark, while the last run was followed by a double EOF mark. As well as processing the information and writing events on tape, the acquisition program recorded the scalers and kept a set of histograms for on-line analysis of the data. The spectra stored in memory are listed in Appendix II, along with their DCR gating requirements.

During the experiment, the detectors were positioned at various angles by remotely controlling the booms. The pairs of detector angles for which coincidence data were acquired are shown in Table IV. Data for each row of angle pairs in this table were acquired simultaneously. CD_2 and ^{40}Ca data were acquired for the same angle pairs in order to allow further calibration of the NaI detectors using (p,2p) on ^{12}C or deuterium. Data were taken with the CH_2 target to provide calibration points for the NaI detectors from free p-p scattering. Only the angle pairs 57°-30°, 30°-57° and 44°-44°, from the various CH_2 angle pairs, provided calibration information.

TABLE IV

Angle Pairs of Data Taken During Experiment

^{40}Ca and CD_2 Targets

LB-RF	LF-RB	LF-RF	LB-RB
54°-30°	30°-54°	30°-30°	54°-54°
49°-35°	30°-54°	30°-35°	49°-35°
67°-25°	25°-67°	25°-25°	67°-67°
52°-40°	30°-62°	30°-40°	52°-62°
47°-29°	29°-47°	29°-29°	47°-47°

CH_2 Target

LB-RF	LF-RB	LF-RF	LB-RB
57°-30°	30°-57°	30°-30°	57°-57°
44°-25°	25°-44°	25°-25°	44°-44°
63°-44°	44°-63°	44°-44°	63°-63°

Using the ^{40}Ca target, typically 3 to 5 tapes were
acquired at each set of angle pairs and each polarization
direction. Approximately two tapes (one third of a tape) of
data were acquired for each set of angle pairs for the CD_2
(CH_2) target. One tape contains roughly 150,000 events
divided among the 4 detector coincidence combinations.

CHAPTER IV

EVENT ANALYSIS

4.1 Introduction

The reduction of the information on the tapes to the final results can be divided into two phases. In the first phase, all events for a given beam polarization direction, detector coincidence combination, and angle pair were binned into two dimensional histograms containing prompt (reals+randoms) or random events. The histogram axes were T_1+T_2 (ESUM) and T_1-T_2 (EDIF). T_1 and T_2 are the kinetic energies of the protons at the target. With appropriate corrections, these numbers were converted into cross sections. This chapter discusses the first phase of the analysis in considerable detail. Readers who desire only a general understanding of this phase are advised to read sections 4.1, 4.2, and 4.14.

The quantity EDIF for three of the four detector coincidence combinations (LF-RB, LF-RF, LB-RB) was defined as $T_{left}-T_{right}$. Since some of the angle pairs for the RF and LB detectors were the same as those for the LF and RB detectors, data for LB-RF was binned as $T_{RF}-T_{LB}$. With this convention and for similar angle pairs, a spin ↑ run for LF-RB would be equivalent to a spin ↓ run for LB-RF - thus spin ↑ (↓) LB-RF data was treated as spin ↓ (↑) data. Due to different ESUM resolutions and accuracy of the energy calibrations between LB-RF and LF-

45

RB, events from these detector combinations were always binned in separate histograms.

The data are organized in ESUM versus EDIF histograms because a single particle state is characterized by a unique binding energy, BE. If T_0 is the incident energy and T_3 is the energy of recoil for a (p,2p) reaction, then

(IV.1) $T_1 + T_2 = T_0 - BE - T_3$.

As the recoil energy of the residual nucleus (T_3) is quite small for ^{40}Ca(p,2p) (less than 0.55 MeV for recoil momenta less than 200 MeV/c), the cross section for a single particle state should peak at a nearly fixed value of ESUM independent of EDIF. Varying EDIF while keeping ESUM fixed changes the recoil momentum allowing the examination of the momentum dependence of a single particle state. As the cross section for a state changes rather slowly as a function of recoil momentum, the EDIF bin size is 20 MeV. The ESUM bin size is chosen to be 1.0 MeV since this is 1/3 to 1/4 of the summed energy resolution (FWHM) attained in this experiment.

In the second phase of the analysis, which is discussed in the next chapter, cross sections for each of the $1d_{3/2}$, $2s_{1/2}$, and $1d_{5/2}$ single particle states were extracted by fitting Gaussian peaks to ESUM spectra for the different 20 MeV EDIF ranges. As there were data for both polarization directions, the results of the fitting were converted into unpolarized cross sections (σ_0)

and analysing powers (A_y) for each single particle state
as a function of EDIF and angle pair.

4.2 Overview

An outline of the first phase of the analysis follows.
This po   the data analysis was performed on a Data.
General   00 computer. The tape reading software is
descr   N-78) while the remainder of the event
analysis software was developed specifically for this
experiment. For a given run, the data were subjected to a
number of cuts and the surviving events were binned into
eight ESUM versus EDIF histograms. By means of windows on
the left-right timing (start=left, stop=right plastic),
events were binned either into a prompt event histogram
(corresponding to the central peak of Figure III-6) or a
random event histogram (corresponding to the left and right
peaks of Figure III-6) for each of the four detector
coincidence combinations. The assumption was made that the
energy distribution for random coincidence events
originating from two beam bursts was the same as that for
random coincidence events arising from a single beam burst.
Since both random coincidence peaks were included to
increase statistical accuracy, the random event histogram
contained twice the actual random background correction.
The counts (divided by two) in the random event histogram
were subtracted from the counts in the corresponding prompt
event histogram before the cross sections were computed.

Criteria (cuts) used to reject events from the data

were applied equally to the prompt and random data. Some of these cuts, although necessary, eliminate valid events and compensating corrections were necessary to avoid biasing the final cross sections. For this reason, during the reduction of each run, statistics and correlations were acquired from which correction factors were calculated.

4.3 NaI Detector Efficiency and Solid Angle Definition

For a given particle energy, the efficiency of a NaI detector is nearly constant over its central region and drops off sharply near the outer circumference due to out-scattering (CA-77). The radius of the central plateau decreases with increasing particle energy. The energy dependence of the NaI efficiency in the plateau is given in Table V. For energies greater than 150 MeV, these efficiencies include the effect of inserting enough copper to degrade the energy to ~135 MeV. A correction factor consisting of the product of the NaI efficiencies for the detector energies of the two protons has been incorporated into the calculation of the cross sections.

The MWPC coordinates were used to define circular windows centered on the faces of the four NaI detectors. The center of each of these windows was established by examining the distributions of $^{40}Ca(p,2p)$ events on x versus y histograms. The radius of these windows was chosen on the basis of histograms such as the one shown in Figure IV-1. This illustrates the radial distribution of (p,2p) events per unit area from the center of the detector

TABLE V

NaI Efficiency versus Incident Proton Energy

Energy (MeV) (MeV)	Efficiency ε_0	Uncertainty in ε_0
10	0.998	–
20	0.994	–
30	0.987	–
40	0.978	–
50	0.968	–
60	0.958	–
70	0.947	–
80	0.935	–
89	0.931	0.0050
104	0.916	0.0021
139	0.866	0.0055
147	0.844	0.0015
210	0.757	0.0063
221	0.728	0.0030

Values for 10 to 80 MeV from (CE-69),

for 89 to 221 MeV from (CA-77).

FIGURE IV-1

Counts per unit area for each of the 4 NaI
detectors as a function of distance (in
wires, wire spacing = 2mm) from the center
of the detector. Counts are LF-RB (30°-54°)
and LB-RF (49°-35°) events with a ^{40}Ca
target. Events falling outside a radius of
26 wires (indicated by arrows) were rejected
in the analysis.

DISTANCE FROM CENTER OF DETECTOR

51
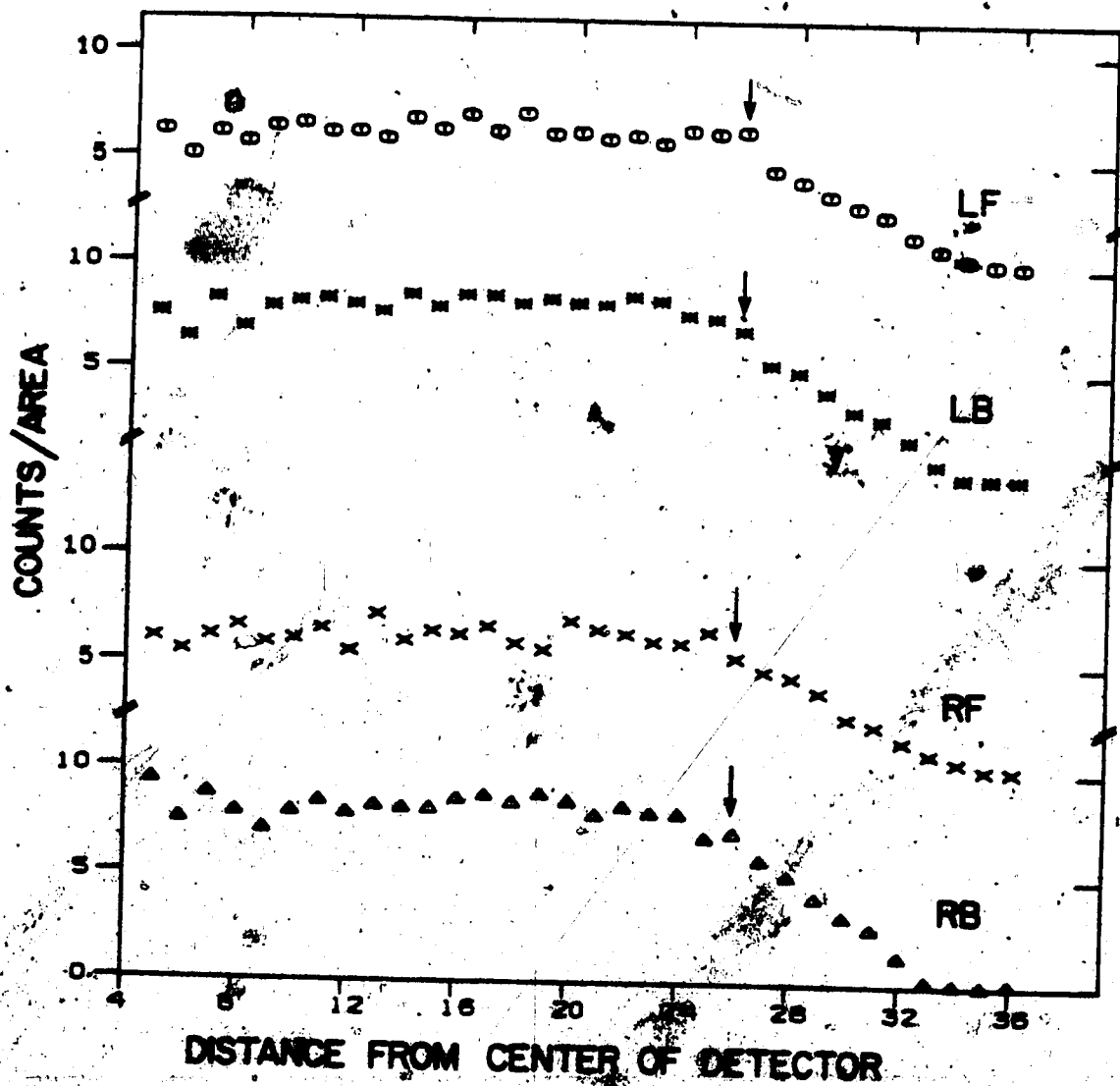
- the abscissa has units of wires (where the wire spacing is 2 mm). For each of the detectors, the central region is flat (as expected) and falls off beyond 26 wires. Thus, a common window radius of 26 wires was chosen for each of the detectors. The resulting solid angles are LF=4.72msr, RF=4.79msr, LB=6.36msr, and RB=6.43msr. Events outside these windows were rejected. The front (back) detectors subtended ~±2.6° (~±2.2°) at the target.

4.4 Multiwire Efficiency

Wires away from the edges of the multiwire planes are quite efficient (typically ≳99.5%). However, any event for which one (or more) of the four wire planes fails to register a hit must be rejected. For a certain fraction of these events, this missing coordinate would be within the window. Consequently, a correction consisting of the product of the efficiencies of the four participating multiwire planes is included in the calculation of the cross sections. For the x and y planes on one arm, the efficiencies are given by

$$(IV.2) \quad MWEFF_x = 1 - \frac{XMISS}{YHIT} \quad , \quad MWEFF_y = 1 - \frac{YMISS}{XHIT} \quad ,$$

where   XHIT, YHIT are the number of events within 26 wires of the center in X (Y),

XMISS, YMISS are the numbers of missings in X (Y) whose corresponding Y (X) coordinates were within 26 wires of the center.

Typically, the product of the efficiencies of the four

planes was ~0.99.

4.5 Pile-Ups and Multiple Hits

In the event analysis, events with a pile-up DCR bit
set for either detector arm were rejected. These
represented ~13% of the total number of events.
Approximately 0.5% of the events had pile-ups in both arms.
In adjusting the cross sections for the pile-up cut, each
pile-up was counted as representing a single (p,2p) event.
Any double (p,2p) events rejected by the pile-up criteria
were automatically accounted for in the computer dead-time
correction.

When a proton passes through a MWPC, it is most likely
that a single wire will be struck, although it is possible
that two or more wires (not necessarily consecutive) will
be struck. It is also possible that two particles may pass
through the plane within the resolving time, τ_{MW}, of
the plane (~100ns) causing two distinct sets of struck
wires. Furthermore, two particles passing through the
telescope sufficiently close in time will fail to be
resolved by the pile-up monitor and thus the pile-up DCR
bit will not be set.

The span of a struck plane is defined as the number of
wires from the leftmost (or topmost) struck wire to the
rightmost (or bottommost) struck wire. Thus, a single
struck wire has a span of one, two struck wires separated
by a gap of two wires has a span of four and so on. If the
assumption is made that only a single particle passes

through each wire plane per event, then a reasonable definition of the position of this particle is the sum of struck wire coordinates divided by the number of struck wires (centroid). However, for large spans, the concern arises whether two particles have in fact passed through the plane or whether a single particle has produced a large span (for example, by ejecting a δ-ray to one side). In either case, as the span increases, confidence that the calculated centroid represents the actual centroid of the particle(s) rapidly erodes as there is no reason to assume that the span is symmetrical about the position of the particle(s).

The distribution of events for the y plane of the LF MWPC is plotted as a function of span in Figure IV-2. This distribution is typical of all the wire planes and it was decided to reject events for which any one of the 4 planes recorded a span greater than 4 wires. Such events are referred to as multiple hits. After pile-up events were rejected, 12% of the remaining events were found to be multiple hits including 0.5% which had spans greater than four on all four wire planes (quadra-multiple events). No account was taken for the fraction of the quadra-multiple events which may have been double (p,2p) events and all multiple hit events were treated as single (p,2p) events with the final cross sections being corrected accordingly.

FIGURE IV-2

Distribution of events (expressed as the percentage of total) passing through y plane (LF at 25°) as a function of span. Events with spans greater than 4 (indicated by the arrow) were considered multiple hits.
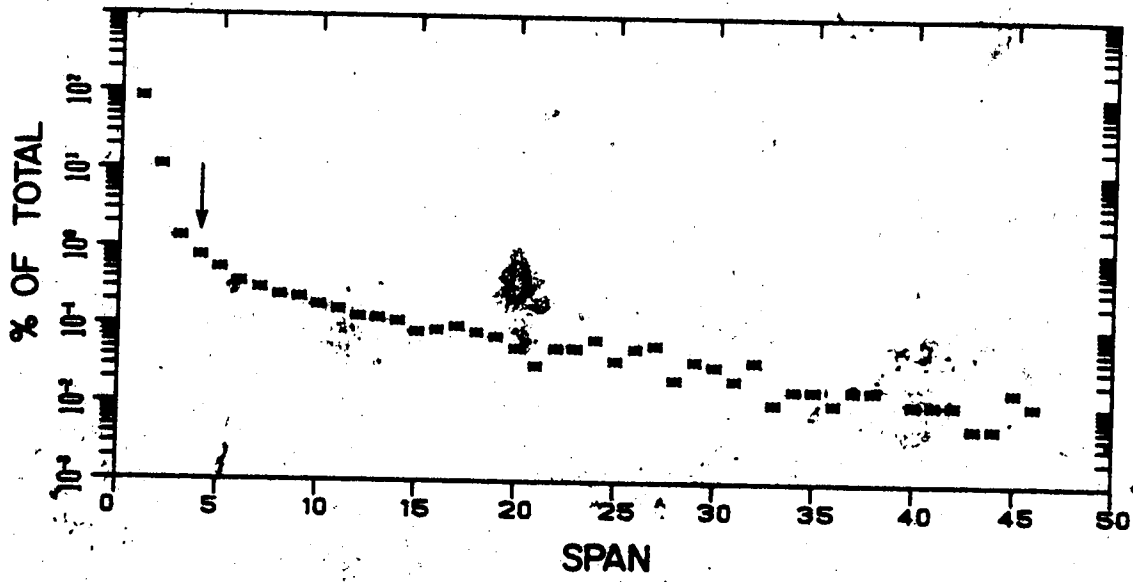
4.6 Elimination of Free p-p Events

The calcium target used in the experiment contained substantial amounts of hydrogen ($H/^{40}Ca \sim 0.23$ in atoms) as discussed in section 4.13. All the angle pairs for LB-RF and LF-RB (with the exception of 47°-29° and 29°-47°) overlapped with free p-p scattering angles. The relatively large free p-p cross section (~ 10.6 mb/sr at 200 MeV at 43.6°) resulted in the presence of considerable numbers of free p-p events in the data. The peak for free p-p events is well separated from the (p,2p) data as shown in Figure IV-3 where T_{left} versus T_{right} is plotted for 30°-54° (LF-RB). However, energy losses suffered by elastic protons undergoing nuclear reactions in the NaI crystals result in two p-p reaction tails which extend into the (p,2p) region as can be seen in the figure. Free p-p events were eliminated by means of coplanarity and opening angle cuts applied to the data based on the distribution of Δx versus Δy where

(IV.3) $\quad \Delta x = x_{left} - x_{right} + 64$,

$$\Delta y = \frac{(y_{left} + y_{right})}{2} \quad .$$

Δx and Δy correspond to the opening angles in the horizontal and vertical planes respectively. Such a distribution for events from the free p-p peak (isolated from the $^{40}Ca(p,2p)$ events by means of applying suitable windows to the NaI signals from both arms) for 30°-54° is

FIGURE IV-3

Scatter plot (logarithmic density scale) for T_{LF} versus T_{RB}. Counts are LF-RB (30°-54°) events with a ^{40}Ca target. The (p,2p) loci as well as the free p-p peak and reaction tails are labelled. The reaction tail on the low energy side (LB) is only barely visible.

Figure showing a two-dimensional scatter plot with axes T_{RB} (MeV) (vertical) ranging from 26 to 154, and T_{LF} (MeV) (horizontal) ranging from 26 to 154. Labels on the plot: $^{40}Ca(p,2p)$ LOCI, FREE p-p PEAK, and p-p REACTION TAILS.
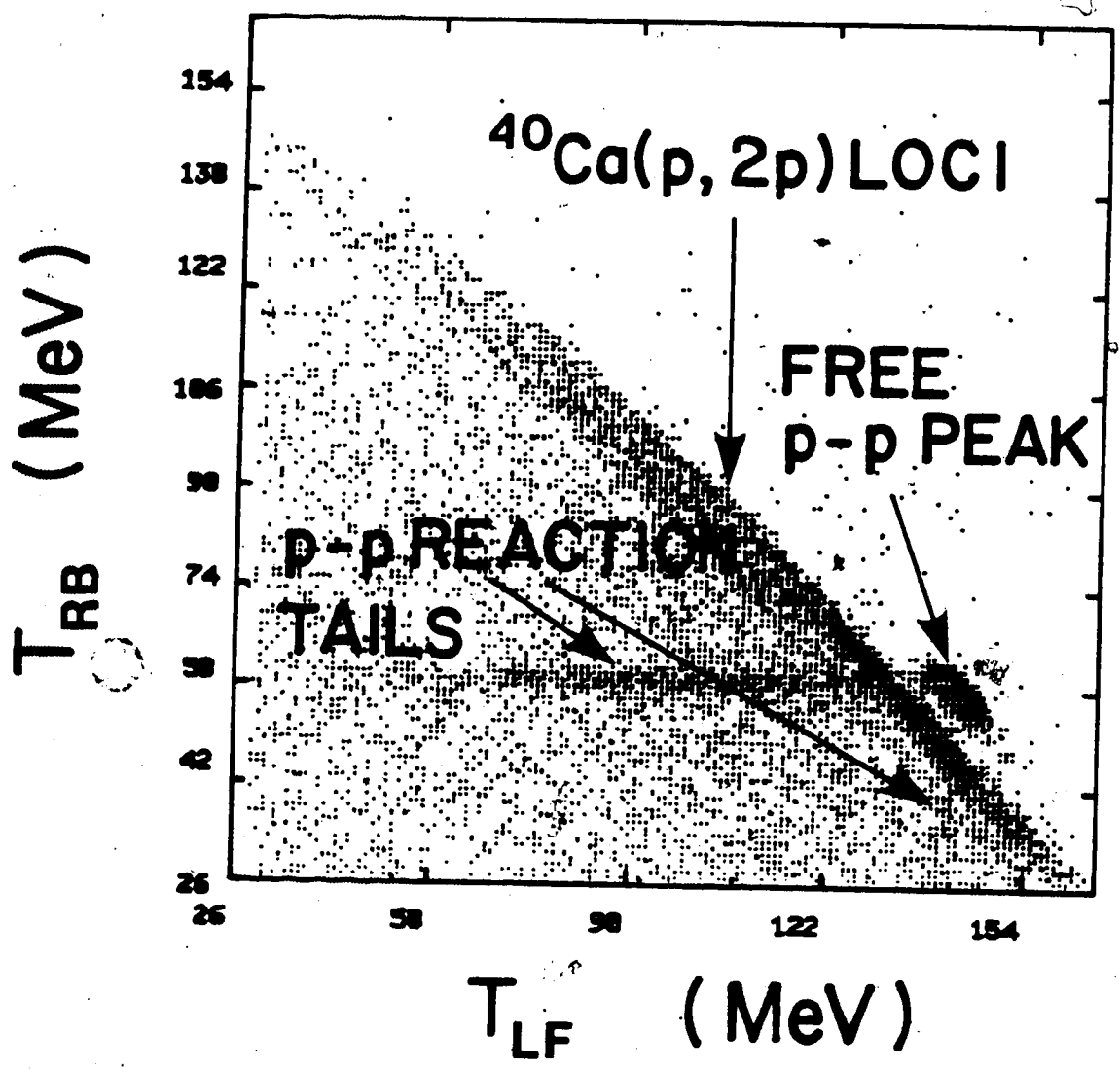
shown in Figure IV-4. Eliminating all events which fell within a rectangular window surrounding this distribution (shown in Figure IV-4) resulted in the T_{left} versus T_{right} distribution shown in Figure IV-5 (which is to be compared with Figure IV-3). This method, which we refer to as the elastic cut, required a different window in Δx versus Δy for each angle pair of LB-RF and LF-RB. It eliminated >96% of the free p-p events.

However, it also excluded a fraction of the (p,2p) events. To estimate what fraction of (p,2p) events were being rejected, the elastic cuts were applied to runs not containing free p-p events (47°-29° and 29°-47°). By counting the numbers of events eliminated, we obtained a correction factor for each elastic cut. This correction factor was incorporated in the calculation of the cross sections. The size of the correction varied with the Δx versus Δy window size and ranged from 1% to 19% due to varying degrees of overlap with free p-p angles.

4.7 NaI Calibration and Energy Resolution Optimization

In order to bin events in the ESUM versus EDIF histograms, pulse heights from the left and right NaI detectors were converted into energies. To do this, a number of factors had to be taken into account. The relationship between NaI pulse height and energy was nonlinear. In addition, the NaI ADC pedestals, zero offsets due to a dc level added to each NaI signal, were not negligible. Since the accuracy in determining the

FIGURE IV-4

Scatter plot (logarithmic density scale) for Δx versus $\Delta y/2$ (proportional to opening angles in the horizontal and vertical planes respectively). Counts are LF-RB ($30°-54°$) events with a ^{40}Ca target. The free p-p events (selected by software windows) and the few remaining (p,ℓp) events are labelled. Events falling within the rectangular region were rejected in the analysis.

^{40}Ca(p,2p) EVENTS

FREE p-p EVENTS

ΔY/2 (WIRES)

ΔX (WIRES)
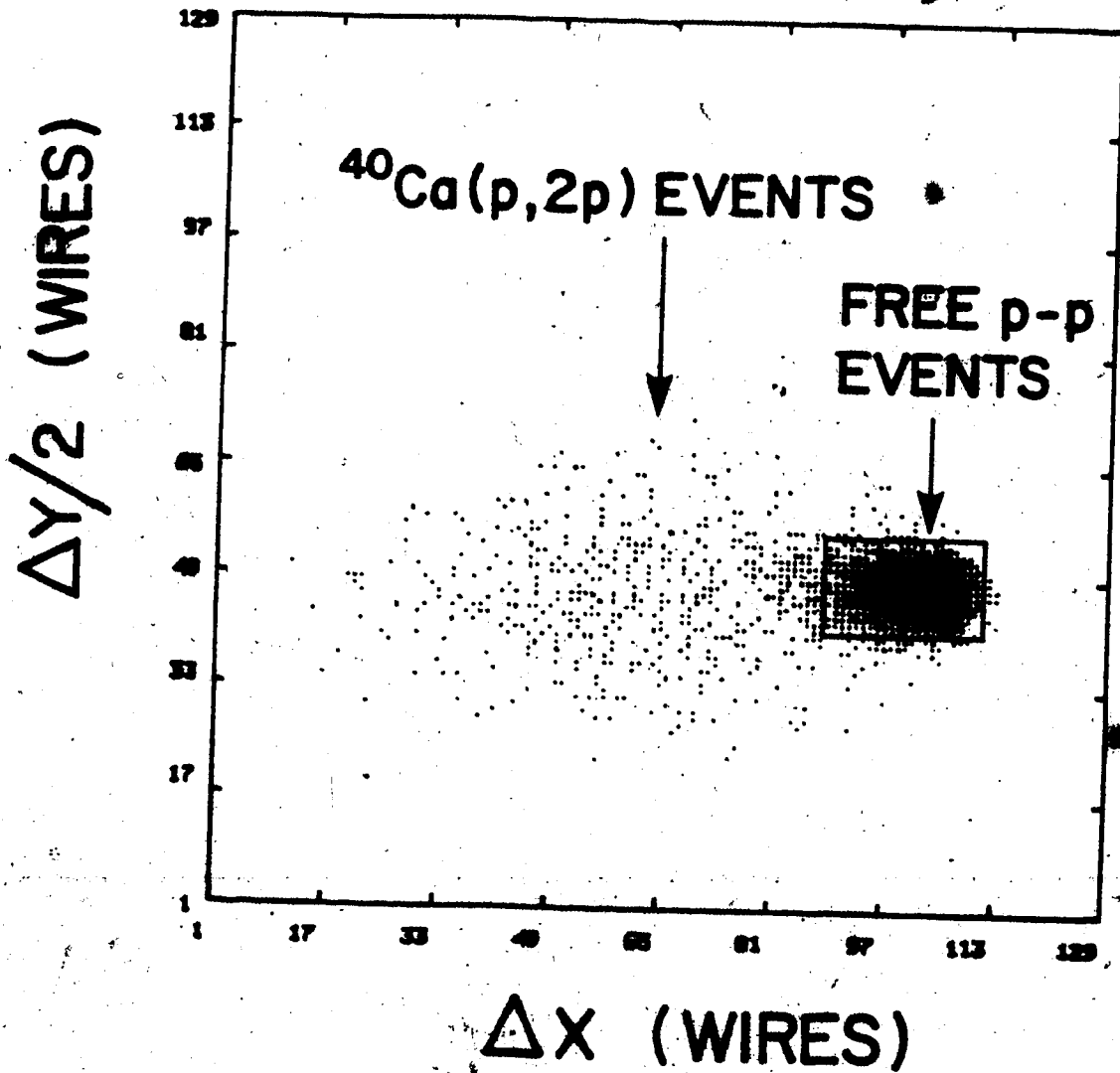
FIGURE IV-5

Scatter plot (logarithmic density scale) for T_{LF} versus T_{RB}. Conditions are the same as for Figure IV-3 but with all events falling within the rectangular window shown in Figure IV-4 rejected. Although >96% of the free p-p events have been eliminated, the p-p peak is still visible because of the logarithmic scale.

$^{40}Ca(p,2p)$ LOCI

FREE p-p PEAK
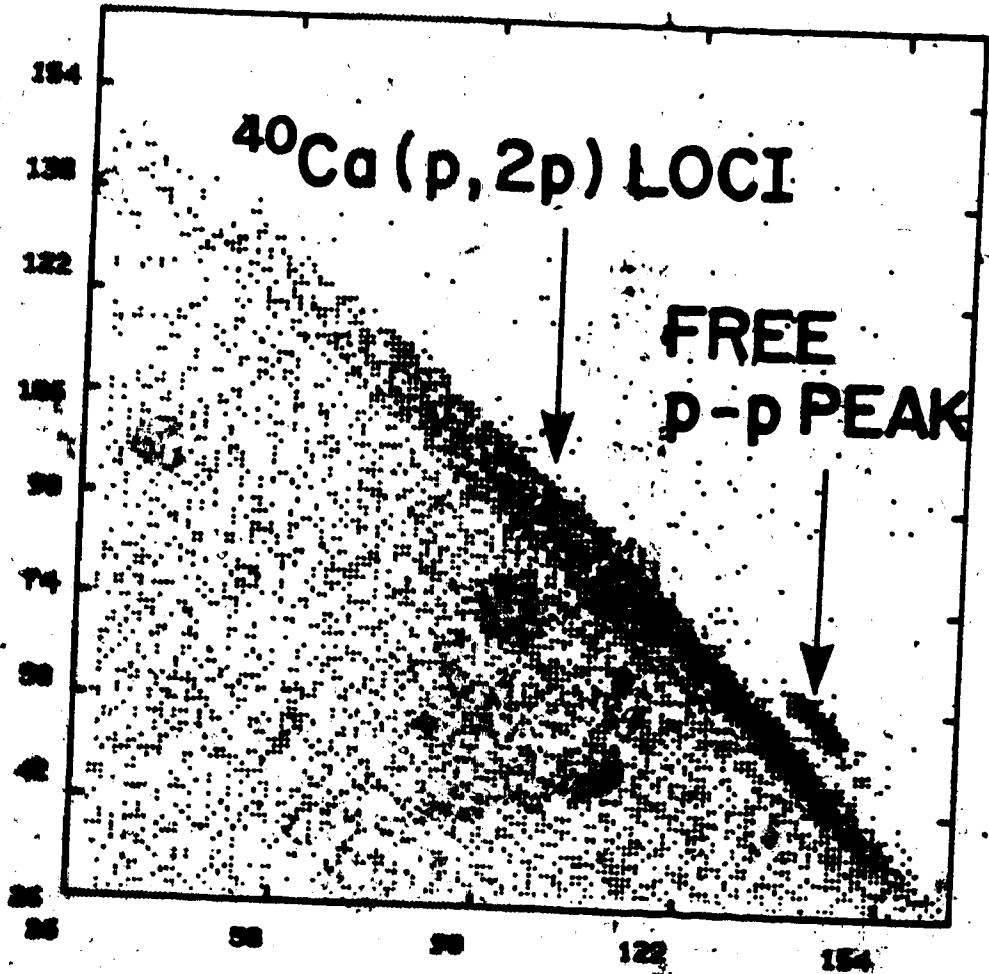
cross sections of the single particle states depended
strongly upon the degree to which the peaks were resolved,
it was worthwhile to invest considerable effort in removing
nonlinearities and minimizing effects that degraded the
energy resolution.

The free p-p scattering in the LF-RF and LF-RB ^{40}Ca
runs and in the CH$_2$ runs provided a number of well-defined
energy calibration points. Free p-p events were isolated
from the ^{40}Ca(p,2p) data by means of NaI pulse height
windows and, in addition, the left-hand-side protons were
required to pass through a 6 wire wide window in the x
direction. Since scattering angle and energy are
correlated for free p-p scattering, the ~0.6° window
served to define precisely the energies of the protons at
the target. The position of each x-plane window was chosen
and a restriction was applied to the y-coordinates in order
to guarantee that the protons in either arm passed within
the circular region of constant MWPC efficiency. This
minimized the reaction tails, making the precise
determination of the peak positions easier.

Protons emerging from the target passed through a
considerable amount of material (the target itself, the
scattering chamber window, air, the MWPC's, the plastic
scintillators, and caps on the fronts of the NaI detectors)
losing some of their energy before being stopped in the NaI
detectors. For calibration purposes, given the energies of
the free p-p protons after the interaction in the target,

their final values at the NaI detectors were required. Once the detectors were calibrated, the energy deposited in the NaI detector was used to obtain the scattered energy at the target. For both purposes, a table of values representing the energy-degrading materials between the target and the NaI detectors was necessary. A suitable table was compiled and is shown as Table VI. The energy losses experienced by protons passing through these materials were obtained from tables of stopping powers (SE-67). Energy losses suffered by 142 (547) MeV protons at the target reaching the front (back) NaI detectors were ~8.1 (~13.4) MeV.

For each CH_2 run and for the p-p elastic events in each ^{40}Ca run, the average value of the NaI pulse height for the free p-p peak was obtained. In addition, the average LED and pedestal pulse heights for each of the NaI detectors for these runs were obtained. A plot of average pedestal pulse height versus run number for each detector is shown in Figure IV-6. The common fluctuations among the four detectors are believed to be due to a combination of temperature effects and electronic noise while the origin of the similarity between the left or right pedestals is believed to originate in the ADC's. The fluctuations over the course of the experiment are on the order of 5 channels (~1.10 to 1.42 MeV depending on the detector) while the resolution (FWHM) for a given run ranged from 4 to 7 channels among the various detectors.

TABLE VI

Materials* for dE/dx Energy Loss Calculations

Region	Thickness·Density (gm/cm²) LForRF	LBorRB	Material	Comment
1	Dependent on angle and target		^{40}Ca, CD_2, CH_2	Target Energy Losses.
2	0.134	0.112	Air	Scattering Chamber window to front wire plane window.
3	0.033		Copper	MWPC wires and gas.
4	0.010		Air	Back wire plane window and air gap.
5	0.835	0.598	CH	Plastic Scintillator.
6**	5.667 LF 5.644 RF	–	Copper	Degrader.
7	0.583	0.250	CH_2	Material in front of NaI crystal.

* Note: Some materials in table are the stopping power equivalents of the materials they represent.

** Used only for LF, RF = 25°.

TABLE VII

Materials for dE/dx Energy Loss Calculations Adjusted for Nonlinearity Correction

Region	Thickness·Density (gm/cm²) LF	RF	LB	RB	Material
1-4	Same as in Table VIII				
5	0.500(0.835*)	0.835	0.460	0.295	CH
6*	5.170	5.644	–	–	Copper
7	–	0.183	–	–	CH_2

* Used only for LF, RF = 25°.

FIGURE IV-6

NaI pedestal pulse height centroids for each detector as a function of run number. Data shown are for ^{40}Ca runs while gaps correspond to acquisition of CH_2 or OD_2 data.

CENTROID

58 —
56 —
54 —
52 —
61 —
59 —
57 —
55 —
66 —
64 —
62 —
60 —
80 —
78 —
76 —
74 —
72 —

LF

LB

RF

RB

0   5   10   15   20   29   34   39   40   45   50
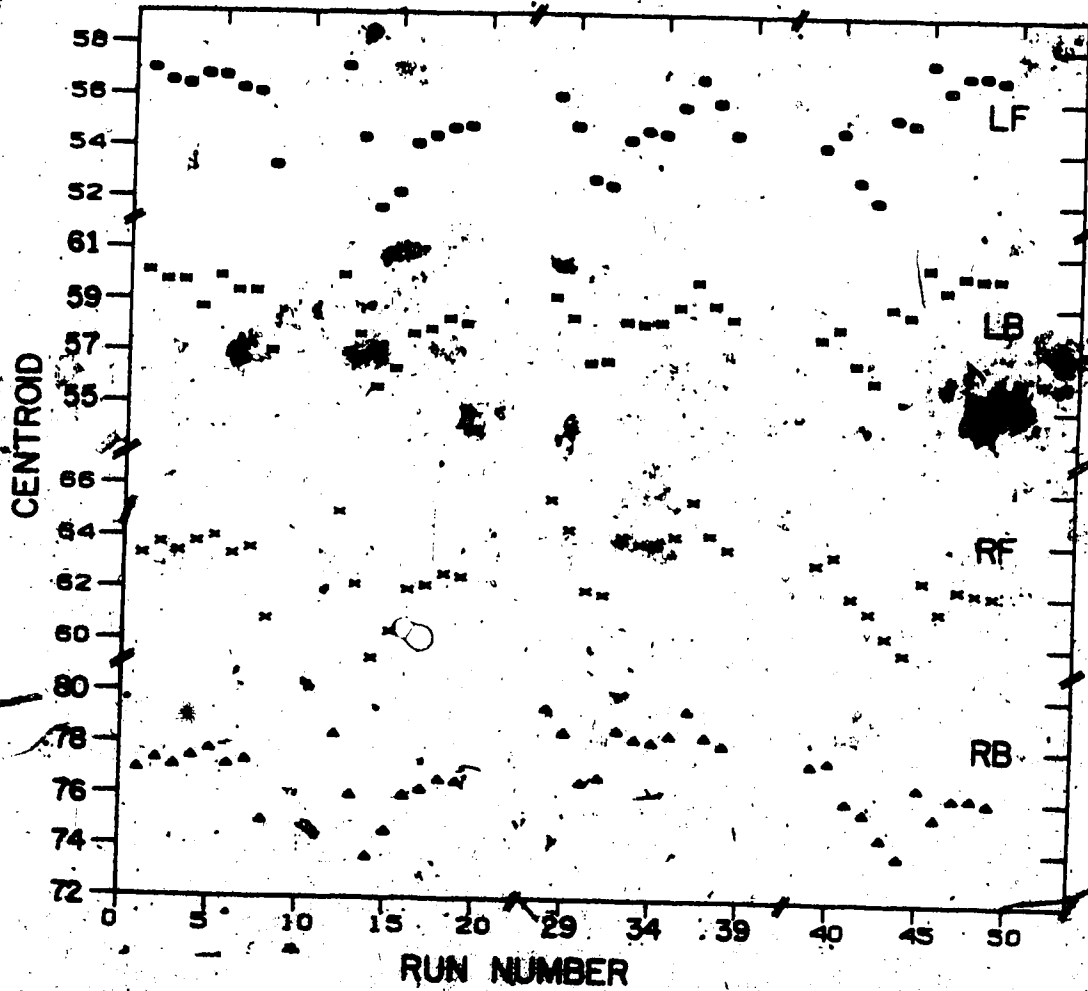
RUN NUMBER

LED pulse height (corrected for the pedestal) versus run number is plotted in Figure IV-7. The large shifts in gain (~20 to 45 channels), which are correlated among the 4 detectors, are very probably due to stability problems in the common pulser input to the LED's. The resolution of the LED peaks (FWHM) for a given run ranged from 11 to 16 channels among the four detectors. Finally, the average pulse height of the free p-p events (corrected for pedestal) versus run number is plotted in Figure IV-8. The ESUM resolution (FWHM) varied from 20 to 24 channels. Runs with the same detector angles are grouped together in the figure since the average pulse height for free p-p scattering varies with angle (data for Figures IV-6 and IV-7 were organized similarly to facilitate comparison). For data corresponding to a given set of detector angles, the variations are probably due to a combination of ADC fluctuations and individual detector base noise. The changes in the LED pulse heights are substantially larger than, and not obviously correlated with, those of the free p-p events. For this reason, the LED pulse heights were not used in the calibration of the NaI detectors. If the signal as output directly from the pulser driving the LED's had been recorded on an event-by-event basis, it might have been possible to remove these variations and the LED pulse heights would then have been quite useful in the energy calibration.

The method of calibration was as follows. Initially,

FIGURE IV-7

Nal LED pulse height (minus pedestal)
centroids for each detector as a function of
run number. Conditions as for Figure IV-6.
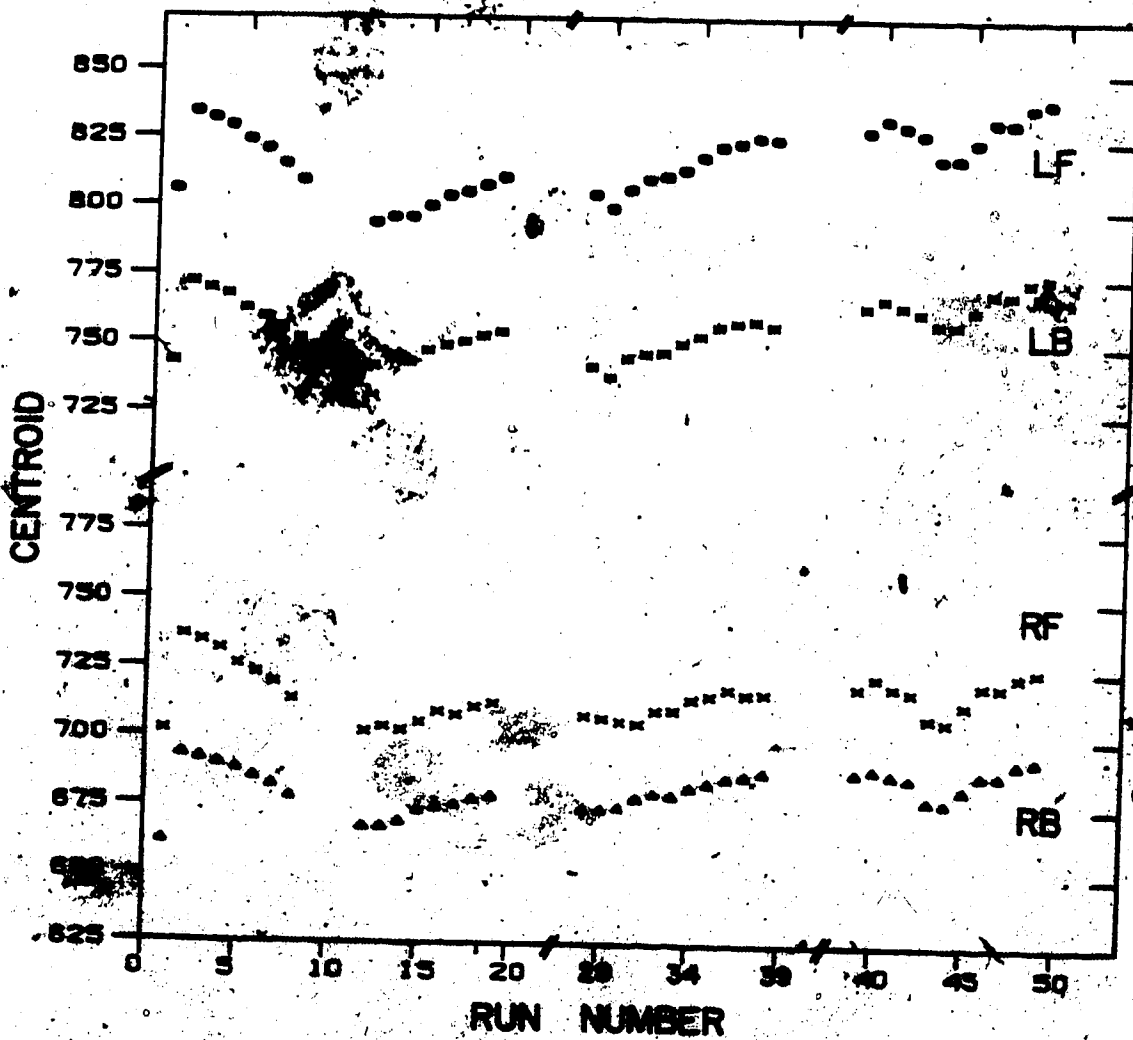
FIGURE IV-8

Free p-p NaI pulse height (minus pedestal) centroids for each detector as a function of run number. Data are from scattering from hydrogen contamination in ^{40}Ca target. For each set of data, the detector angle and the difference between the measured pulse heights and the plotted values are given.
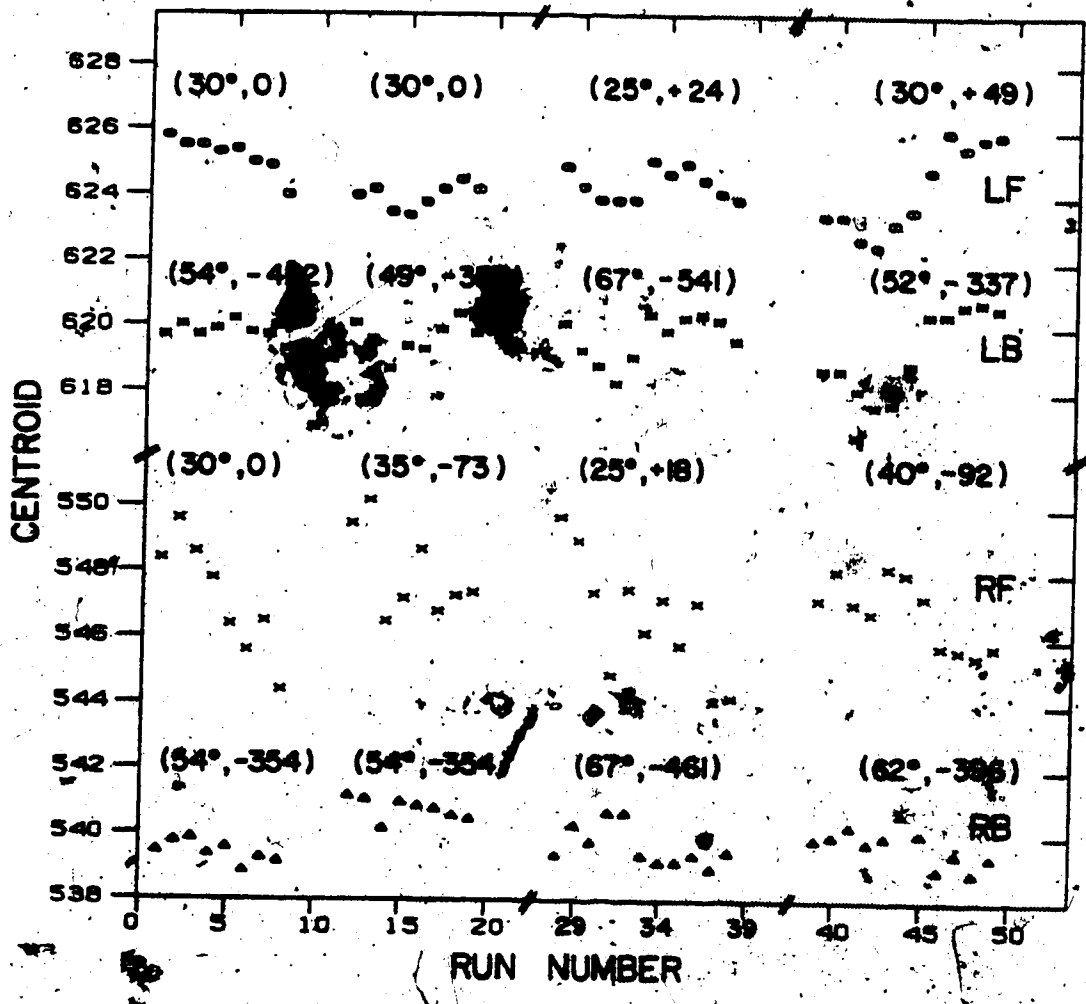
the energy at the NaI detector (T_{cal}), as determined from the pulse height, was assumed to be related to the pulse height of the proton (PH_p) and pedestal (PH_{ped}) in a linear fashion,

$$(IV.4) \quad T_{cal}(i) = g(i) \cdot [PH_p(i) - PH_{ped}(i)] ,$$

where $g(i)$ is the gain for the ith detector. The gains were obtained from the average pulse height for free p-p events, $\overline{PH}_p^{el}(i)$, and pedestals, $\overline{PH}_{ped}(i)$, from the $44°-44°$ (LF-RF, LB-RB) GH_2 runs:

$$(IV.5) \quad g(i) = \frac{T_{kin}(i)}{[\overline{PH}_p^{el}(i) - \overline{PH}_{ped}(i)]}$$

where $T_{kin}(i)$ is the energy at the ith NaI detector as determined from kinematics at the target (corresponding to the angle of scatter) and corrected for energy losses.

With this set of gains, a value of energy based upon the average free p-p pulse height and pedestal for each of the detectors for each angle pair of ^{40}Ca data containing free p-p scattering was computed using equation IV.4. The result of these calculations is presented in a plot of $(T_{kin}-T_{cal})$ versus T_{kin} shown in Figure IV-9. The departures from zero at high and low energies are a result of the nonlinearity of the system. A nonlinearity correction, of the necessary energy dependence, was introduced by adjusting the amount of material in front of

FIGURE IV-9

Kinematically determined energy at NaI minus the energy determined from the NaI free p-p pulse heights $(T_{kin} - T_{cal})$ for each of the 4 detectors as a function of T_{kin}. Pulse heights are from CH_2 as well as ^{40}Ca runs.

FIGURE IV-10

Same as in Figure IV-9 after nonlinearity correction has been applied.
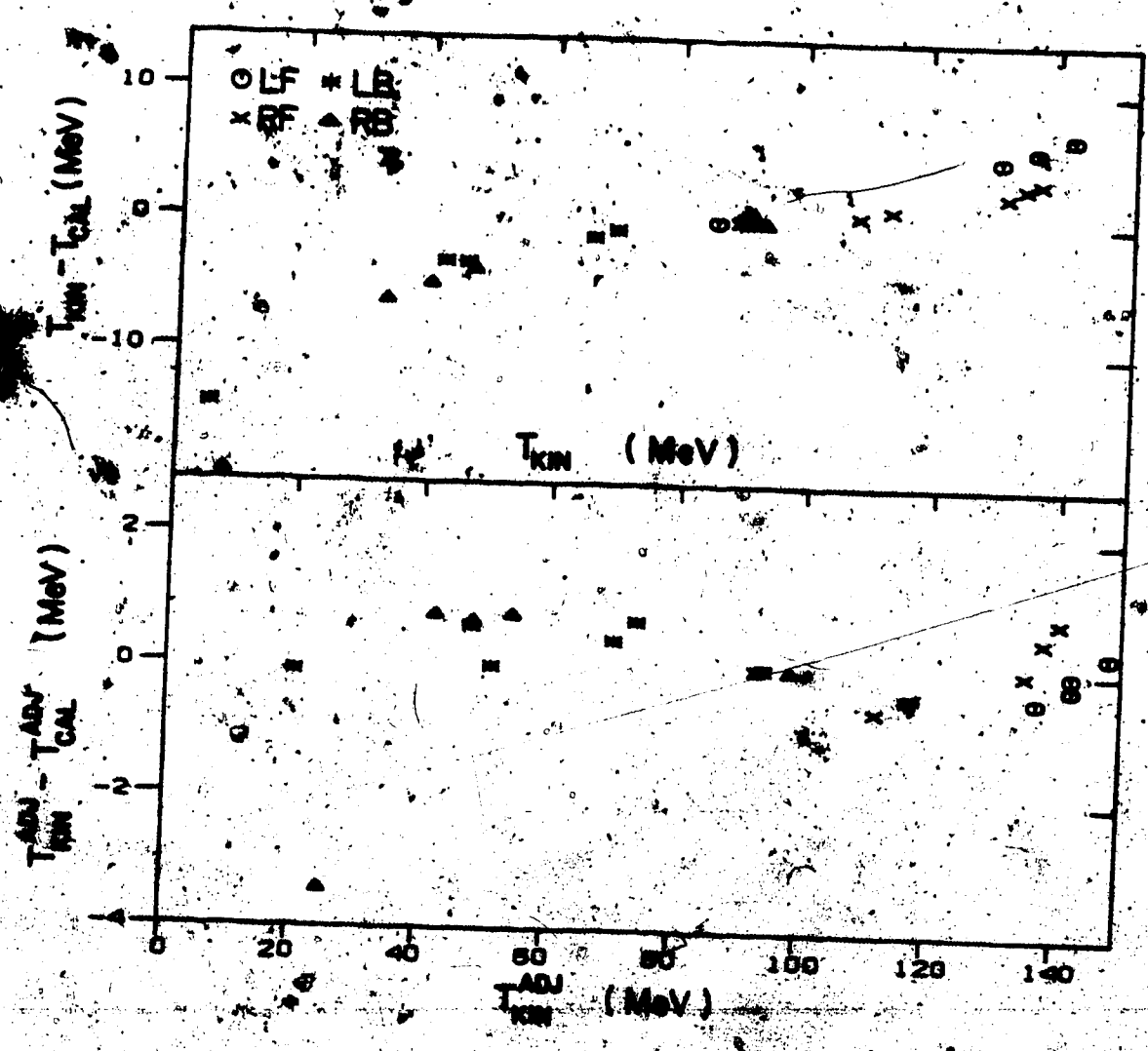
the NaI detectors used in the energy loss calculations. The adjusted values are given in Table VII.

With the same data, the gains were recalculated using equation IV.5 where T_{kin} was replaced by T_{kin}^{adj}. T_{kin}^{adj} is the energy at the NaI obtained from free p-p kinematics at the target and corrected for energy losses using the adjusted densities given in Table VII. The process used to obtain the points for Figure IV-9 was repeated and the new energy calibration gives the results shown in Figure IV-10. The non-linearities are now seen to be largely removed. Thereafter, energies at the target were obtained from NaI pulse heights and pedestals by means of equation IV.4 (using the adjusted gains) and by performing energy loss calculations with the values from Table VII.

With this procedure, the CD_2 target data were binned in ESUM versus EDIF histograms. The resulting positions in ESUM of the $^{12}C(p,2p)$ (BE=15.95 MeV) and $^2H(p,2p)$ (BE=2.225 MeV) loci typically ranged from 1 MeV above to 5 MeV below the expected position of the loci (based on kinematics and taking into account the recoil energies of the ^{11}B and neutron). The expected positions in ESUM of the loci for $^{12}C(p,2p)$ and $^2H(p,2p)$ ranged from ~182 to ~184 MeV and from ~190 to ~197 MeV respectively. For a given energy difference and angle pair, the difference between the position of the data and the expected position was the same for the $^{12}C(p,2p)$ and $^2H(p,2p)$ data. This, along with the fact that the size of the bins in EDIF (20 MeV) was large

compared with the error in ESUM, led us to regard any further adjustment of the energy calibration as unnecessary. The remaining discrepancy was regarded as a linear shift in ESUM which was treated in the fitting of the data.

A further refinement of the pulse height to energy conversion process involved the pedestal values. The pedestal for each detector was continually updated by the average of the last 100 pedestal values for that detector. This resulted in an improvement of 0.2 to 0.3 MeV in the ESUM resolution. The ESUM resolution varied with the angle pair and detector combination and ranged from 3.2 to 4.4 MeV. The variation with detector combination reflects individual detector differences. The variation with angle pair is possibly caused by time-varying temperature effects on the detector electronics.

4.8 Reaction Tail Subtraction

Reactions in the NaI(Tℓ) crystals produce tails from every point along a (p,2p) locus similar to those shown for free p-p scattering in Figure IV-11. To ensure that the ESUM resolution of the individual valence states was not being seriously degraded and that the heights of their peaks did not have a significant background due to the reaction tails of higher energy protons, an examination of the effect of reaction tail subtraction was performed. The shape of the reaction tails was taken from p-p spectra from the CH_2 runs and an attempt to strip away the tails

FIGURE IV-11

Scatter plot (logarithmic density scale) for T_{LB} versus T_{RB}. Counts are LB-RB (44°-44°) events with a CH_2 target. The free p-p peak and reaction tails as well as the $^{12}C(p,2p)$ locus are labelled.

$^{12}C(p,2p)$ LOCUS FREE p-p PEAK
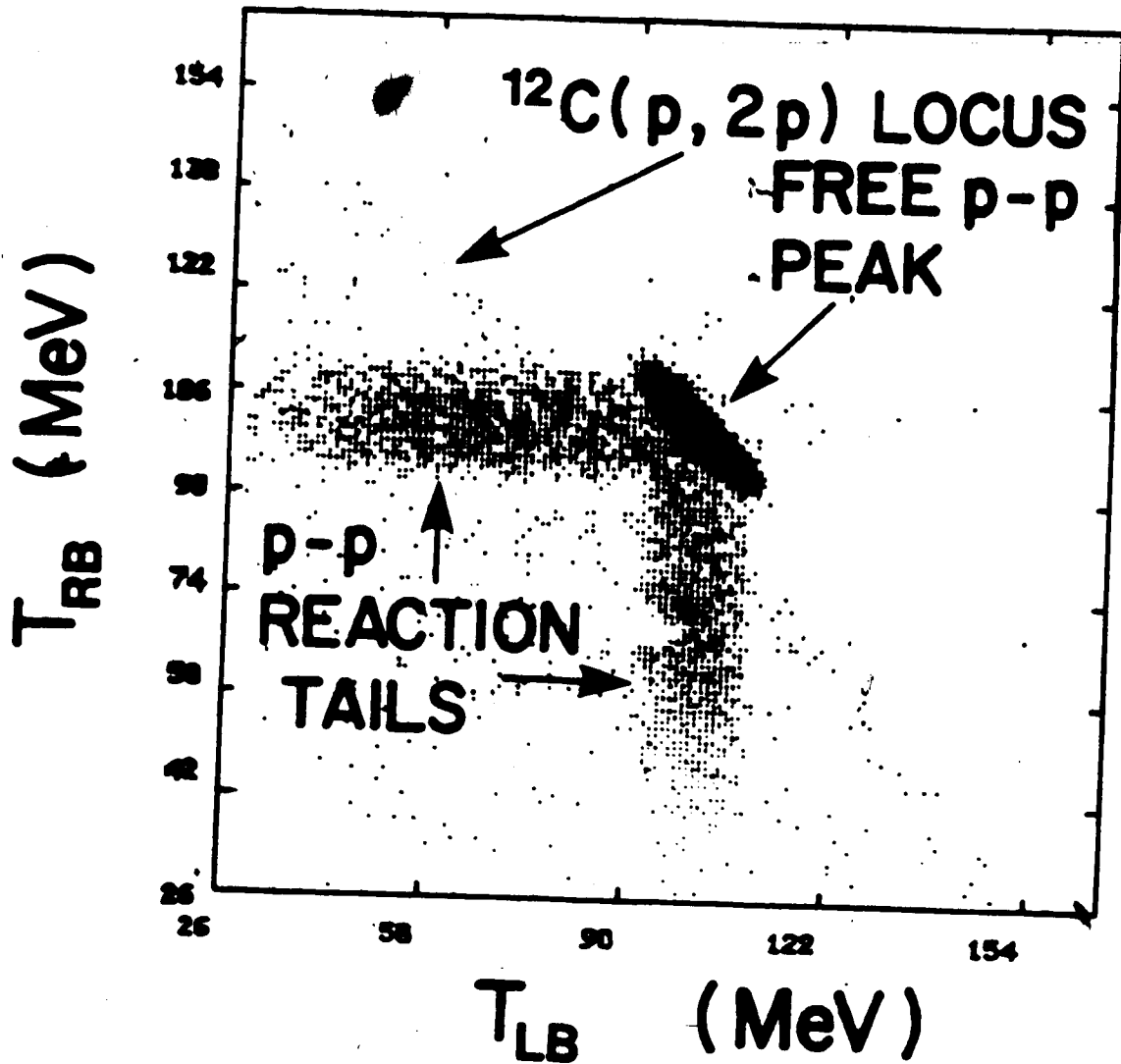
from the (p,2p) data was made. For a given angle pair and spin direction, (p,2p) events were binned in a KSUM versus KDIF histogram with bin sizes of 1 MeV by 1 MeV. For each bin of the histogram, the reaction tail contributions due to all higher energy protons were subtracted before proceeding to the lower energy bins. Once the subtraction process was completed, the remaining counts were rebinned in an KSUM versus KDIF histogram with bin sizes of 1 MeV by 20 MeV and compared with the uncorrected histogram. The reaction tail subtraction made no measurable improvement in the KSUM resolution, and an upper limit for the decrease in the counts for the $1d_{3/2}$, $2s_{1/2}$, and $1d_{5/2}$ region was <2%. Thus, the effect of tail subtraction was small and was not included in the final results.

4.9 Removal of Deuterons

Events from the (p,pd) reaction were acquired concurrently with the (p,2p) events. To eliminate them, a quantity proportional to the masses of the detected particles was calculated. The range, R, of a particle of energy T and mass M in a given material can be approximated by (SK-64)

$$(IV.6) \quad R\left(\frac{T}{M}\right) = K \cdot \left(\frac{T}{M}\right)^n \quad ,$$

where   K,n are constants, and n=1.8.
From an expression relating the difference in range (ΔR) for two particles differing in energy by an amount ΔT,

$$(IV.7) \quad \Delta R = R\left(\frac{T + \Delta T}{M}\right) - R\left(\frac{T}{M}\right) ,$$

and using equation IV.6, the following expression for the mass may be derived:

$$(IV.8) \quad M = \left[(T + \Delta T)^n - (T)^n\right]^{1/n} .$$

Here ΔT and T represent the energy deposited in the plastic detector and the emerging particle energy respectively. Thus, plastic scintillator pulse height had to be converted to energy for each of the detectors. Pedestals and free p-p scattering pulse heights for the plastic scintillators from CH_2 runs were used to establish a linear relationship between pulse height and energy. The energy of the particle emerging from the plastic scintillator was obtained from the energy deposited in the NaI detector plus the energy lost in travelling between the plastic and the stopping counter.

In order to resolve protons and deuterons on the basis of mass, it was necessary to correct the pulse heights in the plastic scintillators for an observed dependence on the vertical position of the particle in the detector. This dependence was studied by examining free p-p events from the CH_2 runs and the results are plotted in Figure IV-12 as a function of vertical distance (in wires) from the center for each of the plastics.

This behavior probably arises from a number of

FIGURE IV-12

Relative plastic pulse heights for each detector as a function of vertical distance from the center of the event-defining window. Data are from free p-p scattering from the CH_2 target. The position of the light guide and the center of the window are indicated.

Figure showing RELATIVE PULSE HEIGHT vs POSITION (WIRES), with curves labeled LIGHT GUIDE, CENTER, RB, LB, LF, RF.
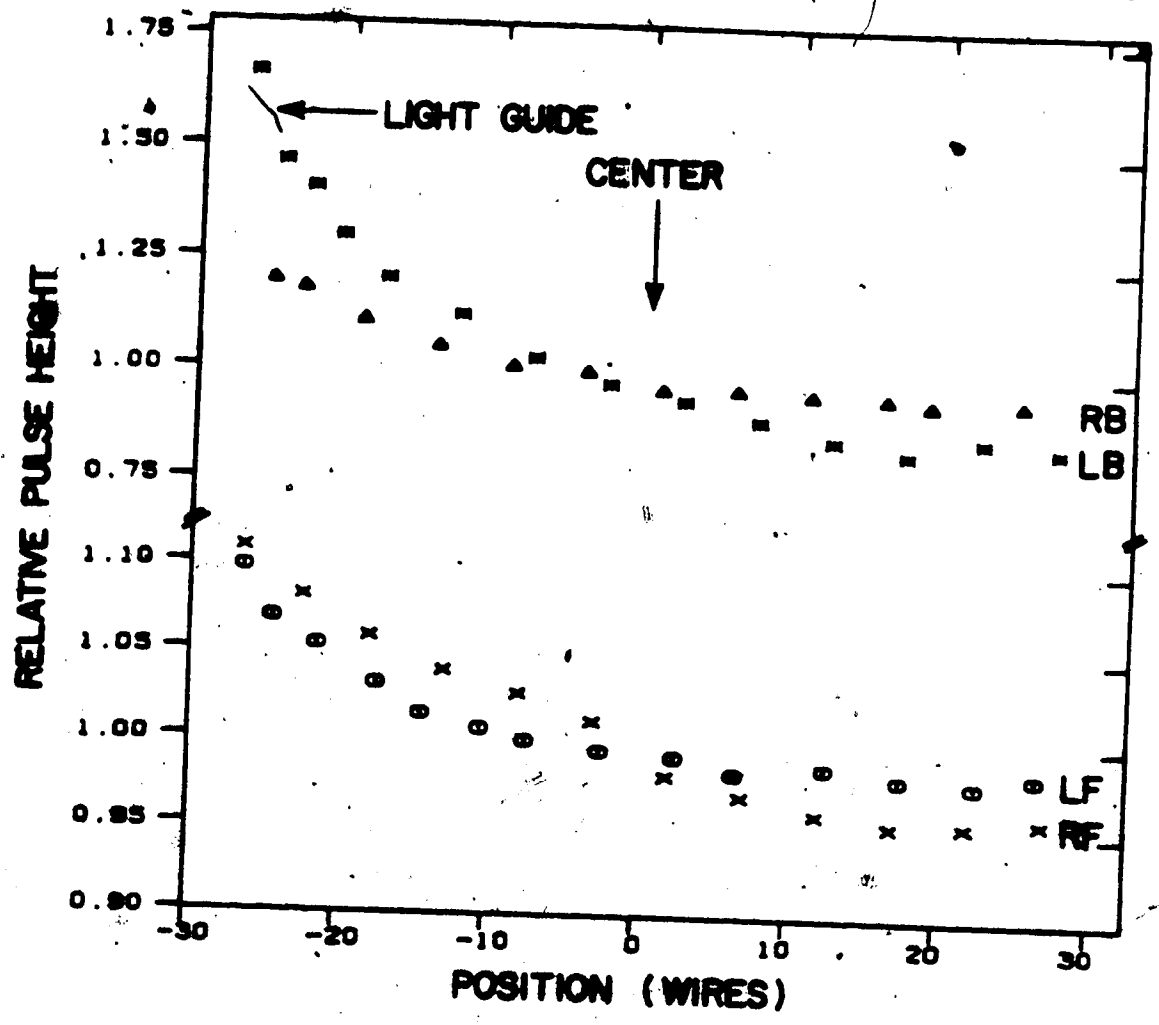
effects. The light undergoes attenuation in the
scintillator, and the solid angle acceptance of the light
guide decreases with increasing distance from the guide.
In addition, light signals undergo more reflections from
the boundary of the scintillator as they propagate toward
the light guide the higher they are generated in the
detector, and with each reflection there is some loss of
signal strength due to partial internal reflection. This
interpretation correctly predicts that the thick front
plastics should experience a smaller effect than the thin
back plastics (which should require more reflections).

After correction for this position dependence, the
protons were sufficiently well resolved to allow
elimination of the deuterons. Figure IV-13 shows the
distribution of events as a function of the mass parameter
for the RB detector for 30°-54° ^{40}Ca data. The deuteron
peak is to the right of the larger proton peak. Mass
parameter windows for protons were established for each
detector in a (p,2p) coincidence and events with either
particle mass outside these windows were rejected. This
eliminated varying fractions of events from ~9% (25°-67°)
to ~26% (67°-67°). Generally, the angle pairs for which
typical (p,pd) recoil momenta were smaller than typical
(p,2p) recoil momenta had the greatest number of events
containing deuterons.

FIGURE IV-13

Counts as a function of the mass parameter
for the RB detector. Counts are LF-RB (30°-
54°) events with a ^{40}Ca target. Proton and
deuteron peaks are labelled.
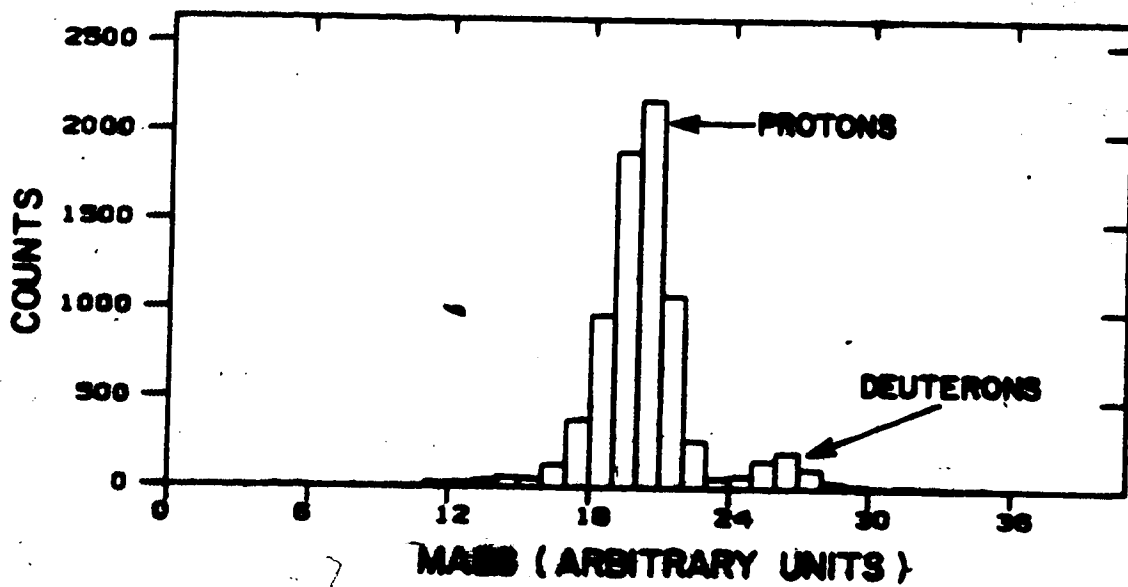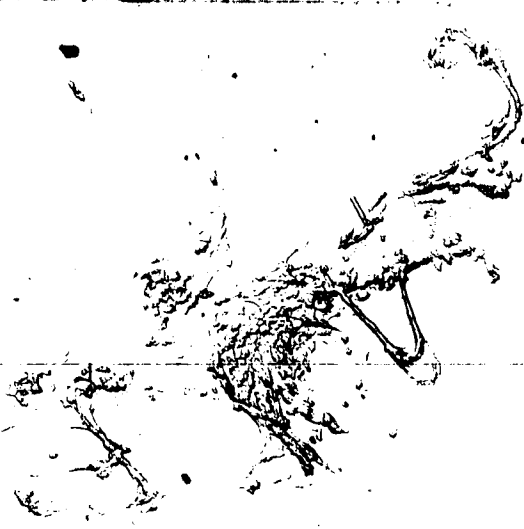
4.10 Decelerated Beam Events

The fraction of decelerated protons in the incident beam was large (~12%-78%) in 7 of the 39 ^{40}Ca runs. In the remaining 32 runs, the decelerated beam component was <2%. As mentioned previously, decelerated beam events could be resolved from normal beam events by means of the timing versus rf TDC information. Using the same procedure as in the NaI calibration to isolate free p-p events from ^{40}Ca data, the energy spectra for decelerated and accelerated beam events were studied separately. It was concluded that the incident energy of the decelerated component of the beam and the ESUM resolution were indistinguishable from those for the normal beam. Also, the beam polarizations were similar to those of other runs. For these reasons, decelerated beam events were not separated or treated differently from normal events in the subsequent analysis.

4.11 Dead Time Correction

The loss of events due to computer and electronic dead-time must be compensated for in the calculation of the cross sections. Two (correlated) measures of the dead-time, the first (a) including only computer dead-time, the second (b) including that from both sources, were calculated, from

$$(IV.9) \quad DTC_a = \frac{\text{Events presented to MASTER GATE}}{\text{Events written on tape}}$$

$$DTC_b = \frac{\text{Pulser events presented to system}}{\text{Pulser events written on tape}}$$

These measures were usually quite consistent; (a) was typically 0.6% to 1.0% larger than (b). Prescaling of polarimeter counts caused the interval between subsequent pulser triggers to be very regular. Thus, pulser events could cause dead time for non-pulser data but not subsequent pulser events. This, along with the fact that the electronic dead-time is expected to be negligible, explains the sense of the difference between the two dead times.

The value determined by method (a) was used. In instances when there was serious disagreement between the two methods, the problem was believed to be due to a hardware malfunction in the pulser electronics. In such cases, the ratio of non-pulser events written on tape to non-pulser events presented was taken as the dead time correction. Typically, this correction ranged from 1.05 to 1.12 for the ^{40}Ca runs.

4.11 Run Normalization

The number of incident protons during a run could be measured either by means of the polarimeter counts (NI_a) or ion chamber counts (NI_b) using equations II.2 or II.3 respectively. The free p-p scattering cross sections at ~43.2° from LF-RF and LB-RB CH_2 data with a polarization of ~0.73 (+) were computed. Using NI_a, the values obtained were consistent to within 0.2% and were ~10% lower than the values expected from phase shift calculations. When NI_b was used, for LF-RF and LB-RB the results were ~12% and ~

lower than the expected values.

Throughout the experiment, the ratio of NI_a to NI_b varied from 0.85 to 0.93 while this ratio dropped to values as low as 0.51 to 0.70 for a small number of runs. In the latter cases, the event rates presented to the acquisition system were much more stable as a function of NI_a than as a function of NI_b. The variation in the ion chamber gain was believed to be due to beam movement, changes in beam halo, small changes in the gas mixture, the window bulging under increased gas pressure or variable atmospheric pressure, and, probably most importantly, impurities (air) leaking into the chamber. Because of its superior stability, the polarimeter was used for beam normalization.

4.13 Target Components

Pure calcium is extremely reactive with many elements and compounds, including oxygen, making it notoriously difficult to protect from contamination. Between experiments, the ^{40}Ca target was kept immersed in a mineral oil bath (primarily consisting of CH_2) to protect it from air. After it was cleaned with acetone (CH_3COCH_3), the target was mounted in the target ladder and lowered into the scattering chamber which was then pumped to a rough vacuum (~ 90 millitorr = 12 Pascals).

The amount of hydrogen in the target at the time of the experiment, expressed as the ratio of hydrogen to calcium atoms, was $0.XXX\pm0.002$. This was determined by isolating the free p-p events from ^{40}Ca runs in the

previously outlined in section 4.7. Then, from known values for the free p-p cross section (from phase shifts), the amount of hydrogen could be deduced.

The source of hydrogen in the target was probably $Ca(OH)_2$ and residual mineral oil not removed in the cleaning. As previously mentioned, the free p-p peak is well separated from the $^{40}Ca(p,2p)$ data and the reaction tails were almost entirely removed by means of the elastic cuts. However, while the free p-p events posed no problem in the analysis of the $^{40}Ca(p,2p)$ data, other contaminants such as oxygen ($Ca(OH)_2$, CaO), nitrogen (CaN_2), and carbon ($CaCO_3$) have (p,2p) loci which overlap those from ^{40}Ca to varying degrees. Previously measured binding energies for single particle valence states for ^{40}Ca, ^{16}O, and ^{12}C are listed in Table VIII. Because of the 3.2 to 4.4 MeV summed energy resolution and the resulting overlap of single particle states from different nuclei, it is impossible to distinguish between the $^{40}Ca(p,2p)$ peaks and those of the contaminants. Consequently, other analysis methods were employed in an attempt to ascertain the amount of contamination. Since these analysis methods were performed after various periods of time had elapsed since the experiment (performed in June 1977), the resulting values serve only as upper limits. Due to a number of difficulties, the methods were not equally sensitive to the various contaminants and the following represents the best estimate for each of the contaminants.

TABLE VIII

Proton Binding Energies for ^{40}Ca, ^{16}O, ^{12}C
and Spectroscopic Factors for ^{40}Ca Valence States

Nucleus	State	Binding Energy (MeV)	Excitation Energy (MeV)[*]	Spectroscopic Factors[**]
^{40}Ca	$1d_{3/2}$	8.33	0	3.7
	$2s_{1/2}$	10.85	2.52	1.65
	$1d_{5/2}$	13.60	5.27	0.91
		13.94	5.61	0.64
		14.67	6.34	1.25
		14.83	6.50	0.10
		15.10	6.77	0.10
		15.29	6.96	0.18
		15.53	7.20	0.10
		15.76	7.43	0.47
		16.11	7.78	0.10
		16.50	8.17	0.35
		16.76	8.43	0.24
		16.88	8.55	0.22
		17.23	8.90	0.10
		17.43	9.10	0.10
		18.08	9.75	0.10
				4.96
^{16}O	$1p_{1/2}$	12.127	3.797	
	$1p_{3/2}$	18.44	10.11	
^{12}C	$1p_{1/2}$	15.95	7.62	

* Relative to $1d_{3/2}$ state of ^{40}Ca.
** Spectroscopic factors and binding energies for ^{40}Ca from (DO-76).

A value for the nitrogen to calcium ratio of 0.091±.004 was obtained (in August 1979) from a 200 MeV (p,d) experiment involving the ^{40}Ca target and a 90.2 mg/cm^2 kapton target ($C_{22}H_{10}N_2O_5$, density=1.42gm/cm^3) which served as a nitrogen target. The scattered deuterons were detected by the TRIUMF Medium Resolution Proton Spectrometer (MRS) at 22.0°. In the experiment, the peak for $^{14}N(p,d)$ in the deuteron energy spectrum was identified by means of the Q-value for the reaction (=-8.3 MeV). The Kapton target was used to determine the cross section for this process and this in turn was used to determine the amount of ^{14}N in the ^{40}Ca target. Unfortunately, the peaks corresponding to $^{12}C(p,d)$ and $^{16}O(p,d)$ were not resolved from $^{40}Ca(p,d)$ peaks and no reasonably accurate value for carbon or oxygen could be extracted.

A value for the carbon to calcium ratio of 0.054±0.009 was obtained (in August 1979) by means of gas chromatography. The method involved grinding a small piece of the target (~10 mg) into a powder which was then fed to a gas chromatograph. The sample was heated to a temperature of ~1100°C and the expelled gases were carried along by a jet of helium to molecular scrubbers which trapped H_2O, CO_2, He, N_2, or O_2. Even though $CaCO_3$ dissociates at ~900°C, CaO would probably remain as a solid (dissociation point >2850°C). Also the dissociation point for CaN_2 is >1192°C and thus this technique was inappropriate for determining the oxygen or nitrogen

contamination.

The amount of oxygen was measured by scattering 18 MeV protons from the ^{40}Ca target (University of Washington, Seattle, September 1979). Elastically and inelastically scattered protons were stopped at 110° in a solid state silicon detector. The ratio of ^{16}O to ^{40}Ca (RAT) was obtained from

$$(IV.10) \quad RAT = \frac{N_O}{N_{Ca}} \cdot \frac{\frac{d\sigma}{d\Omega}^{40Ca}}{\frac{d\sigma}{d\Omega}^{16O}} \quad,$$

where N_{Ca}, N_O were the number of counts in the ^{40}Ca and ^{16}O elastic peaks, and the elastic scattering cross sections, $\frac{d\sigma}{d\Omega}$, for ^{40}Ca and and ^{16}O were obtained from (SH-74,VA-71). The elastic peaks for ^{12}C and ^{14}N were not resolved in this experiment.

The ^{40}Ca target was briefly exposed to air in the process of mounting it in the scattering chamber despite attempts to isolate it by means of keeping it in a dry argon atmosphere. Thus, the value obtained for the ratio of ^{16}O to ^{40}Ca (0.526±0.055) represents a very pessimistic upper limit.

In summary, the level of contamination for ^{14}N and ^{12}C appears low enough to be unimportant. However, the situation for ^{16}O is less clear on the basis of these measurements. Fortunately, an indirect method of measuring the oxygen was found by means of incorporating previously

measured $^{16}O(p,2p)$ cross sections into the fitting of the $^{40}Ca(p,2p)$ data. This method is fully outlined in Chapter V and yielded a value of 0.324 ± 0.078. Furthermore, as detailed in that chapter, the final $^{40}Ca(p,2p)$ results were fully corrected for the presence of ^{16}O.

4.14 Event Analysis Summary and Cross Section Calculations

The cuts and windows applied to the events from each ^{40}Ca run in the order in which they were performed are summarized below.

i)   Pulser events were rejected.

ii)   The detector coincidence combination was determined. Subsequent analysis focussed on information from the two detector arms in coincidence.

iii)   Events not passing through the circular multiwire windows were rejected.

iv)   The elastic cuts were applied to those runs and angle pairs which contained free p-p events. This eliminated most free p-p events.

v)   The left-right timing (start-left, stop-right plastic) was examined and events were flagged either as a random (peak 1 or 3 of Figure III-6) or a prompt (peak 2). All subsequent cuts were applied in an identical fashion to both types of events.

vi)   Events for which pile-up occurred in either detector arm were rejected.

vii) Multiple hit events (events with spans >4 wires) were rejected.

viii) The energies deposited in the plastic and NaI detectors were computed. From these the mass parameter for each particle was calculated. If either particle fell outside the mass parameter window for protons, the event was rejected.

ix) The appropriate random or prompt energy histogram bin was incremented.

The bins of the energy histogram were: 100.5, 101.5, ..., 209.5 for ESUM (where bin 100.5 covers the region $[100,101)$ MeV etc.); -180, -160, ..., 200 for EDIF (where bin -180 covers the region $[-190,-170)$ MeV etc.). After the information from all runs having a given spin direction, detector combination, and angle pair were combined, the cross sections were calculated. As the incident beam was only ~70% polarized, the resulting spin ↑ and ↓ cross sections are referred to as partially polarized cross sections.

For a bin with energy coordinates ESUM=ES, EDIF=ED, the partially polarized cross section and error were computed as

$$(IV.11) \qquad \frac{d^4\sigma}{dESUM \cdot dEDIF \cdot d\Omega_1 \cdot d\Omega_2} = \left(\frac{NE-NRE}{2}\right) \cdot f \ ,$$

$$\frac{\Delta d^4\sigma}{dESUM \cdot dEDIF \cdot d\Omega_1 \cdot d\Omega_2} = \left(\frac{NE+NRE}{4}\right)^{1/2} \cdot f \ ,$$

where f is given by

$$(IV.12) \qquad f = \frac{DTC \cdot PUC \cdot MHC \cdot ELC}{\Delta ESUM \cdot \Delta EDIF \cdot d\Omega_1 \cdot d\Omega_2 \cdot N_1 \cdot N_t \cdot MWEFF \cdot NaIEFF} \ .$$

where   NE is the number of events in the prompt histogram bin,

NRE is the number of events in the corresponding randoms bin (includes 2 randoms peaks),

DTC is the computer dead time correction,

PUC is the pile-up correction,

MHC is multiple hit correction,

ELC is the correction factor accounting for the elimination of (p,2p) events in the course of eliminating free p-p events; it applies only to those detector combinations and angle pairs with free p-p events present,

ΔESUM (ΔEDIF) is the dimension of the bins in ESUM (EDIF), 1 (20) MeV,

$d\Omega_1, d\Omega_2$ are the solid angles subtended by the MWPC windows,

N_1 is the number of protons incident on the target (based on polarimeter counts),

N_t is the number of ^{40}Ca atoms per unit area in the target, $[7.44 \pm 0.37] \times 10^{20}$ cm^{-2},

NWEFF is the product of the efficiencies for the four multiwire planes for the detector coincidence being considered,

$$ = \text{NaIEFF}(T'_1) \cdot \text{NaIEFF}(T'_2) ,$$

where   NaIEFF(T) is the NaI efficiency at a proton energy T (from Table V),

T'_1, T'_2 are the energies of the protons at the NaI

detectors corresponding to energies T_1, T_2 at the target,

$ES=T_1+T_2$,

$ED=T_1-T_2$.

The expression for the error in the cross section contains only contributions from counting statistics and is derived according to equation AIII.1 in Appendix III. A summary of the errors in the factor f and its constituents is given in Table IX.

TABLE IX

Errors in f and its Constituents*

	Typical Statistical Uncertainties**	Systematic or Non-Statistical Uncertainties**
Δf	1.14% - 2.24%	15.55% - 17.23% #
Component of f		
DTC	0.2% - 0.6%	0.6% - 1.8%
PUC	0.6% - 0.8%	-
MHC	0.6% - 0.9%	-
ELC	0.61% - 0.65%	-
$d\Omega_1 \cdot d\Omega_2$	-	2.8%
N_1	0.06% - 0.07%	7%
N_t	-	5%
MWEFF	0.03% - 0.04%	-
NaIEFF	-	0.15% - 0.63%

*   f is defined in equation IV.12.

**   Ranges of values indicates that error varied with angle, energy, or run.

This total error is a worst case estimate obtained by adding the errors linearly.

CHAPTER V

FITTING OF THE DATA

The final stage of the analysis involved extracting unpolarized cross sections and analysing powers for the ^{40}Ca single particle valence states, $(1d_{3/2}, 2s_{1/2}, 1d_{5/2})$, as a function of EDIF from the partially polarized cross sections stored in the ESUM versus EDIF histograms. The functional dependence of analyping power and unpolarized cross section on the partially polarized spin ↑ and ↓ cross sections is given in equation AIII.10 of Appendix III.

The computer software used for fitting were a TRIUMF program (OPDATA) and a CERN program (MINUITS). Notes on some specialized aspects of the fitting and on the calculation of the errors from the results of the fits are included in Appendix III.

In a given 20 MeV EDIF interval, partially polarized cross sections for each of the valence states were obtained by fitting peaks to data over a portion of the ESUM range. Examples of ESUM spectra are shown in Figure V-1 where the spin ↑ and ↓ data for 30°-54° for 'channels' 100.5 to 200.5 in ESUM and EDIF = 20 MeV are presented. Since, as explained in Chapter IV, difficulties with the energy calibration resulted in small errors in summed energy which differed for each EDIF region, the amount of the shift from the correct value was determined in the fitting from the position of the $1d_{3/2}$ state. In Figure V-1, where the ESUM

FIGURE V-1

^{40}Ca(p,2p) cross sections as a function of ESUM (in channels) for LF-RB (30°-54°), EDIF=20⧸MeV. The positions of the ^{40}Ca valence states (ld$_{3/2}$, 2s$_{1/2}$, ld$_{5/2}$) are indicated along with those of possible ^{40}Ca lp states. The wide and narrow-fit windows are indicated by horizontal single and double headed arrows respectively.
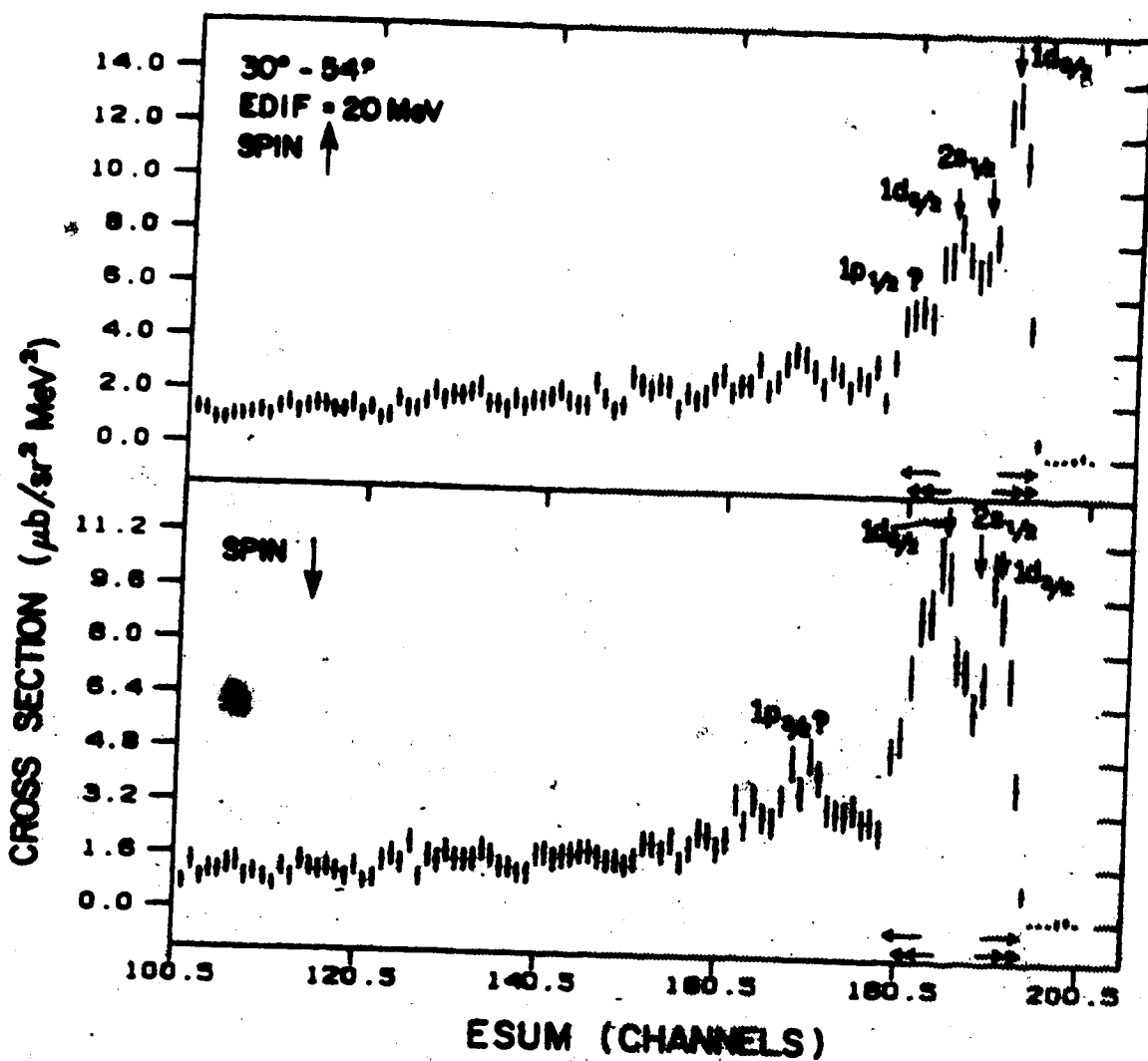
scale is uncorrected for the shift, the regions from channel 180.5 to 194.5 were the portions of these spectra fit in the final analysis. For this data, the final analysis determined the shift to be ~+0.3 MeV. Since the 3.2 to 4.4 MeV XSUM resolution due to detector resolution and other experimental effects is large compared with the expected width of a particle stable state of less than an eV, a Gaussian curve was taken to be an adequate representation of the peak shape.

Spectroscopic factors derived from the analysis of a $^{40}Ca(d,^{3}He)$ experiment (DO-76) suggest that most or all of the strength for each of the $1d_{3/2}$ and $2s_{1/2}$ single particle states is concentrated in a single peak while that for the $1d_{5/2}$ state is spread out over a number of peaks (over ~6 MeV in binding energy) as shown in Table VIII. The spectroscopic factors for the $1d_{3/2}$, $2s_{1/2}$, and $1d_{5/2}$ states (3.7, 1.65, 4.96) are ~93%, ~83%, and ~83% of their expected shell model values of $(2J+1)$ respectively. The peak positions and spectroscopic factors from (DO-76) for these 3 states are fairly consistent with results of an earlier $^{40}Ca(p,d)$ experiment (MA-72) as well as with the results of a $^{40}Ca(e,e'p)$ experiment (MO-76). Consequently, our model for fitting the data utilized a single Gaussian peak for each of the $1d_{3/2}$ and $2s_{1/2}$ states and a combination of 15 Gaussian peaks for the $1d_{5/2}$ state. For a given spin direction, there were three variable amplitudes, one for each of the valence states (where the

amplitude for the $1d_{5/2}$ was distributed on the basis of the spectroscopic factors in Table VIII). The relative positions of each of the peaks was fixed according to the excitation energies in Table VIII.

The shift in ESUM energy due to difficulties in the energy calibration was dealt with by allowing the positions of the peaks to shift up or down in ESUM with the spacing between the peaks remaining fixed. By varying the parameter for the position of the $1d_{5/2}$ peak, XI, the fitting routine could determine the best position of the peak for the fit. The difference between the best value of XI in the fit and channel 191.67 was the assumed energy shift over the entire ESUM region fit. Spin ↑ and ↓ data have identical energy calibration shifts and thus were fit together.

The height for a single peak at a particular channel in ESUM, XT, was found by evaluating a function of the form

(V.1) $\quad A \cdot \exp(-C52^2 \cdot (XT-XI+EXC)^2)$,

where   A is the amplitude,

XI is the position of the $1d_{3/2}$ peak,

EXC is the excitation energy (relative to the $1d_{3/2}$ peak) of the peak,

C52 is a peak width parameter related to the standard deviation of the peak position, σ, and the FWHM of the peak by

$$(V.2) \quad C52 = \frac{1}{\sqrt{2}\,\sigma} = \frac{2\sqrt{\ln 2}}{FWHM} \quad (FWHM \text{ in MeV}) .$$

The area under a Gaussian is given by

$$(V.3) \quad Area = \frac{A \cdot \sqrt{\pi}}{C52} .$$

To remove the contribution of the $^{16}O(p,2p)$ $1p_{1/2}$ and $1p_{3/2}$ states from the ^{40}Ca data, four peaks (two for each spin direction) were incorporated into the model as well. The values and statistical errors for the ^{16}O cross sections, $\sigma_0 \pm \Delta\sigma_0$, and analysing powers, $A_y \pm \Delta A_y$, were obtained from the results of a previous 200 MeV experiment (KI-80,KI-76). With the relations

$$(V.4) \quad \sigma_P(^{16}O) = \sigma_0 \cdot (1 + P \cdot A_y) ,$$

$$\Delta\sigma_P(^{16}O) = [(1 + P \cdot A_y)^2 \cdot \Delta\sigma_0^2 + (\sigma_0 \cdot P \cdot \Delta A_y)^2]^{1/2} ,$$

where P>0 for spin ↑, P<0 for spin ↓,

$\sigma_P(^{16}O)$, $\Delta\sigma_P(^{16}O)$ are the partially polarized cross sections and errors ($\mu b/sr^2 MeV$) for a polarization, P (where equation AIII.1 has been used),

the ^{16}O peaks were incorporated into the fit with amplitudes and errors given by

$$(V.5) \quad A(^{16}O) \pm \Delta A(^{16}O) = (\sigma_P \cdot \pm \Delta\sigma_P) \cdot g ,$$

and with the overall normalization adjusted to the ^{40}Ca data by the factor

$$(V.6) \quad g = \frac{C52 \cdot RAT}{\sqrt{\pi}} \quad ,$$

where   RAT is the ratio of ^{16}O to ^{40}Ca atoms in the target.

The angle pairs of data taken in this previous experiment did not completely overlap with all the angle pairs of the current experiment so that the fitting was performed only for energy differences between -100 and +100 MeV for the angle pairs 54°-54°, 47°-47°, 30°-30°, 30°-35°, 30°-40°, 47°-29°, 29°-47°, 54°-30°, 30°-54°, and 30°-62°. Results for three other sets of data where the $2s_{1/2}$ state was dominant (near conditions of zero recoil) were also obtained (67°-25° and 25°-67° (EDIF=120 MeV), 49°-35° and 52°-40° (EDIF=40 MeV)).

The amount of energy lost to recoil ($\sim$0.3 MeV at 150 MeV recoil for ^{40}Ca(p,2p) and $\sim$0.4 MeV at 100 MeV/c recoil for ^{16}O(p,2p) (where the ^{16}O 1p states have maximum cross section)) was small compared with the FWHM resolution of 3.2 to 4.4 MeV. Thus, the shifting of the positions of peaks in ESUM due to varying recoil energy losses as the angles or energy differences changed was ignored in the model, and recoil energy losses were neglected in the positioning of the peaks.

Even with the addition of these ^{16}O peaks, an 'extra'

peak (B, for background) was required in the model to account for an additional feature in the spectrum at an excitation energy of 12.4 MeV. Without the inclusion of this peak, the χ^2 increased substantially. The nature of the peak that appears throughout the data at this energy is unknown but one possibility is that it is $1p_{1/2}$ strength from $^{40}Ca(p,2p)$. This peak is part of the shoulder at approximately channels 178.5 to 181.5 in the spin ↑ spectrum of Figure V-1. A second interesting feature appears between channels 160.5 and 178.5 (centered at ~169.5) in the spin ↑ spectrum of Figure V-1. This may possibly be $1p_{3/2}$ strength from $^{40}Ca(p,2p)$. As this second feature is well outside the region of the data fitted, no account of it was taken in the model. Both of these features appear throughout the data in regions well away from $2s_{1/2}$ state dominance and were most prominent in the 30°-54° data which had the best statistics.

The fitting of the data proceeded in two passes. In the first pass, the model was developed. A linear least squares routine (OPDATA) was used to minimize a χ^2 function of the form given in equation AIII.2. In summary, the model consisted of 40 peaks with a common width parameter. For each spin direction, there were seventeen ^{40}Ca peaks, two ^{16}O peaks, and a background peak. Ten parameters in the model were always free: four peak amplitudes for each spin direction (three for ^{40}Ca, one for the background peak), the energy calibration parameter (XI), and the ^{16}O.

to ^{40}Ca ratio (RAT). The Fortran functions used to compute the value of the model for a particular spin direction are listed in Appendix IV where the ^{16}O peaks are in a separate function from the rest. The same functions were used for both spin ↑ and ↓ data.

More ^{40}Ca data (≳70%) were acquired at 30°-54° (LF-RB) than for other angle pairs. For this reason, much of the early development of the model was performed using this data. As the background peak was most prominent in the 30°-54° data, it was used to determine the B peak position relative to the $1d_{3/2}$ peak. The value obtained, 12.4±0.3 MeV, was thereafter adopted as a fixed parameter in the model.

As all the spin ↑ and ↓ data for a given angle pair and detector combination should have the same resolution, the width parameter was established by first fitting several of the ESUM spectra from that data set with the width parameter, C52, free. By statistically averaging the result for C52 from three or four spectra according to equation AIII.3, a value for C52 and its error was established and all subsequent fits for that data set were performed with C52 fixed. These values and errors were also used in the second pass of the fitting.

For a given spectrum, the range used in the fit was the same for the spin ↑ and ↓ data and was chosen so as to include as much of the region from the B peak (on the low ESUM side) to the $1d_{3/2}$ peak (on the high ESUM side) as

possible without including other background features. The number of channels in these fitting regions (which we call the wide-fit window) ranged from 16 to 19 while the number of degrees of freedom for a fit varied from 22 to 28. The wide-fit limits (inclusive) for $30°-54°$, EDIF=20 MeV are indicated by single-headed horizontal arrows in Figure V-1.

All data were fit using the model and the wide-fit windows described above. The values of RAT, except for those from the EDIF=±100 MeV spectra, where the statistics were generally quite poor, were used to determine the ^{16}O to ^{40}Ca ratio in the ^{40}Ca target. A histogram of these values of RAT is shown in Figure V-2. This distribution resembles a broad Gaussian peak. However, the statistics are too poor to make any definite conclusion. A simple average and the sample standard deviation were used as our conservative estimate for RAT and its error. This yielded a value for $^{16}O/^{40}Ca$ of 0.324±0.078 which was used in the second pass of the fitting.

In the second pass (performed using the CERN fitting program, MINUITS (JA-75)), the model was basically the same as for the first pass. In addition to the ten free parameters of the first pass, C52 and the four ^{16}O peak amplitudes were free parameters. However, RAT, C52, and the ^{16}O amplitudes were constrained from deviating significantly from their previously determined average values. For each of these six parameters, a constraint

FIGURE V-2

Distribution of RAT's, relative numbers of ^{16}O and ^{40}Ca atoms, produced from first pass fitting of data. The centroid of the distribution is indicated by an arrow.
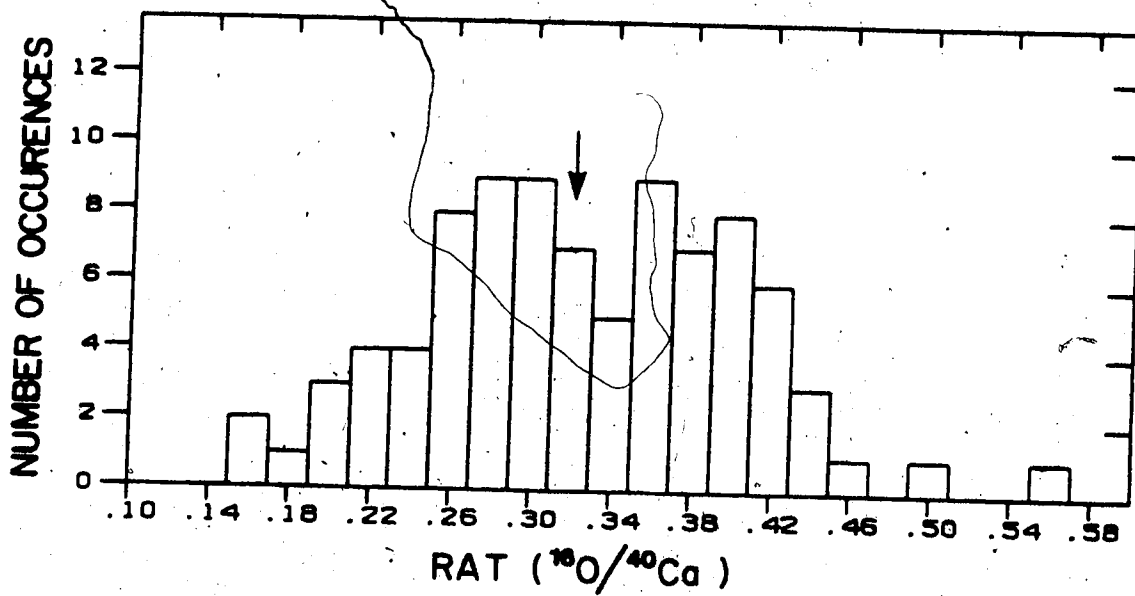
term of the form given in equation AIII.4 was added to the χ^2. In this manner, the uncertainties in these six parameters were reflected in final values for all the free parameters, their errors, and the χ^2.

The upper channel limit for each second pass fit was the same as that for the corresponding first pass fit. However, the lower limit was chosen to be the channel nearest to 11.5 channels below the position of the $1d_{3/2}$ peak (XI) as determined from the first pass. In this fashion, the second pass 'narrow-fit' windows were chosen in a consistent manner for all of the data. In addition, while the size of this window ensured the inclusion of almost all of the $1d_{5/2}$ state, it excluded a large fraction of the B peak region thus minimizing the dependence of the final results on the accuracy of the determination of the position of this peak. Varying the position of the B peak by amounts equal to its standard deviation (± 0.3 MeV) changed the results for the $1d_{5/2}$ and $2s_{1/2}$ states by $<2\%$ and had a negligible effect on the $1d_{3/2}$ state. Also, the values for XI from the second pass fits differed by <0.5 MeV from those of the first pass. The number of channels within these narrow-fit windows ranged from 14 to 17 and the number of degrees of freedom ranged from 19 to 25. The narrow-fit limits (inclusive) for $30°-54°$ EDIF=20 MeV are indicated by double headed horizontal arrows in Figure V-1.

The result of fitting the $30°-54°$ EDIF=20 MeV data is

shown in Figure V-3. The individual peaks are shown (solid lines for ^{40}Ca peaks, dashed lines with circles for ^{16}O peaks, dashed line with +'s for background peak) along with the overall fit (dashed line) and the individual data points along with their errors (*'s with bars). Fits which produced negative amplitudes were redone with a penalty function added onto the χ^2 as shown in equation AIII.5. Five spectra gave slightly negative amplitudes (<0.5 $\mu b/sr^2 Mev$) for the B or $2s_{1/2}$ peak and were re-fit.

From the ^{40}Ca amplitudes, C52 values, and their errors as determined from the fits, the partially polarized cross sections and errors were calculated according to equation AIII.6. These values, in turn, were used to derive the unpolarized cross sections, analysing powers, and their errors by means of equations AIII.10 and AIII.11. The results for $29°-47°$, $47°-29°$ (LF-RB, LB-RF), $30°-54°$, $54°-30°$, and $25°-67°$, $67°-25°$ were averaged statistically according to equation AIII.3. The final results for the ^{40}Ca unpolarized cross sections and analysing powers are presented and discussed in the next chapter.

A general overview of the quality of the fits is illustrated in Figures V-4 and V-5. These figures contain the distributions of the percentage points and the χ^2 per degree of freedom respectively for all of the second pass fits. A percentage point is the fractional probability of obtaining a value for χ^2 equal to or less than the value obtained in the fit; its interpretation is discussed in
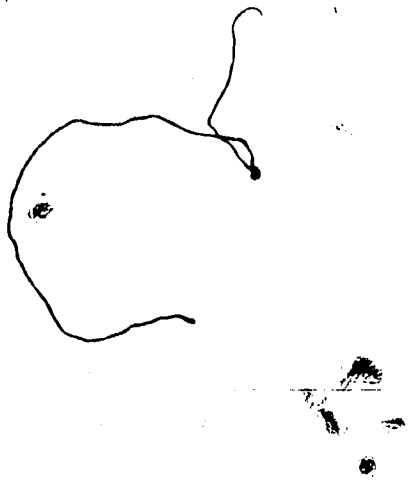
FIGURE V-3

Results of fitting LF-RB (30°-54°) EDIF=20 MeV data. Data points and their errors are indicated by asterisks and bars and the overall fit by a dashed line. The ^{40}Ca ($1d_{3/2}$, $2s_{1/2}$, $1d_{5/2}$) and ^{16}O ($1p_{1/2}$, $1p_{3/2}$) peaks are shown as solid lines and dashed lines with circles respectively while the background peak is denoted by dashed lines with pluses (+). The energy calibration shift has been applied to the ESUM scale.
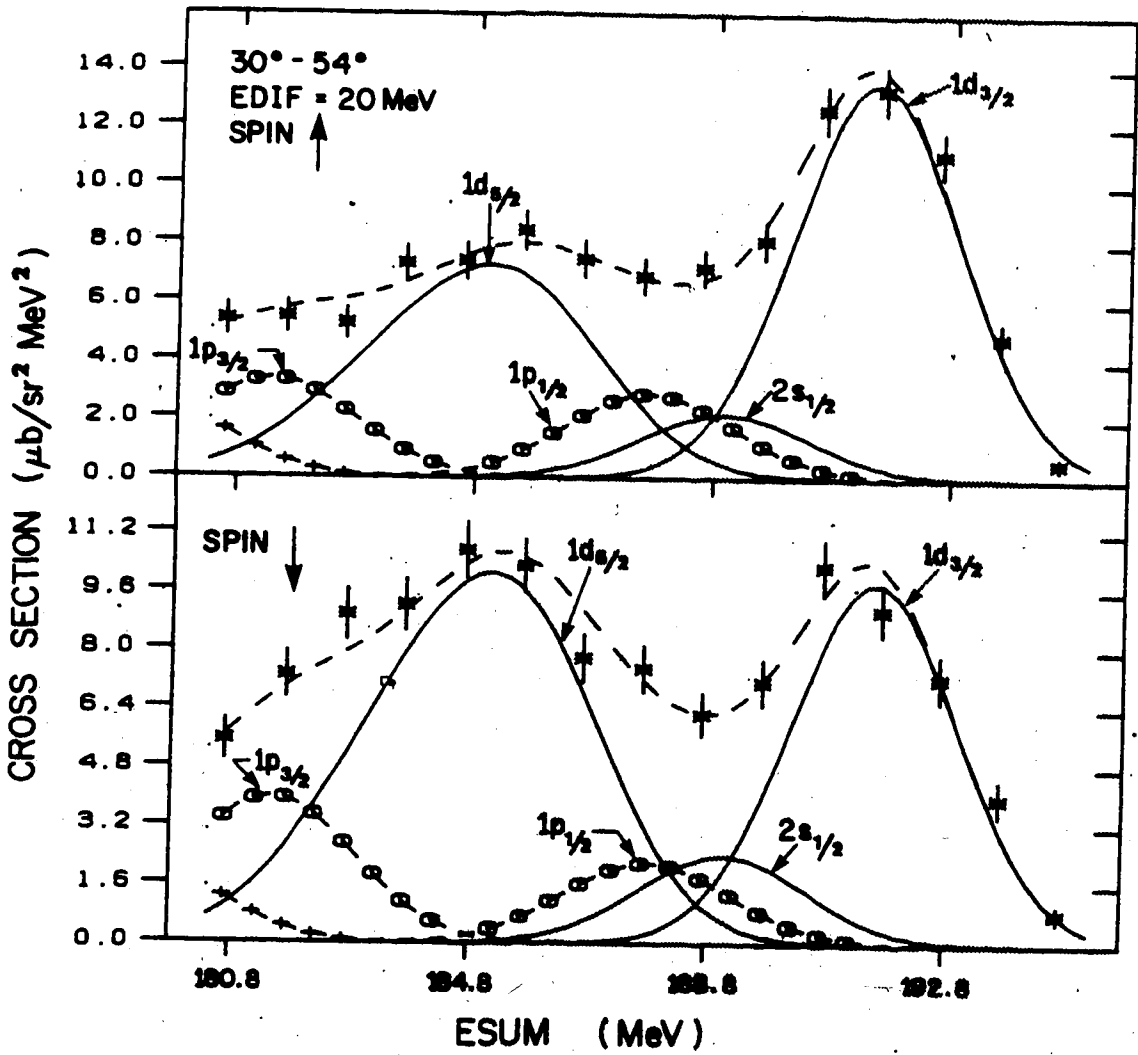
FIGURE V-4

     Distribution of percentage points from the
     second pass fitting of the data.

FIGURE V-5

     Distribution of χ^2 per degree of freedom
     from the second pass fitting of the data.
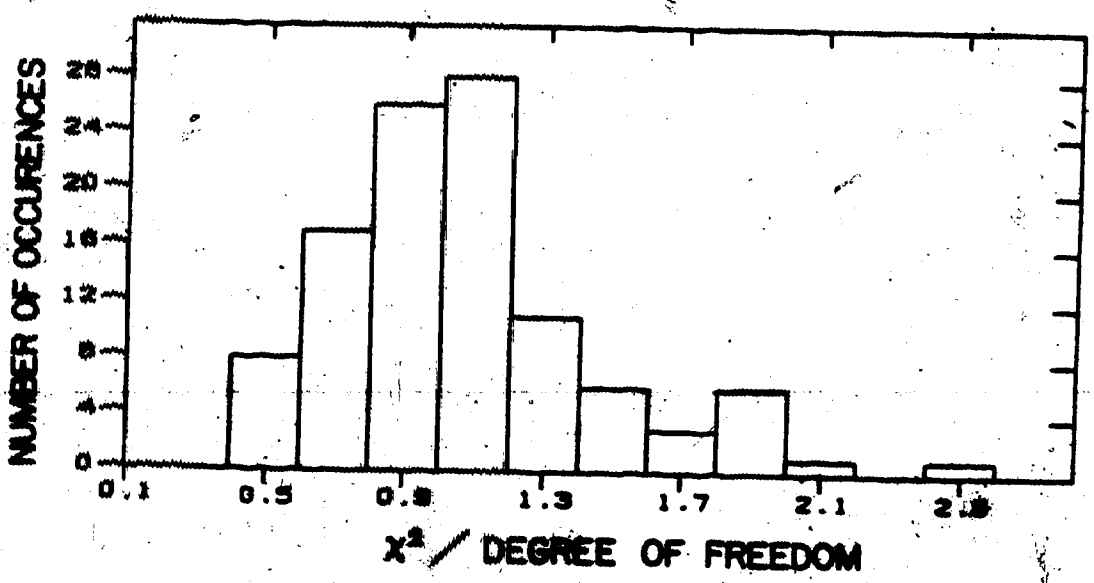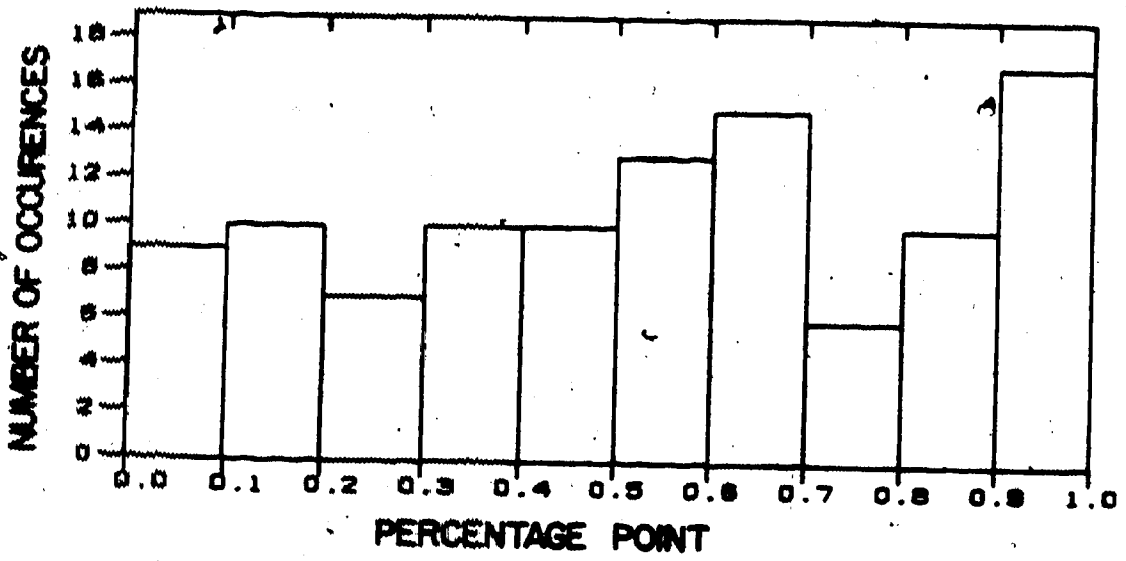
Appendix III.   The percentage points are fairly evenly distributed with a small amount of skew toward the high end.   The χ^2 per degree of freedom histogram exhibits a χ^2-like distribution with a peak at a value of ~1.2.   Neither distribution contains any disturbing features.

CHAPTER VI

COMPARISON OF RESULTS WITH DWIA CALCULATIONS

The values of the cross sections and analysing powers for the $1d_{3/2}$ (circles) and $1d_{5/2}$ (crosses) states obtained from the fitting are presented in Figure VI-1. For each angle pair, the data are plotted as a function of EDIF. In addition, the $2s_{1/2}$ cross sections and analysing powers are plotted as a function of THETA$_{pp}$ (the p-p scattering angle in the center of mass of the two protons) for conditions where the recoil momentum is at or near zero which includes: 25°-67°, EDIF=120 MeV (THETA$_{pp}$=52.1°); 30°-62°, EDIF=100 MeV (62.1°); 30°-54°, EDIF=80 MeV (66.5°); 35°-49°, EDIF=40 MeV (77.7°); and 40°-52°, EDIF=40 MeV (81.5°). Away from zero recoil momentum, the $2s_{1/2}$ strength was small compared with that of the $\ell=2$ states; consequently, its cross sections and analysing powers were poorly determined and are not shown.

The curves in Figure VI-1 are the results of DWIA calculations performed with the code THREEDEE (CH-79). This code performs the calculations according to equation AI.5 and employs a direct 3-dimensional numerical integration avoiding the use of angular momentum coupling coefficients. This represents a substantial improvement over previous codes which did not include the effects of spin-orbit distortion. The calculations were performed at the kinematic conditions for which the data were obtained

FIGURE VI-1

Cross sections and analysing powers for the $1d_{3/2}$, $1d_{5/2}$, and $2s_{1/2}$ states. Results for the $1d_{3/2}$ (circles) and $1d_{5/2}$ (crosses) are presented as a function of energy sharing (EDIF) for the angle pairs indicated while the $2s_{1/2}$ results are presented as a function of the free p-p center of mass scattering angle (as calculated using a half-off-shell prescription). The DWIA calculations for the $1d_{3/2}$, $1d_{5/2}$, and $2s_{1/2}$ states are given as solid, dashed, and solid lines respectively while the dashed line in the plot of $2s_{1/2}$ analysing powers corresponds to the free p-p analysing powers. The DWIA calculations were performed using spectroscopic factors one-half the simple shell model values of 2J+1.
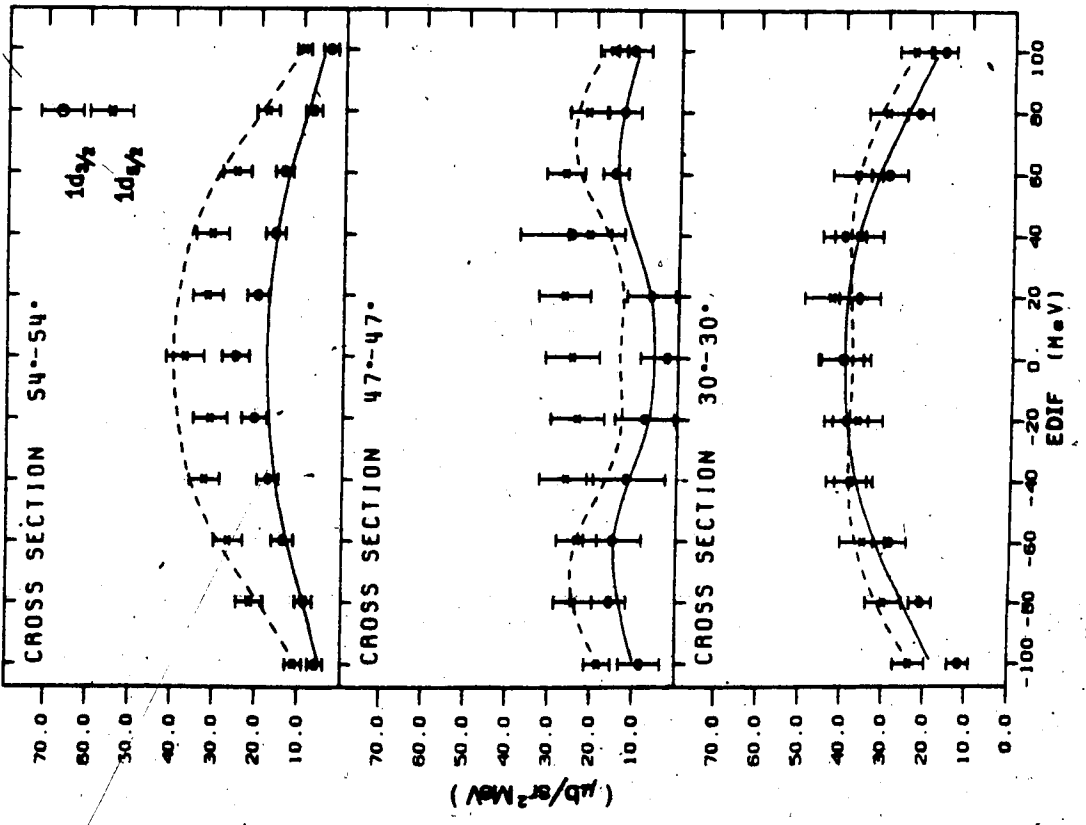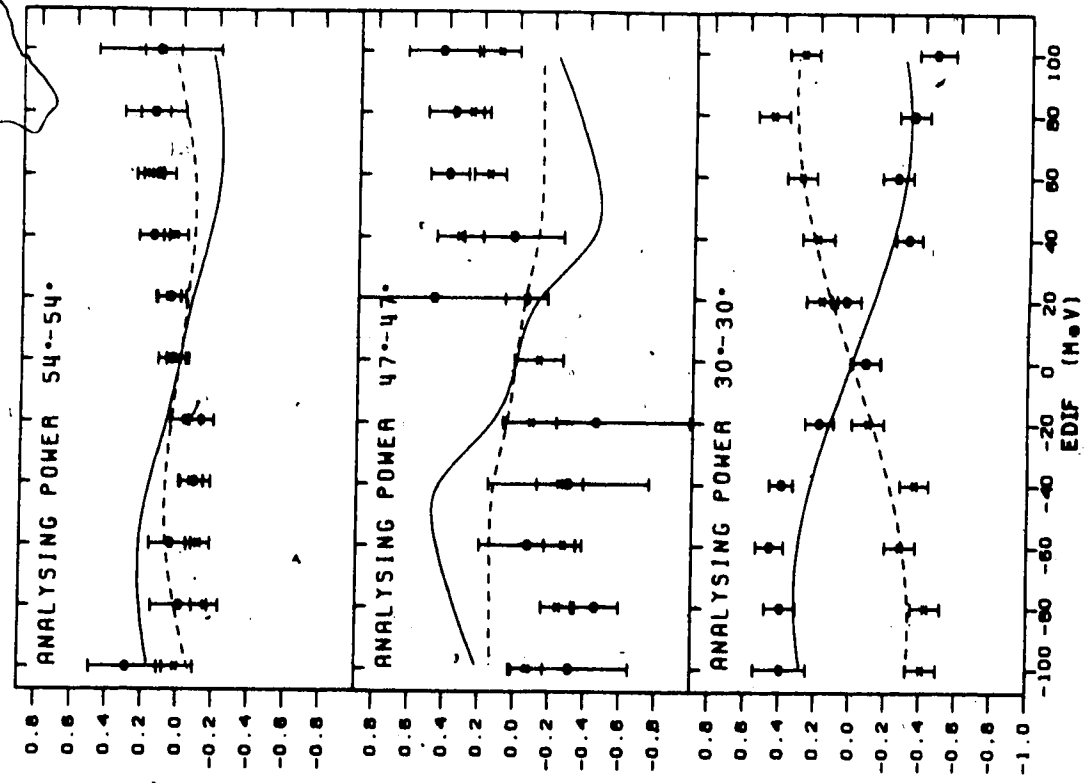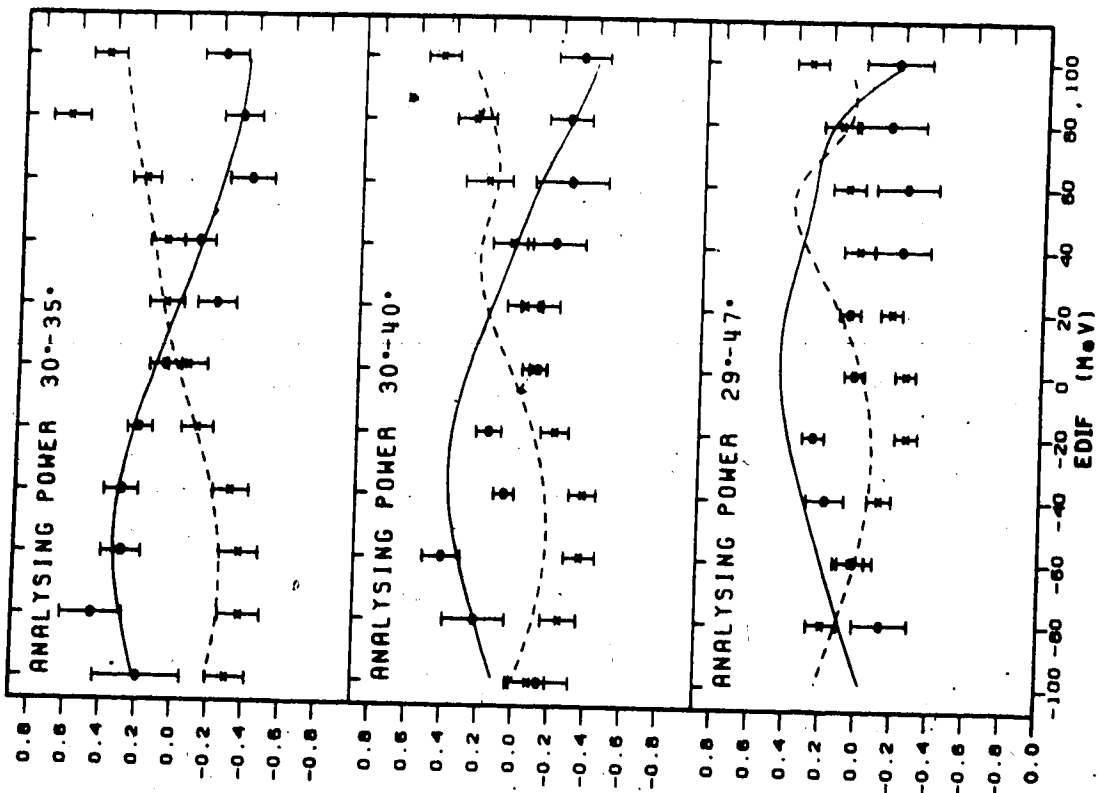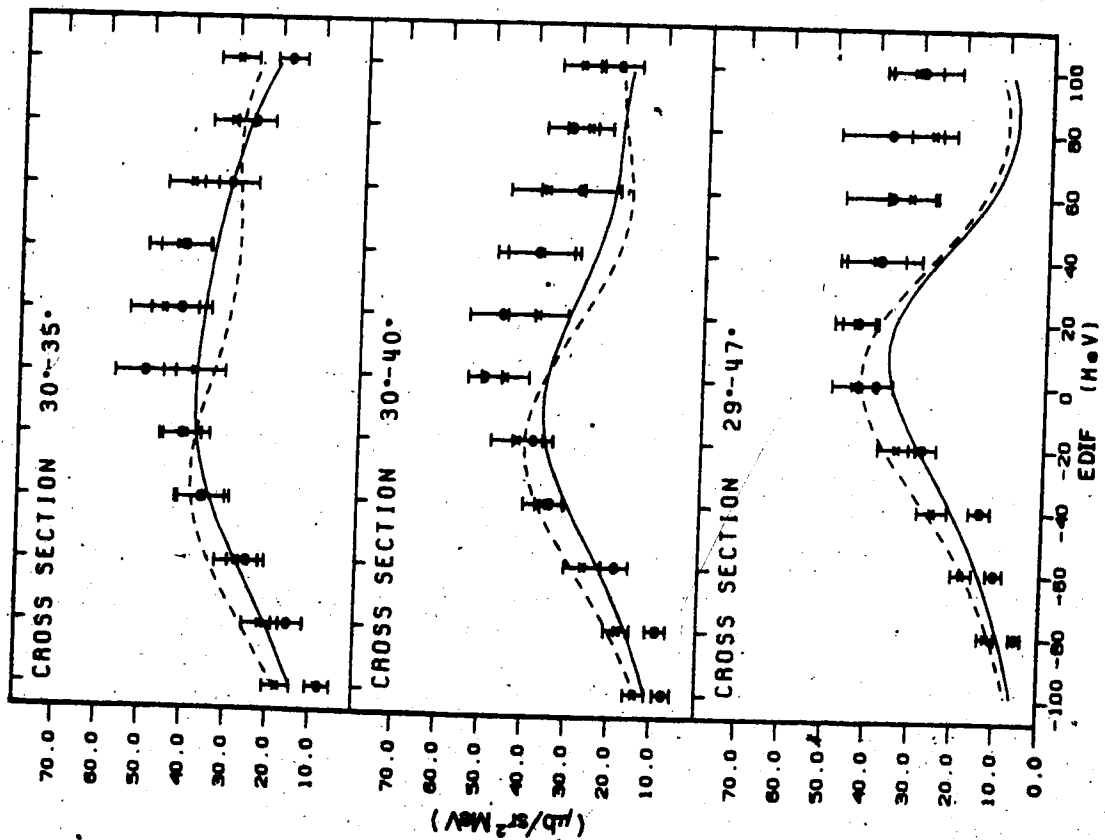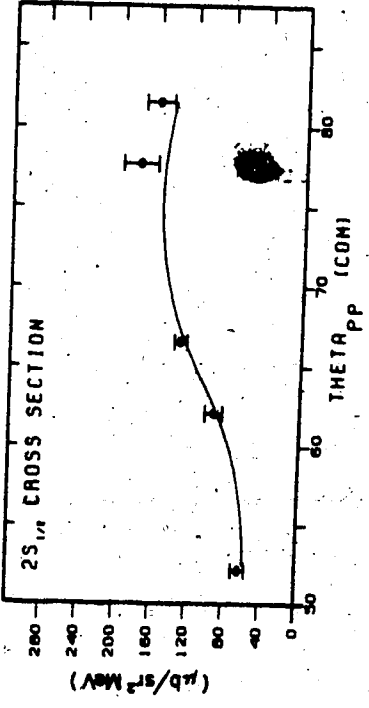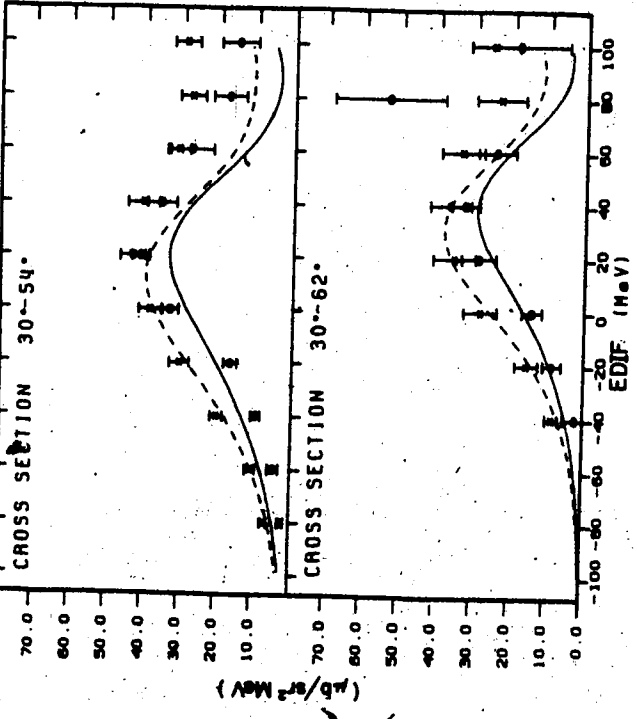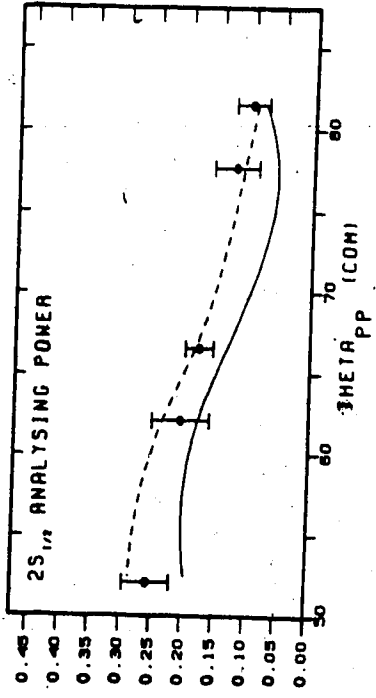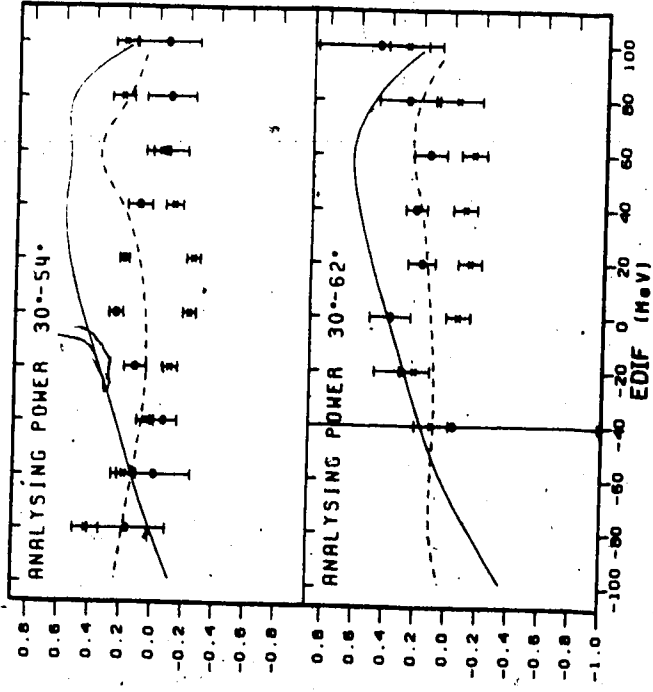
and the dashed and solid curves are interpolations between the calculated values. In the plots for the $1d_{3/2}$ and $1d_{5/2}$ states, solid and dashed curves are used respectively while solid curves are used in the plots for the $2s_{1/2}$ state. All calculations were done with an optical potential including spin-orbit terms. In addition, the dashed line in the plot of $2s_{1/2}$ analysing powers corresponds to the free p-p analysing powers resulting from excluding the spin-orbit terms in the optical potential. The cross sections are in units of $\mu b/sr^2 MeV$ and, in order to plot the DWIA values and the measurements on the same scale, spectroscopic factors one half the shell model values of $(2J+1)$ were used in the DWIA calculations.

In the calculations, the bound state wave functions were calculated from a Woods-Saxon potential with spin-orbit terms. The radius, diffuseness, and well depth parameters are taken from values derived from fits to elastic electron scattering data as well as the binding energy of the particular single particle state (EL-67). The binding energies used in the calculations for the $1d_{3/2}$ and $2s_{1/2}$ states are those given in Table VIII while a value for the $1d_{5/2}$ state of 15.07 MeV (based on an average of the binding energies of the various $1d_{5/2}$ components weighted by their spectroscopic factors) was used. As the calculations are not especially sensitive to small changes in the binding energy, this is an adequate approximation for the $1d_{5/2}$ binding energy. The optical potential

(SC-80) used was derived from a global fit to angular distributions of p-^{40}Ca elastic scattering cross sections and analysing powers including recent TRIUMF (200 MeV) and Indiana (80,135,160,181 MeV) data. This phenomenological optical potential utilized relativistic kinematics and a semi-relativistic Schrodinger-type equation. The potential does not contain an isospin-flip component which would result in a charge exchange contribution to the calculation. The functional form of this potential, its energy dependence, and the modifications necessary to implement it in the code are outlined in Appendix V. The difference between p-^{40}Ca total reaction cross sections (σ_r) predicted using this optical potential and measured values is <9% at energies <140 MeV. Although the difference increases slightly to 14.5% at 181 MeV, distortion plays a relatively less important role in this energy region for an incident energy of 200 MeV.

In the plane wave limit, the p-p interaction is half-off-shell. If an on-shell prescription is used, the half-off-shell nature of the interaction leaves some ambiguity as to the momentum at which to evaluate the p-p t-matrix. Two on-shell prescriptions are the initial and final state prescriptions. They correspond to evaluating the t-matrix at the momentum in the center of mass of the initial and struck protons (initial state) or in that of the two outgoing protons (final state). More recently, a half-off-shell prescription in which the t-matrix is evaluated

between the initial and final state momentum (to account for the momentum and energy mismatch) has been incorporated into the calculations in a manner detailed in (MI-79). The t-matrix is factorized into two parts: the on-shell t-matrix (in the form of partial wave amplitudes) which is evaluated from experimentally determined phase shifts (AR-77), and a real off-shell extension function calculated from the Mongan potential (MO-69) - a separable nonlocal phenomenological nucleon-nucleon potential. The results of calculations employing the initial and final state prescriptions differed slightly from those of the half-off-shell prescription by $<\pm 10\%$ in cross section and $<\pm 0.08$ in analysing power. All results shown correspond to the half-off-shell prescription.

The modification of the free p-p interaction in the presence of the nuclear medium is manifested, in part, through off-shell behavior. The effect of the distorting potentials taking the interaction fully off the energy shell has been investigated (using the Mongan potential) for $^{16}O(\vec{p},2p)$ (MI-80) according to a method outlined in (RE-73). Compared to the half-off-shell calculations, there were significant changes only for forward angles (30°-30°) where the analysing powers are reduced by <0.05 and cross sections increased by $<10\%$.

A second effect of the nuclear medium on the interaction is through Pauli blocking. Pauli blocking refers to the suppression of amplitudes for p-p scattering

that leave one of the protons with a momentum equal to that of one of the protons of the core. Calculations incorporating Pauli blocking performed by Miller and Thomas (MI-80) on $^{16}O(p,2p)$ indicate a change of ~0.05 in analysing power and an increase of <10% in cross section compared with the half-off-shell calculations. Because they do not appear to affect the results of the calculations strongly, neither Pauli blocking or fully-off-shell calculations were performed in the present analysis.

A careful comparison of the present DWIA calculations with the data reveals a number of trends. At equal proton angles and energies, the symmetry of the kinematics precludes the existence of a preferred direction. Consequently, the analysing power should and does vanish under such conditions in the data. Throughout the data, when the cross section calculations are normalized to the data, the resulting spectroscopic factors are ~50% to ~55% of the shell model values of $(2J+1)$. In contrast, studies of other reactions (DO-76,MA-72) have yielded spectroscopic factors lying in the range of the shell model values which is more consistent with naive expectations. For 47°-47°, as the EDIF is varied, the recoil momentum reaches a minimum of ~60 MeV/c and here one expects a dip in the $\ell=2$ strength while the $\ell=0$ strength peaks. This is confirmed by both the data and the calculations. The agreement between the data and calculations for the $\ell=2$ analysing powers is quite good for forward angles (30°-30°, 30°-35°,

30°-40°) but deteriorates steadily as one or both angles increases in the backward direction. For the $2s_{1/2}$ analysing powers the difference between the DWIA predictions and the free p-p analysing powers is small and the data do not favor either set of values. The results of the previous $^{16}O(\vec{p},2p)$ experiment at 200 MeV have been similarly compared with predictions from DWIA (KI-80). In this case the cross sections and analysing powers of the $1p_{1/2}$ and $1p_{3/2}$ states were calculated without spin-orbit distortion. The results were quite similar to the present case in that the cross sections were overestimated (by ~80%) and the agreement with the analysing powers was good for forward angles but poor as one or both angles increased.

For 30°-30° and 30°-54° ($\ell=2$) and the $2s_{1/2}$ cases, the calculations were redone with the real and imaginary spin-orbit terms in the optical potential set to zero. This caused an increase in the $p-^{40}Ca$ σ_r of <7% at the highest energy with no change at the lowest energy. The results are shown in Figure VI-2. There were small but non-negligible changes in the (p,2p) cross sections and small changes in the analysing powers which produced no general improvement in the agreement with the measured analysing powers.

The optical model potential describing the interactions when a proton passes through a nucleus can be calculated from the nucleon-nucleon (N-N) potential.

FIGURE VI-2

As in figure VI-1 .except that the spin-orbit term has been turned off in the DWIA calculations.
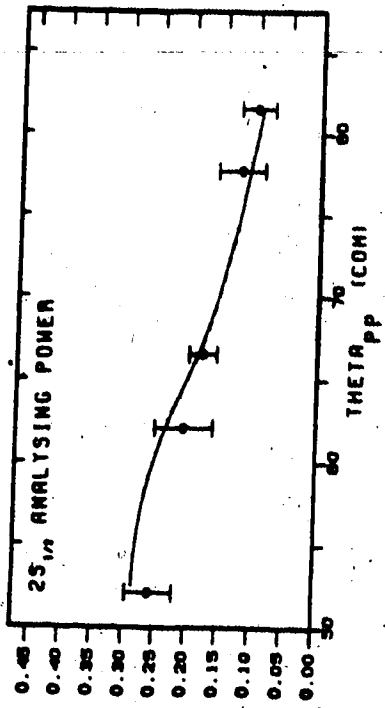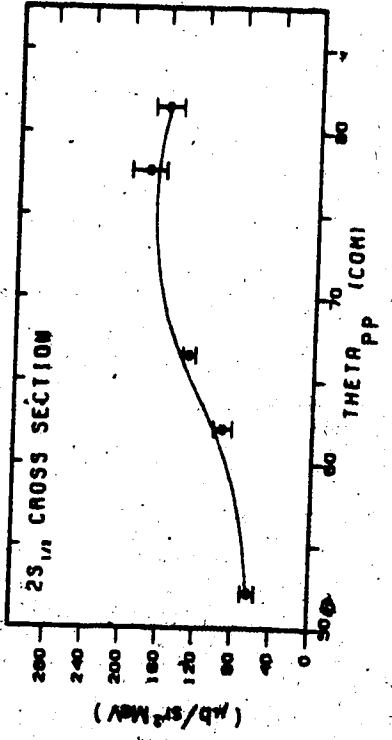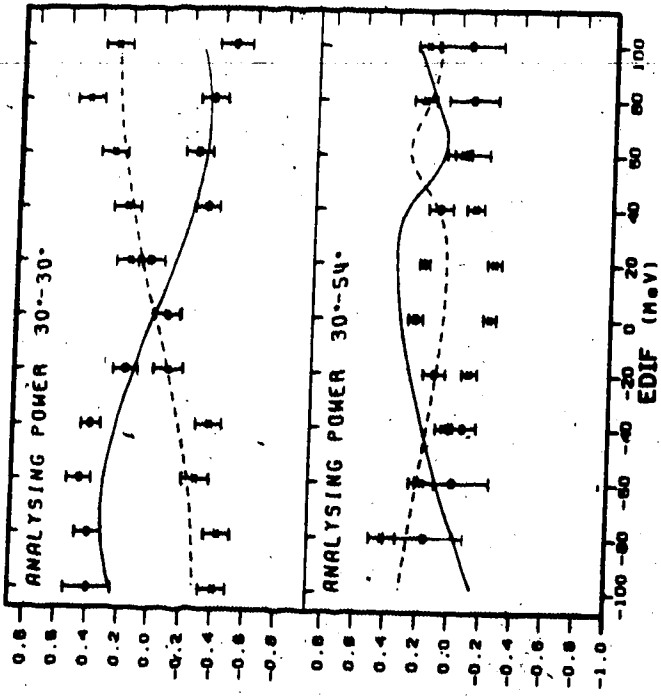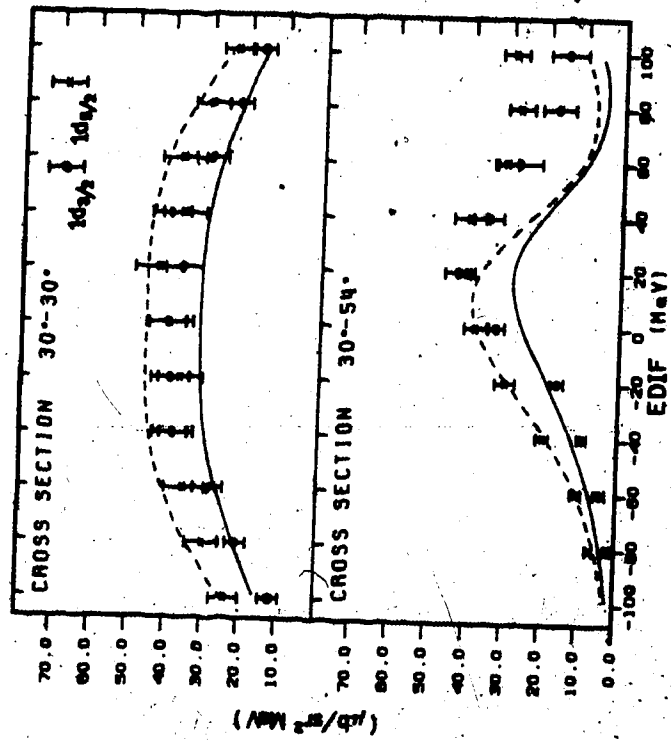
In this context, the intrinsic nonlocality of the N-N potential leads to a nonlocal optical potential. As well, nonlocality may be caused by antisymmetrization, as in the Hartree-Fock method of constructing self-consistent potentials for antisymmetric wave functions, or because the proton in the elastic channel moves under the influence of coupling to the other channels (AU-65).

Nonlocality is partly accounted for by means of an energy-dependent local optical potential, the calculated wave functions of which are asymptotically equivalent to those of its nonlocal counterpart. However, inside the nucleus, such local potential wave functions are not equivalent to the corresponding nonlocal potential wave functions. Calculations have shown that the amplitudes of wave functions derived from an attractive nonlocal potential are significantly reduced inside the nucleus compared with the corresponding amplitudes from a local potential which produces asymptotically equivalent wave functions. In the $^{16}O(\vec{p},2p)$ analysis, an investigation of this effect was performed by multiplying each of the distorted wave function amplitudes by a factor dependent upon the nuclear matter density, $[\frac{\bar{m}}{m}]^{1/2}$, where $\bar{m}$ is an effective mass characterizing the nonlocality of the potential. Values for this factor come from (JE-77) as does the radial dependence of the nuclear density. This nonlocality correction (method 1) was included in calculations for 30°-30°, 30°-54° (l=2) and the $2s_{1/2}$

values and the results are illustrated in Figure VI-3.

A second method (ii) of adjusting the distorted wave functions to correct for nonlocality has been investigated using the WKB method (HO-80,AU-65,PE-63,PE-62) and is incorporated in the present DWIA code. In this method, the degree to which the amplitude of the wave function changes as a result of having a nonlocal component (such as the real central part) in the optical model potential is parametrized by a range parameter, β. With β set to 1.0 fm and applying the correction corresponding to having a nonlocal real central potential to each of the distorted proton wave functions, calculations were performed for 30°-30°, 30°-54° and the $2s_{1/2}$ cases. The results are shown in Figure VI-4.

The two methods of incorporating nonlocality produce virtually indistinguishable analysing powers while the cross sections from method (i) are ~8% higher than those from method (ii). The nonlocal analysing powers differ by <0.03 from those of the local calculations. The nonlocal cross sections (method ii) are generally 20% to 50% lower than the corresponding local values. As β increases, the cross sections decrease and at a value of ~1.15 fm the spectroscopic factors for the $l=2$ states, as obtained by normalizing the calculations to the data, increase to ~(2J+1) in regions where the struck particle momentum is >55 MeV/c. In the $^{16}O(p,2p)$ analysis, method (i) produced effects similar to those observed here.

FIGURE VI-3

As in figure VI-1 except that a nonlocality
correction (method 1) has been incorporated
in the DWIA calculations.
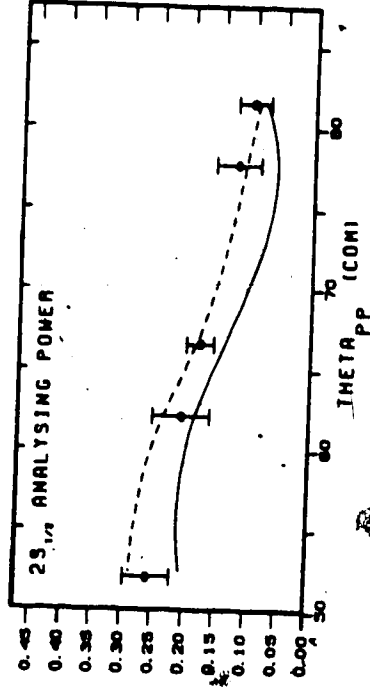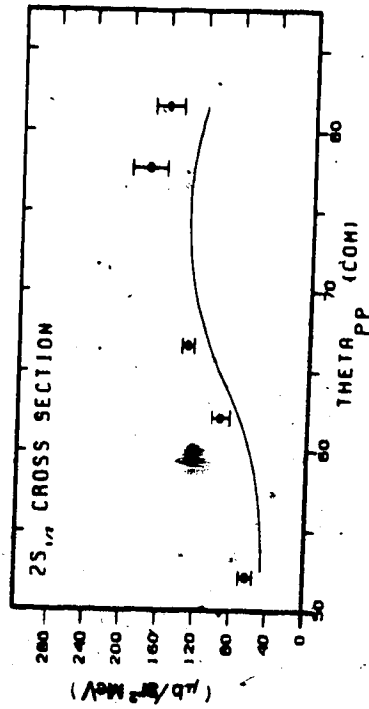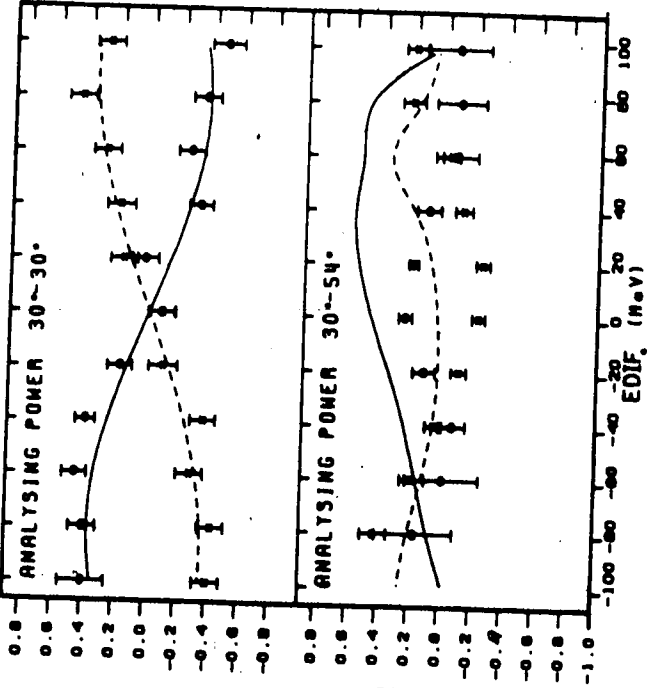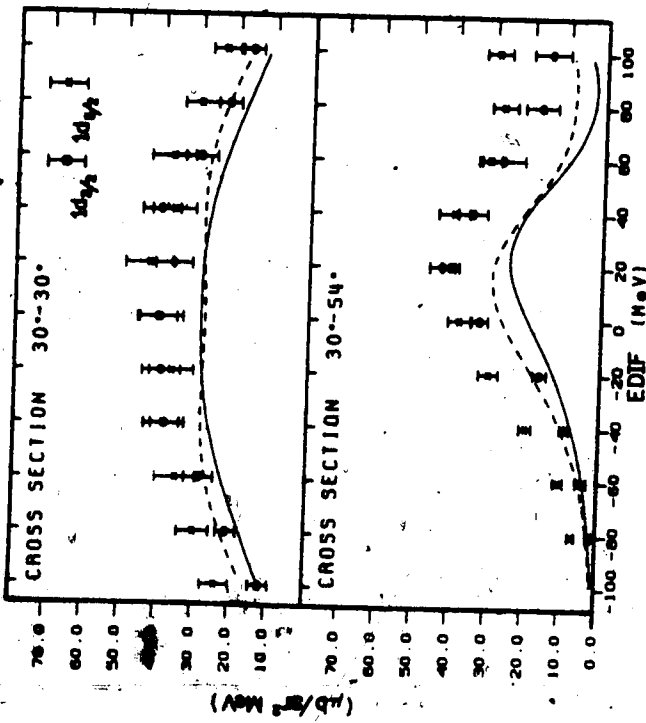
FIGURE VI-4

As in figure VI-1 except that a nonlocality
correction (method ii) has been incorporated
in the DWIA calculations.
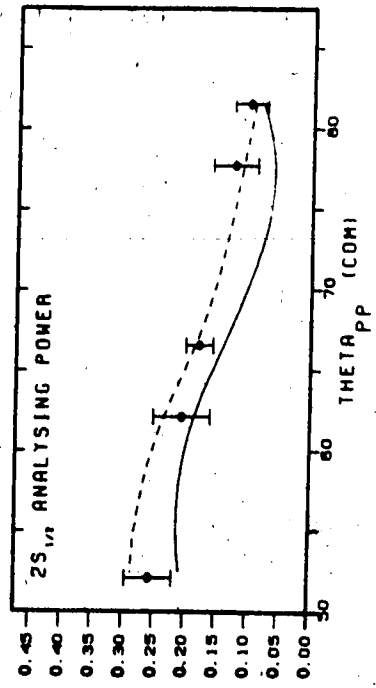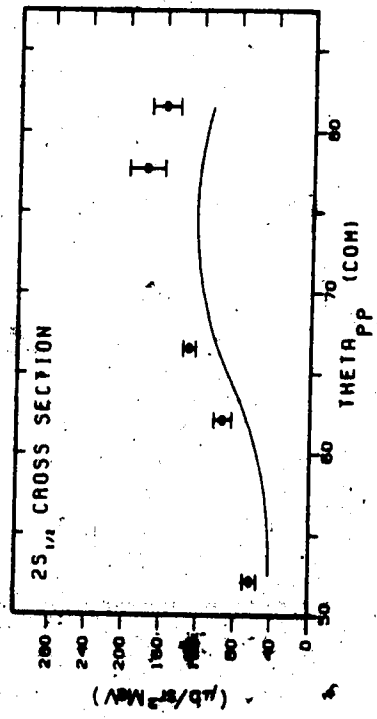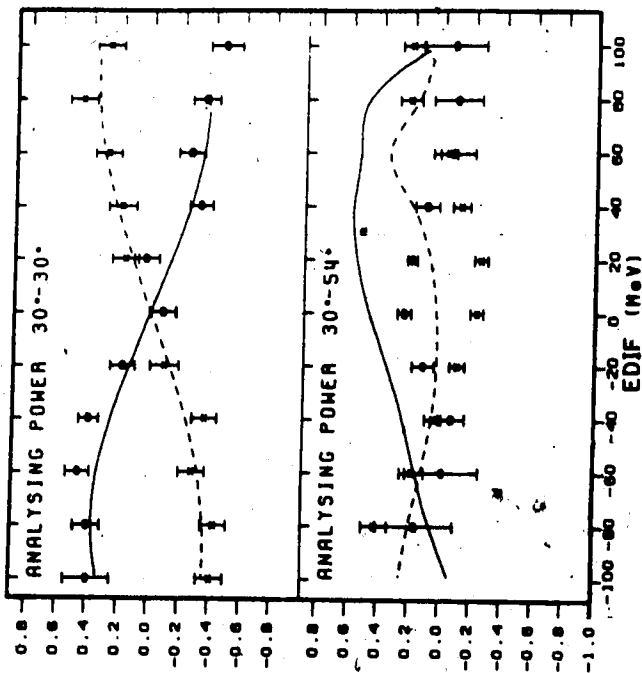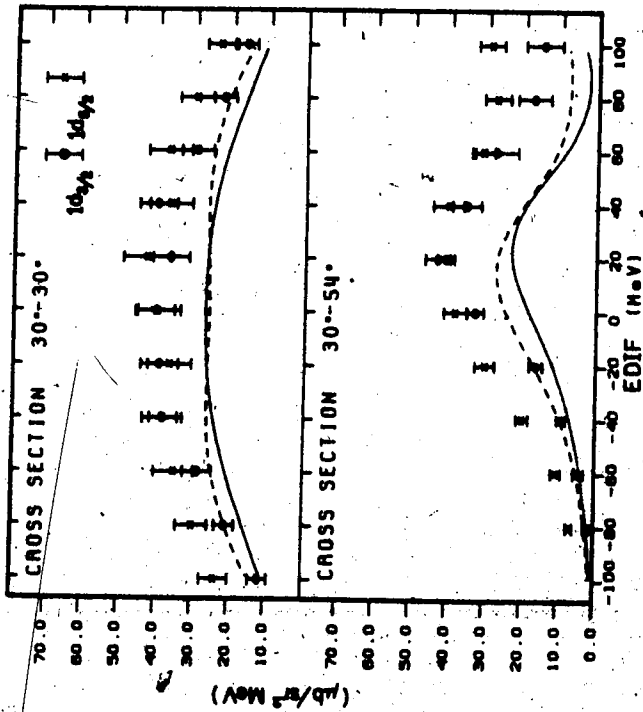
While the inclusion of nonlocality in the calculations improves agreement with the cross sections, the inability to reproduce analysing powers for $\ell \neq 0$ states in certain kinematic regions remains. In response to these concerns, Miller (MI-80) has recently pointed out that the directions of the protons at the interaction point can be altered by the refractive effects of the optical potential. Consequently, the use of the asymptotic center of mass angle between the emerging protons in the calculation of the free p-p observables may be inappropriate. This, along with reaction localization in the target nucleus, may lead to a shift in analysing power the magnitude and direction of which would be correlated with kinematics and which would be the same for states of the same ℓ ($\ell \neq 0$) but different j. Preliminary studies of these effects indicate shifts in the $1d_{3/2}$ and $1d_{5/2}$ analysing powers producing closer agreement with the data. The effect on the $2s_{1/2}$ state is thought to be negligible. Detailed calculations are planned.

For good shell model nuclei, if the spin-orbit term in the binding potential was zero so that the $j = \ell + 1/2$ and $j = \ell - 1/2$ states were degenerate, then the net polarization of the subshell would be zero and the following relation between the effective polarizations, P_{eff}, of protons of the same ℓ but different j would be expected to hold to a good approximation:

(VI.1) $\quad \ell \cdot P_{eff}(j = \ell - 1/2) = -(\ell + 1) \cdot P_{eff}(j = \ell + 1/2)$

The effective polarization is, in fact, insensitive to the
details of the bound state wave function. Consequently,
turning on the spin-orbit term in the binding potential
should not affect the validity of equation VI.1 (MA-79a).

In the absence of spin-orbit distortion; the effective
polarization for a state may be obtained simply from its
$(\vec{p}, 2p)$ analysing power by means of equation AI.4.
Using the free p-p analysing powers, A, and correlation
parameters, C_{NN}, obtained from phase shifts with a half-
off-shell prescription, the values of P_{eff} for the
$1d_{3/2}$ and $1d_{5/2}^{-}$ states were determined. The resulting
values of $2 \cdot P_{eff}(1d_{3/2})$ (circles) and $-3 \cdot P_{eff}(1d_{5/2})$
(crosses) are plotted as a function of energy sharing in
Figure VI-5. The results are consistent with equation
VI.1 when both angles are in the forward direction.
However, poorer agreement is observed as one or both angles
increase in the backward direction. A similar analysis of
the $^{16}O(\vec{p}, 2p)$ data (MA-79b) yielded comparable
results.

FIGURE VI-5

Plot of $\ell \cdot P_{eff}(1d_{3/2})$ (circles) and $-(\ell+1) \cdot P_{eff}(1d_{5/2})$ (crosses) as a function of EDIF for the angle pairs indicated.
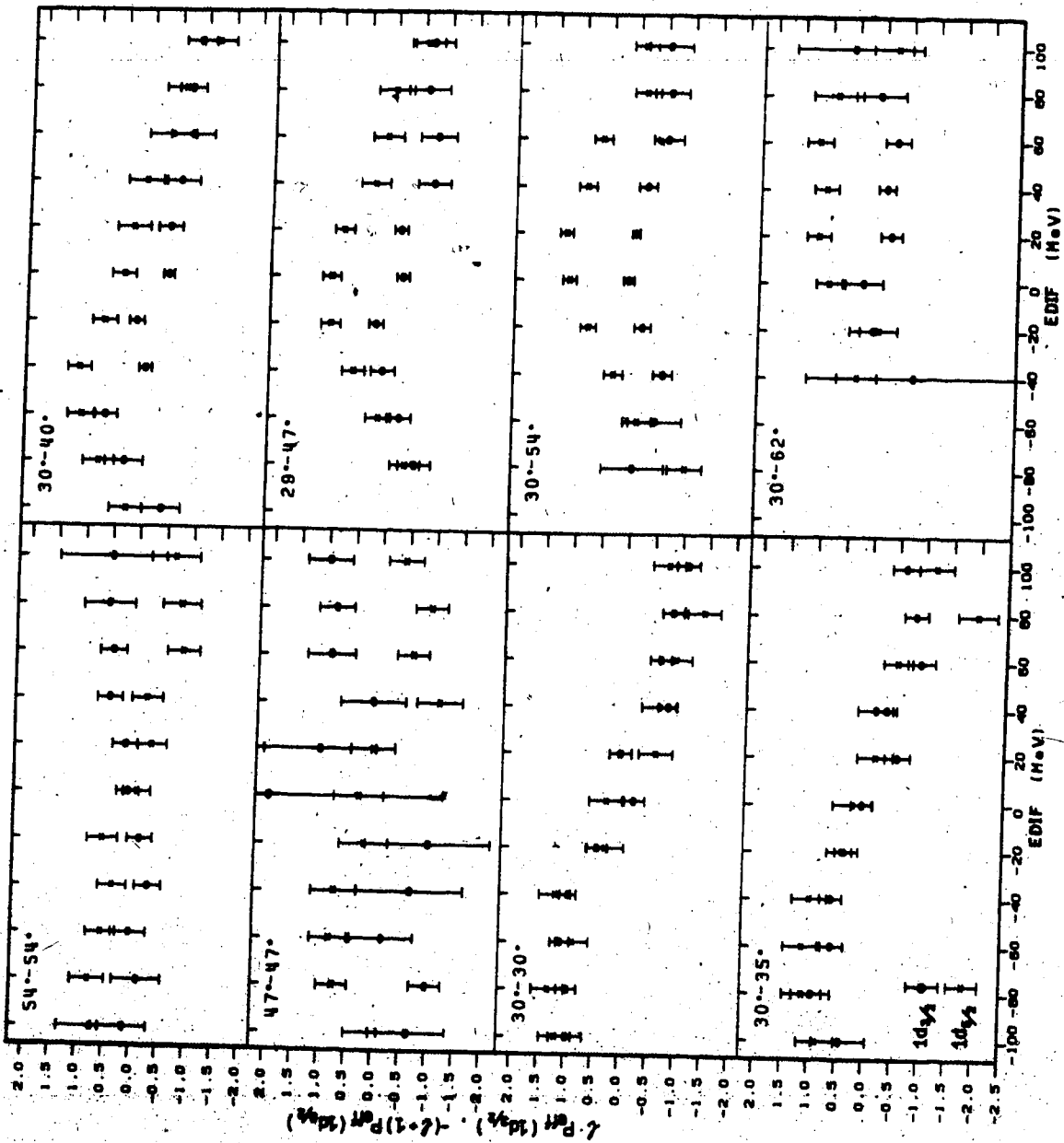
CHAPTER VII

CONCLUSIONS

This experiment has yielded extensive information on the behavior of the cross sections and analysing powers of the $1d_{3/2}$, $2s_{1/2}$, and $1d_{5/2}$ states of ^{40}Ca. The pattern of agreement between the DWIA calculations and the measured $\ell=2$ cross sections and analysing powers is remarkably similar to that observed in the earlier analysis of $\ell=1$ states from the $^{16}O(\vec{p},2p)$ experiment. The inclusion of nonlocality in the DWIA calculations reduces the cross sections, allowing the spectroscopic factors to increase toward values expected of these nuclei.

Although the inclusion of spin-orbit distortion in the present analysis has a marked effect upon the DWIA calculations, it does not significantly affect the quality of the agreement with the data. For the $2s_{1/2}$ state, the data are consistent with either the inclusion or exclusion of spin-orbit dependence in the optical model potential.

Evidence for the existence of ^{40}Ca $1p_{1/2}$ and $1p_{3/2}$ strength at ~21 MeV and ~30 MeV separation energy appears throughout the data although the energy resolution and statistical accuracy of our measurements in these regions is too poor to reach any definite conclusions.

DWIA has proven capable of successfully predicting analysing powers for medium and light weight nuclei like ^{40}Ca and ^{16}O in restricted angular regions. The strong j-

dependence of the analysing power has been clearly demonstrated in these measurements. Given the current state of agreement between DWIA and experiment, $(\vec{p},2p)$ reactions can be used as a spectroscopic tool to identify new pairs of states of the same ℓ but different j provided one limits oneself to appropriate kinematic regions. The results of this experiment thus serve as an incentive for future efforts in both the theoretical and experimental investigation of quasi-elastic scattering with protons.

A new measurement of $^{40}Ca(\vec{p},2p)$ would help to resolve a number of the questions left outstanding in this experiment. With better energy resolution (~1 MeV), a quantitative investigation could be performed upon the feature which may be a ^{40}Ca $1p_{1/2}$ state. Better statistics should enhance the broad feature which may possibly be ^{40}Ca $1p_{3/2}$ strength. The analysing powers of these two features could then be compared with DWIA calculations to determine if they exhibit behavior consistent with $1p_{1/2}$ and $1p_{3/2}$ states. This identification would be facilitated by taking measurements at forward angles, for example 30°-30°, where DWIA has demonstrated its ability to reproduce the data.

The current experiment has stimulated the beginning of an examination of the effect of reaction localization coupled with refraction of the distorted waves in the nucleus on the calculations. Such investigations may extend the reliability of DWIA analysing powers to any kinematic region.

Comparisons of DWIA predictions with data are less "forgiving" when the data includes polarisation data in that more stringent constraints are placed upon the theory. There is some indication that as the quality of the optical model in the input to the DWIA calculations has improved spectroscopic factors have changed signif 80). Consequently, it might be wise to re-examine earlier results in this light. Only when DWIA is able to predict analysing powers and cross sections simultaneously will one be confident in the resulting nuclear structure information.

REFERENCES

AL-79   *Proceedings of the Workshop on Program Options in Intermediate-Energy Physics*, eds. J.C. Allred and B. Talley, LA-8335-C Vol. 1 UC-34 (1979). 156.

AM-66   U. Amaldi Jr., G. Campos Venuti, G. Cortellessa, E. De Sanctis, S. Frullani, R. Lombard, and P. Salvadori, Phys. Lett. 22 (1966) 593.

AN-78   L. Antonuk, A.N. Anderson, TRIUMF Note TRI-NA-78-1 (1978) unpublished.

AR-77   R.A. Arndt, R.H. Hackman, and L.D. Roper, Phys. Rev. C15 (1977) 1002.

AU-65   N. Austern, Phys. Rev. B137 (1965) 752.

BE-76   *CRC Standard Mathematical Tables*, ed. W.H. Beyer and S.M. Selby, (CRC Press, Cleveland, 1976) 491.

BI-76   N.D. Birrell, I.E. McCarthy, and C.J. Nobel, Nucl. Phys. A271 (1976) 469.

CA-75   E.B. Cairns, and W.K. Dawson, IEEE Transactions on Nuclear Science, NS-22 (1975) 301.

CA-77   J.M. Cameron, P. Kitching, R.H. McCamis, C.A. Miller, G.A. Moss, J.G. Rogers, G. Roy, A.W. Stetz, C.A. Goulding, and W.T.H Van Oers, Nucl. Inst. and Meth. 143 (1977) 279.

CE-69   CERN Report 69-17 (1969).

CH-52   O. Chamberlain and E. Segre, Phys. Rev 87 (1952) 81.

CH-67   N.S. Chant, P.S. Fisher, and D.K. Scott, Nucl. Phys. A99 (1967) 669.

CH-79   N.S. Chant, P. Kitching, E.G. Roos, L. Antonuk, Phys. Rev. Lett. 43 (1979) 495.

CH-80   N.S. Chant, University of Maryland, private communication.

CL-52   J.B. Cladis, W.N. Hess, and B.J. Moyer, Phys. Rev. 87 (1952) 425.

CO-74   S.A. Coon and H.S. Kohler, Nucl. Phys. A231 (1974) 95.

DE-79   D.W. Devins and I.D. Svalbe, "An Analysis of Knockout Reaction Geometries", (1979) preprint.

DO-76   P. Doll, G.J. Wagner, K.T. Knopfle, and G. Mairle, Nucl. Phys. <u>A263</u> (1976) 210.

EL-67   L.R.B Elton and A. Swift, Nucl. Phys. <u>A94</u> (1967) 52.

GR-79   L.G. Greeniaus, D.A. Hutcheon, C.A. Miller, G.A. Moss, G. Roy, R. Dubois, C. Amsler, B.K.S. Koene, and B.T. Murdoch, Nucl. Phys. <u>A322</u> (1979) 308.

HO-80   H. Horiuchi, Prog. Theor. Phys. <u>63</u> (1980) 725.

HU-80   D.A. Hutcheon, in Workshop on Nuclear Structure with Intermediate-Energy Probes, eds. H. Baer, J. Moss, R. Siciliano, G. Stephenson, H. Thiessen, A. Bacher, W. Bertozzi, G. Hoffman, LA-8303-C UC-34c (1980) 220.

IO-78   A.A. Ioannides and D.F. Jackson, Nucl. Phys. <u>A308</u> (1978) 305, 317.

JA-65   D.F. Jackson and T. Berggren, Nucl. Phys. <u>62</u> (1965) 353.

JA-66   G. Jacob, Th.A.J. Maris, Rev. Mod. Phys. <u>38</u> (1966) 121.

JA-69   A.N. James, P.T. Andrews, P. Kirkby, and B.G. Lowe, Nucl. Phys. <u>A138</u> (1969) 146.

JA-73   G. Jacob and Th.A.J. Maris, C. Schneider, and M.R. Teodoro, Phys. Lett. <u>B45</u> (1973) 181.

JA-73a   G. Jacob and Th.A.J. Maris, Rev. Mod. Phys. <u>45</u> (1973) 6.

JA-75   F. James and M. Roof, Computer Phys. Comm., ed. P.G. Burke, <u>10</u> (1975) 343.

JA-76   D.F. Jackson, Nucl. Phys. <u>A257</u> (1976) 221.

JA-79   A. James, W.J. McDonald, J.M. Cameron, C.A. Miller, D.A. Hutcheon, P. Kitching, G.C. Neilson, G.M. Stinson, and E.D. Earle, Nucl. Phys. <u>A324</u> (1979) 253.

JE-77   J.P. Jeukenne, A. Lejeune, and C. Mahaux, Phys. Rev. <u>C16</u> (1977) 80.

KE-59   A.K. Kerman, H. McManus, and R.M. Thaler, Ann. of Phys. $\underline{8}$ (1959) 551.

KI-76   P. Kitching, C.A. Miller, D.A. Hutcheon, A.N. James, W.J. McDonald, J.M. Cameron, W.C. Olsen, and G. Roy, Phys. Rev. Lett. $\underline{37}$ (1976) 1600.

KI-80   P. Kitching, C.A. Miller, W.C. Olsen, D.A. Hutcheon, W.J. McDonald and A.W. Stetz, Nucl. Phys. $\underline{A340}$ (1980) 423.

KR-71   E. Kramer, G. Mairle, G. Kaschl, Nucl. Phys. $\underline{A165}$ (1971) 353.

KU-71   S. Kullander, F. Lemeilleur, P.U. Renberg, G. Landaud, J. Yonnet, B. Fagerstrom, A Johansson, and G. Tibbel, Nucl. Phys. $\underline{A173}$ (1971) 357.

KU-79   Y. Kudo and J. Mano, Lett. Al Nuovo Cimento $\underline{24}$ (1979) 289.

LI-80   R.L. Liljestrand, University of Alberta, private communication.

MA-72   P. Martin, M. Buenard, Y. Dupont, and M. Chabre, Nucl. Phys. $\underline{A185}$ (1972) 465.

MA-75   J.L. Matthews, in <u>Conference on High Energy and Nuclear Structure</u>, eds. D.E. Nagel, A.S. Goldhaber, C.K. Hargrove, R.L. Burman, and B.G. Storms (A.I.P. publication, 1975) 437.

MA-77   J.L. Matthews, W. Bertozzi, M.J. Leitch, C.A. Peridier, B.L. Roberts, C.P. Sargent, W. Turchinetz, D.J.S. Findlay, and R.O. Owens, Phys. Rev. Lett. $\underline{38}$ (1977) 8.

MA-79   Th.A.J. Maris, M.R. Teodoro, and E.A. Veit, Phys. Rev. $\underline{C20}$ (1979) 446.

MA-79a   Th.A.J. Maris, M.R. Teodoro, and C.A.Z. Vasconcellos, Nucl. Phys. $\underline{A322}$ (1979) 461.

MA-79b   Th.A.J. Maris, M.R.Teodoro, and E.A. Veit, "Effective Polarization in Quasi-Free Scattering", (1979) preprint.

MC-78   R.H. McCamis, Thesis, University of Alberta, (1978).

ME-66   A. Messiah, <u>Quantum Mechanics</u>, (North Holland Publishing Company, Amsterdam, 1966) 497.

MI-79   C.A. Miller, in Common Problems in Low and Medium -Energy Nuclear Physics, eds. B. Castel, B. Goulard, and F.C. Khanna (Plenum Press, New York, 1979) 513.

MI-80   C.A. Miller, in Proceedings of the 9th International Conference on the Few-Body Problem, (1980). To appear in Nucl. Phys. A.

MO-69   T.R. Mongan, Phys. Rev. 178 (1969) 1597.

MO-76   J. Mougey, M. Bernheim, A. Bussiere, A Gillebert, Phan Xuan Ho, M. Priou, D Royer, I. Sick, and G.J. Wagner, Nucl. Phys. A262 (1976) 461.

NA-76   K. Nakamura, S. Hiramatsu, T. Kamae, and H. Muramatsu, Nucl. Phys. A271 (1976) 221.

NA-79   A. Nadasen, T.A. Carey, P.G. Roos, N.S. Chant, C. W. Wang, and H.L. Chen, Phys. Rev. C19 (1979) 2099.

NA-80   A. Nadasen, P. Schwandt, P.P. Singh, W.W. Jacobs, A.D. Bacher, P.T. Debevec, M.D. Kaitchuck, and J.T. Meek, Phys. Rev. C (1980). In press.

PE-62   F.G. Perry and B. Buck, Nucl. Phys. 32 (1962) 353.

PE-63   F.G. Perey, Direct Interactions and Nuclear Reaction Mechanisms, eds. E. Clementel and C. Villi, (Gordon and Breach, New York, 1963) 125.

RE-70   E.F. Redish, G.J. Stephenson, Jr., and G.M. Lerner Phys. Rev. C2 (1970) 1665.

RE-73   E.F. Redish, Phys. Rev. Lett. 31 (1973) 617.

RO-74   J.G. Rogers, TRIUMF Design Note TRI-DNA-74-4 (1974) unpublished.

RO-75   J.G. Rogers, TRIUMF Design Note TRI-DNA-75-3 (1975) unpublished.

RO-75a   J.G. Rogers, TRIUMF Design Note TRI-DNA-75-13 (1975) unpublished.

RO-77   J.G. Rogers, TRIUMF Design Note TRI-DNA-75-5 (1977) unpublished.

RO-78   P.G. Roos, N.S. Chant, D.W. Devins, D.L. Friesel, W.P. Jones, A.C. Attard, R.S. Henderson, I.D. Svalbe, B.M. Spicer, V.C. Officer, and G.G. Shute, Phys. Rev. Lett. 40 (1978) 1439.

RO-80   P.G. Roos, University of Maryland, private
         communication.

SC-78   C. Schneider, Nucl. Phys. A300 (1978) 313.

SC-80   P. Schwandt, Indiana University, private
         communication.

SE-64   E. Segre, Nuclei and Particles, (W.A. Benjamin
         Inc., New York, 1964) 29.

SE-67   C. Serra, Cern Report 67-5 (1967).

SH-74   B.M. Shwiersky, C.M. Anglin, and P.D. Parker,
         Phys. Rev. C9 (1974) 910.

SM-   G. Smith, University of Colorado, private
         communication.

SP-71   D.W.L. Sprung and P.K. Banerjee, Nucl. Phys. A168
         (1971) 273.

SP-72   D.W.L. Sprung, Nucl. Phys. A182 (1972) 97.

TY-58   H. Tyrén, P. Hillman, Th.A.J. Maris, Nucl. Phys. 7
         (1958) 10.

TY-66   H. Tyrén, S Kullander, O. Sundberg, R.
         Ramachandran, and P. Isacsson, Nucl. Phys. 79
         (1966) 321.

VA-71   W.T.H. Van Oers, Phys. Rev. C3 (1971) 1550.

WI-55   J.M. Wilcox and B.J. Moyer, Phys. Rev. 99 (1955)
         875.

APPENDIX I

DWIA DESCRIPTION OF $(\vec{p},2p)$

The description of quasi-elastic (p,2p) reactions with the Distorted Wave Impulse Approximation (DWIA) has been reviewed by Jacob and Maris (JA-66,JA-73a). Their notation is shown in Figure I-2. Assumptions made in DWIA treatments of quasi-elastic scattering include the following:

1) there is a single violent interaction between the incident proton and struck nucleon and there are no other strong interactions between the incident proton and the residual nucleus,

ii) the violent interaction can be related to free proton-proton scattering,

iii) the distortion factors (defined as the ratio of plane wave functions to distorted wave functions) do not change appreciably over the range of this interaction,

(ii) and iii) are collectively a statement of the impulse approximation)

iv) the core interacts with the incoming and outgoing nucleons as a refractive and absorptive medium. This is described in terms of an optical model potential which distorts the wave functions of the incoming and outgoing protons,

v) the single particle shell model wave functions are

taken as an adequate representation of the overlap integral between the target and residual nuclei.

In the present context of generating distorted waves for protons with energies from 50 MeV to 200 MeV, the best optical model potentials available are empirically obtained from fitting elastic cross section and polarization data. A more desirable approach would be to generate optical potentials from multiple scattering theory, such as KMT (KE-59), utilizing the fundamental nucleon-nucleon interaction. However, at the current time such an approach has not yielded optical potentials for energies less than ~400 MeV which are consistent with the elastic cross section and polarization data (NA-80).

The differential cross section under the assumption of no spin-orbit dependence in the optical potential was shown by Jacob and Maris to be given by a product of a factor (K) involving the phase space and spectroscopic factors, the distorted momentum distribution of the struck nucleon (G), and the free proton-proton scattering cross section,

$$(AI.1) \quad \frac{d^3\sigma}{d\Omega_1 d\Omega_2 dE} = K \cdot G \cdot \frac{d\sigma^{fr}}{d\Omega} .$$

If there is a single value for the initial orbital angular momentum quantum number, ℓ, of the struck proton, then G is given by

$$(AI.1.1) \quad G = \sum_{m=-\ell}^{\ell} W_m \cdot |G_\ell^m|^2 .$$

The W_m are weight factors involving Clebsch Gordan coefficients. With the further assumption of zero distortion (the plane wave limit), G_ℓ^m is the Fourier transform of the initial bound state wave function of the struck proton, ϕ_ℓ^m:

$$(AI.1.2) \quad G_\ell^m = \int \exp(i\vec{k}_{A-1} \cdot \vec{r}) \cdot \phi_\ell^m(\vec{r}) d\vec{r} \quad .$$

Here $\vec{k}_{A-1}$ is the momentum of the recoil nucleus.

In spherical coordinates, the momentum dependence of G_ℓ^m enters via a spherical Bessel function, $j_\ell(k_{A-1}r)$ (ME-66). For small values of the arguement of j_ℓ,

$$(AI.1.3) \quad j_\ell \sim (k_{A-1}r)^\ell \quad .$$

Consequently, at zero recoil momentum, the momentum distribution for $\ell \neq 0$ states goes to zero while that for $\ell = 0$ states is at a maximum since j_0 is at a maximum. In practice, the minimum in the momentum distribution for $\ell \neq 0$ states at zero recoil is somewhat filled in due to the effects of distortion and the finite angular acceptance of the detectors.

The cross section for scattering free protons with parallel or antiparallel spins is given by

$$(AI.2) \quad \frac{d\sigma^{fr}}{d\Omega} = \frac{d\sigma_0}{d\Omega} \cdot \{1 + (P+P_{eff}) \cdot A + P \cdot P_{eff} \cdot C_{NN}\} \quad .$$

Here P and P_{eff} are the polarizations of the incident and struck protons respectively while A and C_{NN} are the free p-p analysing powers and correlation parameters

respectively.   P, Peff, and A are measured with respect to an axis perpendicular to the scattering plane and the polarizations are >0 for spin $\uparrow$, <0 for spin $\downarrow$.

At intermediate energies, C_{NN} is large and positive. Thus the cross section for protons with parallel spins is 3 to 5 times larger than that for protons with antiparallel spins.   Bound protons with the same ℓ ($\ell \neq 0$) but different j can be effectively polarized in opposite directions in quasi-elastic reactions.   Expression (AI.1) leads one to expect states of the same ℓ but different j to exhibit different behavior in their $(\vec{p},2p)$ analysing powers.   For $\ell = 0$ states, the effective polarization vanishes, and thus the $(\vec{p},2p)$ analysing power reduces to that for free p-p scattering.

The $(\vec{p},2p)$ analysing power, A_y, for a particular state is obtained from the spin $\uparrow$ and spin $\downarrow$ cross sections by

(AI.3) $$A_y = \frac{\dfrac{d^3\sigma}{d\Omega_1 d\Omega_2 dE}(\uparrow) - \dfrac{d^3\sigma}{d\Omega_1 d\Omega_2 dE}(\downarrow)}{\dfrac{d^3\sigma}{d\Omega_1 d\Omega_2 dE}(\uparrow) + \dfrac{d^3\sigma}{d\Omega_1 d\Omega_2 dE}(\downarrow)}$$

Substituting equations AI.1 and AI.2 into AI.3 and solving for P_{eff}, one obtains

(AI.4) $$P_{eff} = \frac{A_y - A}{C_{NN} - A_y \cdot A}$$

Thus, by measuring the analysing power, A_y, for a state and given the free p-p values A   and C_{NN}, the effective

polarization of the struck nucleon can be determined.

The inclusion of spin-orbit dependence in the optical model potential seems to be important in fitting elastic and reaction cross section as well as polarization data (NA-80). If included, spin-orbit distortion upsets the factorization of the cross section and expression (AI.1) is no longer valid. Rather, as shown by Jackson (JA-76), the cross section is factorized in the amplitudes and calculations become considerably more complicated,

$$(AI.5) \quad \frac{d^3\sigma}{d\Omega_1 d\Omega_2 dE} = C \cdot S_{1f} |T_{1f}|^2 .$$

Here C is a phase space factor and S_{1j} represents the appropriate sum and average over initial (i) and final (f) states. In DWIA, T_{fi} is given by

$$(AI.6) \quad T_{fi} = \sum_{\ell JMm\sigma_1} N^{1/2} \cdot \xi_{J_i J_f}(\ell J) \cdot (J_f M_f JM | J_i M_i) \cdot (\ell m \tfrac{1}{2}\sigma_1 | JM)$$

$$\times \sum_{\sigma_0' \mu_2' \mu_1'} \int \chi^{-*}_{\mu_2' \mu_2}(\vec{q}_2, \vec{r}) \cdot \chi^{-*}_{\mu_1' \mu_1}(\vec{q}_1, \vec{r}) \cdot \phi^n_{\ell J}(\vec{r}) \cdot \chi^+_{\sigma_0' \sigma_0}(\vec{q}_0, a\vec{r}) d\vec{r}$$

$$\times \langle \tfrac{1}{2}\mu_2', \tfrac{1}{2}\mu_1'; \tfrac{1}{2}(\vec{k}_2 - \vec{k}_1) | t_{pp} | \tfrac{1}{2}\sigma_0', \tfrac{1}{2}\sigma_1; \tfrac{1}{2}(\vec{k}_0 + \vec{k}_{A-1}) \rangle .$$

where $\vec{k}_0, \vec{k}_1, \vec{k}_2, \vec{k}_{A-1}$ are the lab momenta of the incident proton, the outgoing protons and the recoil nucleus, $\vec{q}_0, \vec{q}_1, \vec{q}_2$ are the momenta in the A+1 center of mass (JA-65) conjugate to the spatial coordinates appearing in the Schrodinger equation for the distorted wave functions; $\tfrac{1}{2}(\vec{k}_0 + \vec{k}_{A-1})$, $\tfrac{1}{2}(\vec{k}_2 - \vec{k}_1)$ are the relative momenta of the protons in their c.m. system before and after

scattering,

$(\ldots|\ldots)$ are Clebsch Gordan coefficients,

$\xi_{J_1 J_f}(\ell J)$ are fractional parentage coefficients,

σ, μ are spin quantum numbers,

$\chi_\mu, \pm$ are the distorted wave functions,

N is the spectroscopic factor corresponding to the final state ($=2J+1$ in the single particle shell model where J (or j) is the total angular momentum quantum number of the state),

and $a=(A-1)/A$.

Omitting isospin, the overlap integral (Ψ_p) of the initial and final nuclear states is given by

(AI.7) $\quad \Psi_p = \sum_{\ell J M}(J_f M_f JM|J_1 M_1) \cdot \xi_{J_1 J_f}(\ell J) \cdot \Psi_{\ell J}^M(\vec{r})$,

where

(AI.8) $\quad \Psi_{\ell J}^M(\vec{r}) = \sum_{m \sigma_1}(\ell m \frac{1}{2}\sigma_1|JM) \cdot \phi_{\ell J}^m(\vec{r}) \cdot \chi_{s_1}^{\sigma_1}$

Here s_1 and σ_1 are the spin quantum numbers for the struck proton and $\chi_{s_1}^{\sigma_1}$ is a spinor. In the context of our $^{40}Ca(p,2p)$ calculations, the overlap integral is taken to be a pure single particle state with a single value of ℓ and J. Thus, all configurational mixing is ignored and there is only a single non-zero value of $\xi_{J_1 J_f}$.

A simple statement about the result of the complication arising from the inclusion of the spin-orbit term is difficult to make, but one can make a few generalizations. The relative sizes of various p-p

amplitudes determine the polarization of the final state protons resulting from the free elastic scattering. This polarization of the particles after the interaction can affect the probability of their emergence from the nucleus resulting in a selection of specific p-p amplitudes. Hence, the spin-orbit distortion results in a modification of these relative strengths through the differing absorption and distortion of particles with opposite polarizations. In addition, the polarization of the incoming proton may be affected strongly (SC-78).

APPENDIX II

SPECTRA STORED IN MEMORY DURING EXPERIMENT

Number	Parameter	Length (Words)	Gating Requirement	Comment
1	Y-LF	128	LF·-P [1]	
2	X-LF	128	LF·-P	
3	Y-RF	128	RF·-P	
4	X-RF	128	RF·-P	
5	X-LB	128	LB·-P	
6	Y-LB	128	LB·-P	
7	X-RB	128	RB·-P	
8	Y-RB	128	RB·-P	
9	TDC	256	(LF·RB)·-P	LF Start, Stop=RB
10	TDC	256	(LB·RF)·-P	LB Start, Stop=RF
11	TDC	256	-P	Left Start, Stop=rf
12	TDC	256	-P	Right Start, Stop=rf
13	ADC	256	LF	NaI-LF
14	ADC	256	RF	NaI-RF
15	ADC	256	LB	NaI-LB
16	ADC	256	RB	NaI-RB
17	TDC	256	(LF·RF)·-P	RF Start, Stop=LF
18	TDC	256	(LB·RB)·-P	RB Start, Stop=LB
19	ADC + ADC	512	(LF·RB)	NaI-LF + NaI-RB
20	ADC + ADC	512	(LB·RF)	NaI-LB + NaI-RF
21	ADC VS ADC	4096	(LF·RB)	NaI-LF vs NaI-RB
22	ADC VS ADC	4096	(LB·RF)	NaI-RF vs NaI-LB
23	ADC VS ADC	1024	(LF·RF)	NaI-LF vs NaI-RF
24	ADC VS ADC	1024	(LB·RB)	NaI-LB vs NaI-RB
26	DCR LO	16		
26	DCR HI	16		
27	Scaler	768		Time
28	ADC	256	LF	Plastic-LF
29	ADC	256	RF	Plastic-RF

(1) -P ≡ not pulser

157

APPENDIX III

STATISTICAL TREATMENT OF ERRORS, STATISTICAL AVERAGING, DEFINITION AND INTERPRETATION OF χ^2

Counting statistics in a spectrum are given by Poisson statistics which become Gaussian when the number of counts per bin, c, becomes large ($c \gtrsim 20$). The condition, $c \gtrsim 20$, was satisfied for all data analysed in this experiment and hence all statistical quantities were assumed to follow Gaussian statistics. $\sqrt{c}$ was taken as an adequate estimate of the statistical error in the measured number of counts, c.

Consider a function of n parameters, $F(p_1, p_2, \ldots, p_n)$. Some of the parameters will have corresponding uncertainties and may be correlated with other parameters. Still others will be pre-determined and have no uncertainty and no correlation with other parameters. The uncertainty in F is given by

$$(AIII.1) \quad \Delta F = \left[\sum_{i=1}^{n} \left(\frac{\partial F}{\partial p_i} \cdot \Delta p_i \right)^2 + 2 \cdot \sum_{i=1}^{n} \sum_{j=i+1}^{n} \frac{\partial F}{\partial p_i} \cdot \frac{\partial F}{\partial p_j} \cdot \Delta(p_i p_j) \right.$$

$$\left. + \text{ higher order terms} \right]^{1/2},$$

where the summations extend over the parameters which are not pre-determined,

Δp_i is the error in the ith parameter,

$\Delta(p_i p_j)$ is the covariance between the ith and jth parameters.

In general, a mathematical model which is to be fit

to a set of measurements, $y_i \pm \Delta y_i$ $(i=1,m)$, must make a prediction, F_i, corresponding to each measurement, y_i. The predictions come from the evaluation of a function, $F(p_1, p_2, \ldots, p_n)$. Some of the parameters will be determined and thus fixed while others are free to be varied by a fitting program. The purpose of the fitting program is to find a set of values for the free parameters which minimize the value of a function called χ^2. In the simplest case, χ^2 may be computed from

$$(AIII.2) \quad \chi^2 = \sum_{i=1}^{m} \left(\frac{F_i(p_1, p_2, \ldots, p_n) - y_i}{\Delta y_i} \right)^2 .$$

This expression for χ^2, when applied to a spectrum where m is the number of bins, is approximately true if the number of counts is not too small (>5). Strictly speaking, the y_i should be independent, normally distributed random variables and Δy_i must be their standard deviations.

As a special case, if a series of measurements, $y_i \pm \Delta y_i$ $(i=1,m)$, are made of a single quantity, y, the statistically weighted average for y and the corresponding error are given by

$$(AIII.3) \quad \bar{y} = \frac{\sum_{i=1}^{m} y_i \cdot (\Delta y_i)^{-2}}{\sum_{i=1}^{m} (\Delta y_i)^{-2}} ,$$

$$\Delta \bar{y} = \left(\sum_{i=1}^{m} (\Delta y_i)^{-2} \right)^{-1/2} .$$

In addition to returning a set of values for the parameters which minimize χ^2, the fitting routine also returns a symmetric matrix variously referred to as the covariance, variance, or error matrix. The ith diagonal element of this matrix is the variance (or the square of the standard deviation) of the ith free parameter. Changing one of the parameters by an amount equal to its standard deviation and refitting with this parameter fixed would result in χ^2 increasing by 1. These standard deviations are taken as the errors in the parameters, Δp_i. The (i,j)th element of the matrix is the covariance between the ith and jth parameters, $\Delta(p_i p_j)$.

In the course of developing a fitting model, a parameter may be used which has previously been determined independently to a certain accuracy, $\overline{p}_c \pm \Delta \overline{p}_c$. In this case, it may be desirable to let the parameter remain free while constraining it with this additional information. This constraint is implemented by including a term in the χ^2 function,

(AIII.4) $\quad \left(\dfrac{p_c - \overline{p}_c}{\Delta \overline{p}_c}\right)^2$

Another situation that arises is the desire to restrict the value of a parameter to a particular region. This is done by means of adding a penalty term into the χ^2. An example of a χ^2 function with both a constraint term and a penalty term is

$$(AIII.5) \quad \chi^2 = \sum_{i=1}^{m} \left(\frac{F(x_i, P_1, P_2, \ldots, P_n) - y(i)}{\Delta y(i)} \right)^2$$

$$+ \left(\frac{P_c - \bar{P}_c}{\Delta \bar{P}_c} \right)^2 + \left\{ \begin{array}{ll} 0 & \text{if } P_d > 0 \\ 100 \cdot P_d^2 & \text{if } P_d < 0 \end{array} \right\}.$$

Here the third term (the penalty term) helps to constrain the dth parameter to non-negative values. Penalty terms may help to prevent the fit from producing unphysical values for parameters such as negative amplitudes for peaks.

The value of χ^2 may be used to determine the degree to which the data was successfully fit by the model. One measure for this is the value of χ^2 per degree of freedom. The number of degrees of freedom involves the number of data points minus the number of unconstrained free parameters. A second (but independent) measure based on the χ^2 and number of degrees of freedom is called the percentage point. Tables of percentage points are available in standard mathematical handbooks (BM-76). Its value ranges from 0 to 1 and it represents the fractional probability of obtaining a value for χ^2 equal to or less than the value of χ^2 observed. For a single fit, a definite conclusion based on either of these two quantities is difficult to outline but very general statements can be made. Fits with a χ^2 per degree of freedom (percentage point) of ～ (≥0.2) indicate a reasonably good fit.

very large values, $\gtrsim 4$ ($\gtrsim 0.95$), indicate a poor fit and put the validity of the model into question; very small values, $\lesssim 0.4$ ($\lesssim 0.1$), indicate a fit that is "too" good and may suggest that the errors in the data have been overestimated.

For a number of sets of data fit by a single model, if the model describes the data and the data and variances follow a normal distribution the histogram of percentage points should be flat.

The model used in the fitting involved Gaussian peaks of the form given in equation V.1. The result of fitting a set of data were two amplitudes for each peak in the model (one for each spin direction). In addition, for some fits, the width, C52, was a variable parameter. Let

$A{\uparrow}\pm\Delta A{\uparrow}$ be the amplitude for the spin $\uparrow$ peak,

$A{\downarrow}\pm\Delta A{\downarrow}$ be the amplitude for the spin $\downarrow$ peak,

$C52\pm\Delta C52$ be the width parameter,

$P{\uparrow},P{\downarrow}$ be the beam polarizations of the spin $\uparrow,\downarrow$ data

(where both values are between 0 and 1).

In terms of these parameters, the partially polarized spin $\uparrow$ and $\downarrow$ cross sections and their errors are given by

(AIII.6) $\quad \sigma_p^{\uparrow} = \dfrac{A{\uparrow}\cdot\sqrt{\pi}}{C52}$, $\quad \sigma_p^{\downarrow} = \dfrac{A{\downarrow}\cdot\sqrt{\pi}}{C52}$,

$$\Delta\sigma_p^{\uparrow} = \sqrt{\pi}\cdot\left[\left(\frac{\Delta A{\uparrow}}{C52}\right)^2 + \left(\frac{A{\uparrow}\cdot\Delta C52}{C52^2}\right)^2 + 2\cdot\left(\frac{A{\uparrow}}{C52^3}\right)\cdot\Delta(A{\uparrow},C52)\right]^{1/2},$$

$$\Delta\sigma_p^{\downarrow} = \sqrt{\pi}\cdot\left[\left(\frac{\Delta A{\downarrow}}{C52}\right)^2 + \left(\frac{A{\downarrow}\cdot\Delta C52}{C52^2}\right)^2 + 2\cdot\left(\frac{A}{C52}\right)\cdot(A{\downarrow},C52)\right]^{1/2}.$$

where equations V.3 and AIII.1 have been used.

Let $\sigma\uparrow$ and $\sigma\downarrow$ represent the cross sections for 100% polarizations. The relations between the partially polarized and 100% cross sections are:

$$\text{(AIII.7)} \quad \sigma_p^\uparrow = \frac{1}{2} \cdot (1+P\uparrow) \cdot \sigma\uparrow + \frac{1}{2} \cdot (1-P\uparrow) \cdot \sigma\downarrow \quad,$$

$$\sigma_p^\downarrow = \frac{1}{2} \cdot (1-P\downarrow) \cdot \sigma\uparrow + \frac{1}{2} \cdot (1+P\downarrow) \cdot \sigma\downarrow \quad.$$

Solving for $\sigma\uparrow$, $\sigma\downarrow$ we have

$$\text{(AIII.8)} \quad \sigma\uparrow = \frac{(1+P\downarrow) \cdot \sigma_p^\uparrow - (1-P\uparrow) \cdot \sigma_p^\downarrow}{P\uparrow + P\downarrow}$$

$$\sigma\downarrow = \frac{(1+P\uparrow) \cdot \sigma_p^\downarrow - (1-P\downarrow) \cdot \sigma_p^\uparrow}{P\uparrow + P\downarrow}$$

The unpolarized cross section and analysing powers are defined as

$$\text{(AIII.9)} \quad \sigma_0 = \frac{\sigma\uparrow + \sigma\downarrow}{2}$$

$$A_y = \frac{\sigma\uparrow - \sigma\downarrow}{\sigma\uparrow + \sigma\downarrow} \quad.$$

and in terms of the partially polarized results, these quantities become

$$\text{(AIII.10)} \quad \sigma_0 = \frac{P\downarrow \cdot \sigma_p^\uparrow + P\uparrow \cdot \sigma_p^\downarrow}{P\uparrow + P\downarrow}$$

$$A_y = \frac{\sigma\uparrow - \sigma\downarrow}{\sigma\uparrow + \sigma\downarrow}$$

Finally, from equations AIII.1, AIII.10 and recalling that $\sigma_p^{\uparrow}$ and $\sigma_p^{\downarrow}$ are independent quantities, the errors in σ_0 and A_y are given by

$$(AIII.11) \quad \Delta\sigma_0 = \frac{1}{P\uparrow+P\downarrow} \cdot \left[(P\downarrow \cdot \Delta\sigma_p^{\uparrow})^2 + (P\uparrow \cdot \Delta\sigma_p^{\downarrow})^2 \right]^{1/2}$$

$$\Delta A_y = \frac{P\uparrow+P\downarrow}{(P\downarrow \cdot \sigma_p^{\uparrow}+P\uparrow \cdot \sigma_p^{\downarrow})^2} \cdot \left[(\sigma_p^{\downarrow} \cdot \Delta\sigma_p^{\uparrow})^2 + (\sigma_p^{\uparrow} \cdot \Delta\sigma_p^{\downarrow})^2 \right]^{1/2}$$

The statistical errors   are sufficiently small to be ignored. The   due to the polarimeter p-p calibration does not affect the fits.

APPENDIX IV

FITTING FUNCTIONS

```
C----------------------------------------------------------------
C--    THIS CALCULATES THE CONTRIBUTION OF 40CA(P,2P) TO THE
C--    ENERGY SUM SPECTRUM AT THE POINT XT.
C--    A52,A32,AS12,AB ARE THE AMPLITUDES OF THE 40CA
C--    1D52,1D32,2S12, AND BACKGROUND PEAKS.
C--    SH IS A PARAMETER USED TO SEPARATE SPIN UP AND DOWN
C--    DATA.
C----------------------------------------------------------------
       FUNCTION FIT(A52,A32,AS12,AB,C52,BB,XI,XT,SH)
       IMPLICIT REAL*8 (A-H,O-Z)
       DATA DSUM/4.96/
       CSQ=-C52*C52
       CONST=XT-SH-XI
       FIT=A52*0.91/DSUM*DEXP(CSQ*(CONST+5.27)**2)
      *    +A52*0.64/DSUM*DEXP(CSQ*(CONST+5.61)**2)
      *    +A52*1.25/DSUM*DEXP(CSQ*(CONST+6.34)**2)
      *    +A52*0.10/DSUM*DEXP(CSQ*(CONST+6.50)**2)
      *    +A52*0.10/DSUM*DEXP(CSQ*(CONST+6.77)**2)
      *    +A52*0.18/DSUM*DEXP(CSQ*(CONST+6.96)**2)
      *    +A52*0.10/DSUM*DEXP(CSQ*(CONST+7.20)**2)
      *    +A52*0.47/DSUM*DEXP(CSQ*(CONST+7.43)**2)
      *    +A52*0.10/DSUM*DEXP(CSQ*(CONST+7.78)**2)
      *    +A52*0.35/DSUM*DEXP(CSQ*(CONST+8.17)**2)
      *    +A52*0.24/DSUM*DEXP(CSQ*(CONST+8.43)**2)
      *    +A52*0.22/DSUM*DEXP(CSQ*(CONST+8.55)**2)
      *    +A52*0.10/DSUM*DEXP(CSQ*(CONST+8.90)**2)
      *    +A52*0.10/DSUM*DEXP(CSQ*(CONST+9.10)**2)
      *    +A52*0.10/DSUM*DEXP(CSQ*(CONST+9.75)**2)
      *    +A32*DEXP(CSQ*(CONST)**2)
      *    +AS12*DEXP(CSQ*(CONST+2.52)**2)
      *    +AB*DEXP(CSQ*(CONST+12.4)**2)
       RETURN
       END
C----------------------------------------------------------------
C--    THIS CALCULATES THE CONTRIBUTION OF 16O(P,2P) TO THE
C--    ENERGY SUM SPECTRUM AT THE POINT XT.
C--    AP12, AP32 ARE THE AMPLITUDES OF THE 16O 1P12 AND 1P32
C--    PEAKS.
C----------------------------------------------------------------
       FUNCTION CTM(AP12,AP32,C52,XI,XT,SH)
       IMPLICIT REAL*8 (A-H,O-Z)
       CSQ=-C52*C52
       CONST=XT-SH-XI
       CTM=AP12*DEXP(CSQ*(CONST+3.797)**2)
      *    +AP32*DEXP(CSQ*(CONST+10.11)**2)
       RETURN
       END
```

APPENDIX V

OPTICAL MODEL POTENTIAL FOR p-^{40}Ca SYSTEM

The optical potential used in the calculations consisted of a Coulomb term, a complex valued nuclear central term, and a complex valued nuclear spin-orbit term

$$(AV.1) \quad U(r) = U_{coul}(r) - Vf_0(r,R_0,a_0) -$$
$$i\left[W_s - 4a_w W_d \frac{d}{dr}\right]f_w(r,R_w,a_w) +$$
$$2\left[V_{so} + iW_{so}\right]\frac{1}{r}\frac{d}{dr}f_{so}(r,r_{so},a_{so})\, \vec{L}\cdot\vec{\sigma}$$

where the form factors, f, have Woods-Saxon shapes,

$$(AV.2) \quad f = f(r,R,a) = \frac{1}{1+e^{(r-R)/a}}$$

The values of the various parameters as a function of energy are listed in Table X. The details of the analysis method used to derive this potential are given in (NA-80). The analysis used to obtain the optical potential was based on a semi-relativistic Schrodinger-type wave equation derived from the Dirac equation for a fermion moving in a localized central potential, U(r). As the spin-orbit term arising from the Dirac equation is negligible, the one used in this analysis is purely phenomenological. With the projectile treated relativistically and the target non-relativistically, the radial wave equation for the relative

TABLE X

Optical Model Values* for p-^{40}Ca System

R_{coul}=1.20 fm (Coulomb radius)

R_{so} = 1.035 fm

a_{so} = 0.605 fm

T (MeV)	40	60	80	100	120	140	160	180	200
V (MeV)	42.5	33.2	28.9	25.5	22.7	20.4	18.6	17.0	15.6
R_0 (fm)	1.194	1.207	1.220	1.231	1.242	1.252	1.260	1.266	1.27
a_0 (fm)	0.738	0.746	0.752	0.758	0.762	0.764	0.766	0.768	0.77
W_s (MeV)	0	5.4	6.4	6.4	6.3	6.6	7.3	7.9	8.4
W_d (MeV)	4.4	2.0	0	0	0	0	0	0	0.
R_w (fm)	1.356	1.394	1.440	1.440	1.440	1.424	1.370	1.312	1.26
a_w (fm)	0.470	0.496	0.520	0.556	0.588	0.620	0.650	0.650	0.62
V_{so} (MeV)	6.30	5.28	4.55	3.99	3.52	3.14	2.80	2.51	2.25
W_{so} (MeV)	0.44	-0.35	-0.72	-1.02	-1.27	-1.47	-1.65	-1.80	-1.95

* From (SC-80).

(AV.3) $\left[\dfrac{d}{d\rho^2} + 1 - \dfrac{\gamma U}{T^{cm}} - \dfrac{\ell(\ell+1)}{\rho^2}\right]F(\rho) = 0$,

where $\rho = \dfrac{k'r'}{\hbar}$ $\qquad (\vec{r}\,' \equiv \vec{r}_p - \vec{r}_{{}^{40}Ca}, \quad \vec{k}\,' \equiv \vec{k}_p - \vec{k}_{{}^{40}Ca})$,

$\gamma = 1 + \dfrac{T^{cm}}{T^{cm} + 2mc^2}$ (m = mass of proton) ,

T^{cm} is the total kinetic energy in the center of

mass of the p-^{40}Ca system.

The corresponding non-relativistic Schrodinger

equation used in the DWIA program is

(AV.4) $\left[\dfrac{d}{d\rho^2} + 1 - \dfrac{2\mu V}{(k')^2} - \dfrac{\ell(\ell+1)}{\rho^2}\right]F(\rho) = 0$.

Thus, in order to use the potentials in a manner consistent

with the way they were derived, the following substitutions

were made for the potential, V, and the reduced mass, μ,

(AV.5) $\mu \rightarrow \dfrac{(k')^2}{2 \cdot T^{cm}}$, $V \rightarrow \gamma U$.

VITA

NAME: Larry Edward Antonuk

PLACE OF BIRTH: Calgary, Alberta, Canada

YEAR OF BIRTH: 1953

POST-SECONDARY EDUCATION AND DEGREES:

University of Calgary
Calgary, Alberta
1971-1975 B.Sc.

HONOURS AND AWARDS:

Calgary Separate School Board Grade 10 Deferred Scholarship
University of Calgary
1971

Grade 12 Departmental Examination Catholic School Board
Award
University of Calgary
1971

City of Calgary Matriculation Scholarship
University of Calgary
1971

Ladies Auxiliary Alberta Command Royal Canadian Legion
Award
University of Calgary
1971

Home Oil Company Limited Centennial Scholarship
University of Calgary
1972-1974

Province of Alberta Scholarship
University of Calgary
1972-1974

National Research Council Postgraduate Scholarship
University of Alberta
1975-1976

University of Alberta Graduate Teaching/Research
Assistantship
University of Alberta
1975-1980

Province of Alberta Graduate Fellowship
University of Alberta
1979-1980